TECHNISCHE UNIVERSITÄT WIEN

AUTOMATION & CONTROL INSTITUTE
INSTITUT FÜR AUTOMATISIERUNGS- & REGELUNGSTECHNIK

DIPLOMARBEIT

Opto-mechatronical analysis and outlook on potential improvements for Austria's largest telescope system

Ausgeführt zum Zwecke der Erlangung des akademischen Grades eines
Diplom-Ingenieurs (Dipl.-Ing.)

unter der Leitung von

Univ.Prof. Dipl.-Ing. Dr.sc.techn. Georg Schitter
Univ.Prof. Dipl.-Ing. Dr.techn. Gerhard Schütz
Projektass. Dipl.-Ing. Andreas Sinn
ao. Univ.-Prof. Dr. Werner Zeilinger

eingereicht an der
Technischen Universität Wien
Fakultät für Physik

von
Florian Kreuzmair BSc.
Matrikelnummer: 11706733

Acknowledgements

I would like to thank everyone who has contributed in any way to the completion of this thesis.

First of all I would like to thank Univ.Prof. Dr.sc.techn. Georg Schitter and Univ.Prof Dipl.-Ing. Dr.techn. Gerhard Schütz for supervising me and giving me a place to do my research. A big thank you also goes to Univ.-Prof Werner Zeilinger, who was a great help with everything concerning the Leopold Figl-Observatory. I would also like to give a very special thank you to my supervisor, Dipl. Ing. Andreas Sinn, for his patience, knowledge and advice throughout the whole thesis.

Finally, I would like to thank all my friends and family, without their support I would not have come this far. My biggest thanks, however, go to my girlfriend Rosa for her constant encouragement and tireless support throughout my academic journey. Thank you.

Kurzfassung

Astronomische Teleskope ermöglichen hochwertige Bilder von weit entfernten Objekten und unterstützen Anwendungen in der Astronomie, der Satellitenbeobachtung und der optischen Kommunikation. Die Bildqualität wird jedoch häufig durch Wellenfrontverzerrungen beeinträchtigt, die durch Ausrichtungsfehler und strukturelle Verformungen verursacht werden. Besonders thermische Ausdehnung und Gravitation verursachen relative Verschiebungen zwischen Primär- und Sekundärspiegeln, weshalb aktive Kompensationsstrategien erforderlich sind.

Diese Arbeit untersucht die opto-mechanischen Eigenschaften des Leopold Figl-Observatoriums (LFO), um potentielle Einschränkungen und Verbesserungen zu identifizieren. Anhand eines kleinen RC-Teleskops wird ein Messsystem entwickelt und getestet, welches anschließend zur Vermessung der Relativpositionen der Spiegel des LFOs verwendet wird.

Das kleine RC-Teleskop hat einen Hauptspiegeldurchmesser von 254 mm und ist mit einem Präzisionspositionierungssystem für den Sekundärspiegel ausgestattet, das kein Licht vom Teleskop benötigt, um Wellenfrontfehler zu verringern. Zur Simulation des Betriebs bei Tag wurde ein asymmetrischer Temperaturgradient von über 20 °C angelegt. Während der Erwärmung verbesserte sich der RMS-Wellenfrontfehler von 185 nm auf 46 nm, was einer Verbesserung um den Faktor 4.0 entspricht. Bei ausschließlicher Betrachtung der kompensierten Freiheitsgrade - Defokus, sowie die Verkippung des Sekundärspiegels - reduzierte sich der RMS-Wellenfrontfehler von 167 nm auf 13 nm, eine Verbesserung um den Faktor 12.8. Bei allen Messungen, bei denen das Kompensationssystem verwendet wurde, konnte ein Strehl-Verhältnis (SR) von mehr als 80% beibehalten werden, was die Wirksamkeit des Systems bei der Kompensation von Umgebungsstörungen belegt.

Anschließend wurde das Messsystem erfolgreich am LFO mit einem Hauptspiegeldurchmesser von 1.52 m installiert. Die Messungen zeigen für einzelne, stationäre Posen ein langsames, geringes Driftverhalten mit durchschnittlich 4.54 µm axialer Verschiebung und nahezu keiner Verkippung. Zwischen verschiedenen Teleskoppositionen variiert die Relativposition zwischen Primär- und Sekundärspiegel jedoch erheblich, mit einer durchschnittlichen Abweichung von 45.08 µm und einer maximalen von 78.04 µm, was das SR signifikant beeinträchtigt. Auf Basis dieser Ergebnisse scheint ein aktives Kompensationssystem, besonders für den Fokus des Teleskops, sinnvoll. Zur Validierung dieser Ergebnisse sind weitere Messungen am LFO erforderlich.

Abstract

Astronomical telescopes enable high-quality imaging of distant objects, supporting applications in astronomy, satellite observation and optical communication. However, image quality is often degraded by wavefront distortions caused by alignment errors and structural deformations. In particular, thermal expansion and gravitational effects lead to relative displacements between the primary and secondary mirrors, necessitating active compensation strategies.

This thesis investigates the opto-mechanical properties of the Leopold Figl-Observatory (LFO) to identify potential limitations and improvements. Using a small RC-telescope, a measurement system is developed and tested, which is then used to measure the relative positions of the mirrors of the LFO.

The small RC-telescope has a 254 mm primary mirror and is equipped with a precision secondary mirror positioning system that operates independently of telescope light to reduce wavefront errors. An asymmetric temperature gradient of over 20 °C was applied to simulate daytime operation. During heating, the RMS wavefront error improved from 185 nm to 46 nm, an improvement by a factor of 4.0. When considering only the compensated degrees of freedom - defocus and the tilting of the secondary mirror - the RMS wavefront error reduced from 167 nm to 13 nm, a factor of 12.8. In all measurements utilizing the compensation system a Strehl ratio (SR) exceeding 80% could be maintained, demonstrating its effectiveness in compensating for environmental disturbances.

The measurement system was then successfully installed on the LFO (1.52 m primary mirror). The measurements show a slow, small drift behaviour for individual stationary positions with an average axial shift of 4.54 µm and almost no tilt. However, between different telescope positions, the relative position between the primary and secondary mirror varies considerably, with an average deviation of 45.08 µm and a maximum of 78.04 µm, which significantly affects the SR. Based on these results, an active compensation system, especially for the focus of the telescope, seems sensible. Further measurements on the LFO are needed to validate these results.

Contents

1 Introduction **1**
- 1.1 Motivation . . . 2
- 1.2 Tasks and goals . . . 4
- 1.3 Outline . . . 4

2 State of the Art **5**
- 2.1 Telescope designs . . . 5
  - 2.1.1 Refracting telescopes . . . 5
  - 2.1.2 Reflecting telescopes . . . 6
- 2.2 Metrology for telescope systems . . . 7
  - 2.2.1 Dimensional metrology system . . . 7
  - 2.2.2 Wavefront sensing . . . 8
  - 2.2.3 Measurement of environmental factors . . . 8
- 2.3 Compensation approaches . . . 8
  - 2.3.1 Primary mirror system . . . 9
  - 2.3.2 Secondary mirror system . . . 10
  - 2.3.3 Adjusted secondary mirror system . . . 11
  - 2.3.4 Actuation of the secondary mirror mounting . . . 12
  - 2.3.5 Adaptive optics systems . . . 13
  - 2.3.6 Compensation systems for thermal expansion . . . 15
  - 2.3.7 Summary . . . 16
- 2.4 Leopold Figl-Observatory . . . 16
- 2.5 Research questions . . . 19

3 Theoretical background **20**
- 3.1 Imaging-quality . . . 20
- 3.2 Zernike polynomials . . . 21
- 3.3 Strehl ratio . . . 23
- 3.4 General aberration theory . . . 25
- 3.5 Wavefront sensor . . . 28

4 Implementation of the metrology system **31**
- 4.1 Telescope system . . . 31
- 4.2 Collimation . . . 32
- 4.3 Measurement system . . . 35
- 4.4 Experiment setup . . . 37
- 4.5 Results of the small RC-telescope . . . 38
  - 4.5.1 Comparison of undisturbed system with and without compensation 38
  - 4.5.2 Comparison of disturbed system (heating) with and without compensation) . . . 40
  - 4.5.3 Comparison of disturbed system (cooldown) with and without compensation) . . . 43
  - 4.5.4 Comparison heating and cooldown phases . . . 47
- 4.6 Discussion . . . 49

5 Leopold Figl-Observatory **50**
5.1 Sensitivity analysis . . . 50
5.2 Design of the metrology mounting adapters . . . 51
5.3 Measurement procedure . . . 54
5.4 Results of the LFO . . . 56
5.4.1 Individual measurements . . . 57
5.4.2 Comparison of absolute distances . . . 61
5.5 ACINOGS . . . 65
5.6 WFS proof of concept at ACINOGS . . . 67
5.7 Discussion . . . 69

6 Conclusion and outlook **71**
6.1 Conclusion . . . 71
6.2 Outlook . . . 72

List of Figures

1.1 Schematic depiction of a Ritchey-Chrétien telescope design. 2

2.1 Simplified depiction of a lens based telescope design. 5
2.2 Simplified depiction of some reflective telescope designs. 6
2.3 Schematic presentation of an axial and lateral actuation system. 10
2.4 Schematic representation of a hexapod. 11
2.5 Schematic presentation of an advancement to a standard hexapod. 12
2.6 Secondary mirror structure of the DCT. 13
2.7 Graphic visualisation of an adaptive optics system. 14
2.8 Comparison of an image of Uranus without (left) and with AO (right). . . 14
2.9 LFO as seen from outside. 17
2.10 Different lightpaths of LFO. 17
2.11 LFO from inside the dome. 18

3.1 Geometrical ray trace of a general optical system. 20
3.2 Visual representation of the wave aberration function. 21
3.3 Visualisation of the first 21 Zernike polynomials. 23
3.4 Plot visualising the Strehl ratio. 24
3.5 Light path in case of coma. 25
3.6 Picture visualising the effect of coma. 25
3.7 Light path in case of astigmatism. 26
3.8 Picture visualising the effect of astigmatism. 26
3.9 Light path of spherical aberration of the Hubble Space Telescope. 27
3.10 Picture visualising the effect of spherical aberration. 27
3.11 HST images before and after repair. 28
3.12 Schematic presentation of the principle of operation of a SH-WFS. 28
3.13 Developed WFS module compatible with a focused beam. 29

4.1 Schematics of the small RC-telescope setup. 31
4.2 Design of the active secondary mirror system. 32
4.3 3D model of the secondary mirror system. 32
4.4 Description of a visual collimation method for a RC-telescope. 33
4.5 Alternative collimation screws of the secondary mirror. 34
4.6 Star test, where the SM is misaligned (left) and after adjustment (right). . 34
4.7 Experimental setup of the small RC-telescope. 35
4.8 SHWFS and adapter tube with collimating lens. 36
4.9 Ray tracing of the complete optical setup. 37
4.10 Overview from the laboratory to the artificial star. 38
4.11 Dimensional measurement of the undisturbed system. 39
4.12 Zernike polynomial measurement and RMS WFE of the undisturbed system. 39
4.13 Dimensional measurement of the system while heating. 40
4.14 Zernike polynomial measurement during the heating phase. 41
4.15 Measured RMS WFE of the heating phase. 42
4.16 Major Zernike polynomials and resulting RMS WFE while heating. 42
4.17 Zernike polynomials not targeted by compensation system while heating. . 43
4.18 Dimensional measurement during the cooldown phase. 44
4.19 Zernike polynomial measurement during the cooldown phase. 44

4.20 Measured RMS WFE during a cooldown phase. 45
4.21 Major Zernike polynomials and resulting RMS WFE while cooling down. . 46
4.22 Zernike polynomials not targeted by compensation system during cooldown. 46
4.23 Metrology data of an uncompensated combined heating and cooldown phase. 47
4.24 WFS data of an uncompensated combined heating and cooldown phase. . . 48
4.25 Metrology data of a compensated combined heating and cooldown phase. . 48
4.26 WFS data of a compensated combined heating and cooldown phase. 49

5.1 Sensitivity analysis of the LFO conducted in simulation with Zemax. . . . 51
5.2 3D-model of the PM ring adapter. 52
5.3 Manufactured PM ring adapter. 53
5.4 Closeup of the PM and IF adapters. 53
5.5 Opening of the PM of LFO where the PM adapter is mounted. 53
5.6 Manufactured RR adapter. 53
5.7 Maximum achievable angle without entering light path. 54
5.8 Mounted dimensional metrology system on PM side. 54
5.9 Alignment of the three IF axis with the three RR. 54
5.10 Connection between the WFS and the backplate of the telescope. 55
5.11 Adapter unit of the LFO for the WFS. 56
5.12 Overview of interferometer head and retroreflector positions. 56
5.13 Collection of the dimensional measurements in the Zenith position. . . . 57
5.14 Collection of the dimensional measurements pointing southwards. 59
5.15 Collection of the dimensional measurements pointing in an eastern direction. 60
5.16 Collection of the dimensional measurements pointing in a western direction. 61
5.17 Collection of the dimensional measurements in the Pole position. 61
5.18 Absolute axial distances relative to the first measurement with errorbars. . 63
5.19 Absolute axial distances of the first eight measurements with errorbars. . . 64
5.20 Absolute axial distances of the last twelve measurements with errorbars. . 64
5.21 ACINOGS of TU Wien located in Science Center Arsenal. 66
5.22 Adapter for simultaneous mounting of camera and WFS. 67
5.23 Groundstation WFS measurement over 15 min. 68
5.24 Groundstation WFS measurement over 5 min. 68

List of Tables

1.1 Sources of error that lead to a reduction in image quality of telescopes. . . 3

2.1 Technical data of different lightpaths. 17

3.1 List of Zernike polynomials up to the 4th order. 22

4.1 Properties of IDS3010 interferometer. 35

5.1 Metadata for Measurements. 62
5.2 Summary of individual measurements. 63
5.3 LFO summary of absolute axial distance changes. 65

1 Introduction

Optical telescope systems play a crucial role in many applications. They are not only essential for fields like astronomy and astrophysics, but are also important in more recent fields such as satellite tracking, the observation of space debris, facilitating communication, weather monitoring and Earth observation. By collecting light in a high quality manner they help deepen our understanding of the universe and in understanding complex processes and relationships [1]. Some of these are for instance, the study of the cosmic microwave background (CMB) radiation, the search for exoplanets and solar observations across different wavelengths [2]. Through the study of the CMB radiation information about the age, structure and composition can be gained as well as furthering our understanding of Dark Matter [3]. Solar telescopes monitor solar flares and sunspots among other things, which contributes to space weather forecasting [4].

To deliver high quality images, the telescope needs to track the desired target at all times, even if it is moving. This is summarized by pointing, acquisition and tracking [5]. This is especially important for both astrophysics and novel fields such as space debris and satellite tracking [6]. Furthermore, the imaging quality of the telescope directly affects the quality of the resulting scientific data.

In recent years, the amount of debris orbiting the Earth has increased drastically. In particular, events such as collisions and satellites being intentionally shot down have led to a sharp increase in the number of debris in orbit. As this is a very new problem, there is still no clear space law or international agreement that clearly specifies how space debris should be handled. At the moment, there is only a guideline that states can follow on a voluntary basis [7]. As a result, no reduction in space debris has yet been achieved. This has made space missions significantly more difficult, because operators now must ensure that their spacecraft avoids any collisions with debris. For this to be possible validated, accurate and up-to-date data that is made available on maps is required. Since this data is changing over time and trajectories can change significantly within a few days, telescopes are needed to track and determine the exact orbits of satellites and debris [8, 9].

Another area of application is free-space optical communication (FSO). FSO uses light to transmit data and has the advantage of achieving high data rates and uses highly directional light beams which do not spread out unlike radio waves. This narrow beam width increases security by making it more unlikely for signals to be intercepted. FSO systems have a beam divergence that is approximately 1000 times narrower than radio frequency systems (RF), leading to significantly reduced signal spread. Additionally, due to the much higher carrier frequency, FSO systems can support data rates up to multi-Gbps, whereas RF system typically only achieve roughly 100 Mbps for small satellites [10]. Despite these advantages, FSO communication is highly susceptible to atmospheric disturbances, such as turbulence, and scattering, which can degrade signal quality and reliability. Telescopes play a critical role by firstly providing the ability to create a tightly collimated light beam which ensures long distance communication. Secondly they implement the tracking and pointing mechanism by constantly realigning the transmitter and receiver.

To mitigate atmospheric disturbances, adaptive optics (AO) is employed. AO systems dynamically adjust the wavefront of the optical signal to compensate for distortions caused by turbulence, improving the overall signal quality [10].

In summary optical telescope systems enable a variety of applications in classical and novel research fields and applications. However, their core properties may be affected by environmental influences degrading the imaging quality and pointing precision.

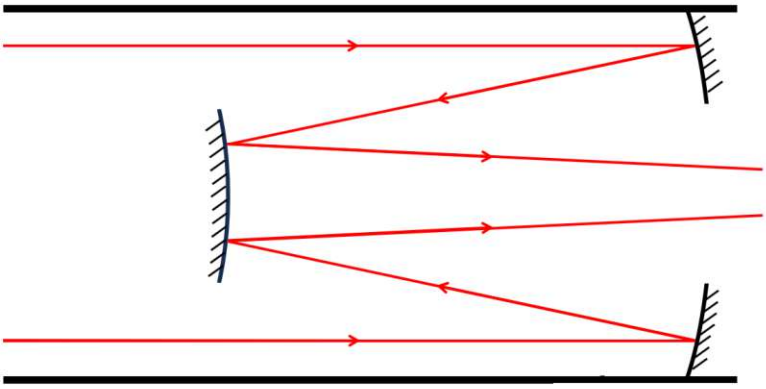

Figure 1.1: Schematic depiction of a Ritchey-Chrétien telescope design.

1.1 Motivation

For many application areas typically reflecting telescopes are used, most commonly the Ritchey-Chrétien (RC) design, due to its ability to maintain image quality across a wide field of view. However, external disturbances can lead to misalignment of mirrors, necessitating compensation techniques such as active optics, which is the focus of this study [1]. There are many more sources which can introduce an error in the telescope performance. In Table 1.1 is a list of sources with their corresponding frequencies. The errors are given as a *band-pass*, which is a range over which the temporal signal properties typically change. The first two errors are related to the design and manufacturing process, which only occurs in the making of the telescope and remain the same and are therefore called d.c. effects, referring to a direct current (d.c.) which does not change over time. The sources of error in telescopes can be categorised into theoretical, maintenance, thermal, mechanical and atmospheric errors. The theoretical errors occur due to lateral tube bending or longitudinal sag. Maintenance errors are often the most serious error sources and usually exceed the theoretical ones. They include among other things malfunctions of supporting structures and misaligments of optical elements or maladjustments such as defocus. Thermal distortions occur slowly due to the masses and thermal capacities of telescopes [11]. Even though in modern telescopes there is an effort to reduce mass of the mirrors and the supporting structures it will still be considerable in larger telescope systems. Mechanical distortions of mirrors have been of little significance because glass has a very high stability, but they are gaining importance with the reduction of mirror thickness and the increased use of alternative materials like metals [12]. The frequency region of the bandpass is again low, because the structural changes take place over a relatively long period of time. Mirror deformation due to wind gusts is a significant issue for modern, very large telescopes with flexible mirrors, particularly those designed to operate in a more open environment to reduce thermal effects from ambient air. In contrast, conventional telescopes in dome enclosures experience fewer wind-related deformations, but are more affected by thermal disturbances inside the enclosure, commonly referred to as *dome seeing*. Atmospheric turbulence is the biggest limiting factor if optimal maintenance, manufacturing and site conditions can be achieved. It therefore also has the largest band-pass frequency and frequency range [11].

Table 1.1: Sources of error that lead to a reduction in image quality of telescopes [11].

Source of error	Band-pass (Hz)
Optical design	d.c.
Optical manufacture	d.c.
Theoretical errors of:	
Mirror supports	d.c. $\rightarrow 10^{-3}$
Structure (focus, centering)	10^{-3}
Maintenance errors of the structure	
and mirror supports	10^{-5} (weeks)
Thermal distortions:	
Mirrors	10^{-4}
Structure	10^{-3}
Mechanical distortion of mirrors (warping)	10^{-6} (years)
Thermal effects on ambient air	$10^{-3} \rightarrow 10^{2}$
Mirror deformation from wind gusts	$10^{-1} \rightarrow 2$
Atmospheric turbulence	$2 \times 10^{-2} \rightarrow 10^{3}$
Tracking errors	$5 \rightarrow 10^{2}$

One possibility to counter some of these error sources is active optics. Due to thermal expansion, gravitational sagging or other environmental conditions there will be some form of mechanical deformation, which can be compensated by actively adjusting the shape and position of the optical elements of the telescope. This is achieved by continuously monitoring the optical elements and make precise adjustments through strategically placed actuators [1].

If the error is due to a distorting effect of an atmosphere turbulence then this can be compensated with the help of adaptive optics. Incoming light will always get slightly distorted due to variations in air density and temperature, which subsequently lead to a reduction in image-quality. By measuring the distortions and using deformable mirrors corrective adjustments can be calculated and applied in real-time. This can eliminate the undesirable effects of atmospheric turbulence to a high degree [13, 14].

These mechanical deformations and atmospheric turbulences are typically measured using wavefront sensors (WFS). Because the WFS requires a portion of the collected light, this method is generally only used for larger telescopes as light is already very limited in smaller telescopes.

With a primary mirror of 1.52 m the Leopold Figl-Observatory may be considered such a large telescope but currently does not utilise a WFS. It uses passive actuators for primary mirror stabilization, and has a rotating secondary mirror mount with two operational modes. However, this secondary mirror system lacks an active optics correction mechanism.

Additionally, the rotating secondary mirror mount was originally designed to support both Cassegrain and RC observing modes, but in recent years, only the RC mode has been actively used. This renders the heavy, movable components of the secondary mirror unnecessary, potentially introducing unwanted mechanical instabilities and alignment issues over time.

Furthermore, being over 50 years old, the LFO was built using design standards and materials that may not fully align with the standards applied to modern observatories.

As newer telescopes increasingly rely on active optics systems specifically designed for them, it remains an open question whether a more generalized design could be applied to enhance the performance of various telescopes, including older systems like the LFO.

1.2 Tasks and goals

The primary objective of this thesis is to measure the pose dependent alignment of the Leopold Figl-Observatory telescope, particularly in terms of imaging quality and mechanical uncertainties, as these two factors are somehow linked. Previous work has already explored a part of this task in a small telescope system [15]. However, it is not entirely clear whether this approach would scale effectively to a larger telescope, such as the Leopold Figl-Observatory. In addition to the previous work a WFS needs to be integrated into a telescope to verify the dimensional metrology results and perform the optical analysis. The goal of this thesis are thus as follows:

- Integrate and evaluate a WFS in an existing small RC-telescope system with an integrated dimensional metrology system.
  - Analyse and compare the measured imaging quality with the one estimated from the dimensional metrology system
  - Evaluate performance both with and without active optics compensation
- Scale, and integrate the dimensional metrology system into the Leopold Figl-Observatory.
  - Read out, record, and analyse measurement data
- Give an assessment of potential improvements of the LFO based on the results.

1.3 Outline

This thesis is structured as follows. Chapter 2 covers general telescope designs and where they are preferably used, methods of active optics and how it is realised in large telescopes. At the end the research questions are also defined. In Chapter 3 relevant theoretical background is covered and any used concepts are explained, as well as the functioning principle of the WFS is covered. The following two chapters cover the experiments setups and results, Chapter 4 contains a description of the small RC-telescope, how it was prepared for measurements, which measurement devices were used and why and how the experiment was performed. The second half covers all the results, the simultaneous dimensional metrology and WFS measurement while heating the system and while letting it cool back down. Chapter 5 then contains a description of the experiment setup and results at LFO. This includes any adapter designs that had to be created and manufactured. The results of the dimensional metrology system are presented and the WFS measurement was done on a different telescope, because maintenance work made a remote access impossible and after multiple unsuccessful attempts onsite due to weather conditions the concept was proven at a similar telescope from TU Wien. In the end Chapter 6 uses the results of the thesis to answer the previously defined research questions and a short outlook for possible improvements and potential for further research work is given.

2 State of the Art

The performance of a telescope is primarily determined by its ability to produce high-resolution images and accurate measurements under all operating conditions. However, various factors, such as mechanical stability, optical alignment, and environmental influences, can significantly degrade imaging quality. Large-aperture telescopes ($> 4\,\mathrm{m}$) are particularly susceptible to these effects. Therefore, to maintain diffraction-limited imaging quality, corrective measures are necessary, and advanced monitoring and correction techniques have been developed [1, 16].

This chapter examines state of the art techniques for quantifying the performance of telescopes, including precise measurement technologies and strategies for mitigating or compensating for performance degradations. At the end of the chapter research questions based on the previous findings are defined.

2.1 Telescope designs

There is a wide variety of telescope designs available, with each of them excelling in different scenarios. They can be categorized in lens-based and mirror-based telescopes, although there are also designs making use of both technologies. The following part will give a short overview of the available designs, their advantages and their typical uses in astronomy [16].

2.1.1 Refracting telescopes

Lens-based telescopes, also called refracting telescopes use lenses to bend incoming light and focus it onto an image plane. The largest lens is called the objective lens and the smaller lens is called the eyepiece lens, which is used for viewing. A simplified schematic of this is depicted in Figure 2.1. By using lenses the design suffers from chromatic aberration, which can be corrected for by adding another thin lens with a different dispersion behind the objective lens. Lenses are also very difficult and expensive to manufacture without any defects at large sizes [16]. Visible light is also dimmed a little when passing through a lens, this applies especially in the ultraviolet and infrared spectrum [17]. Since lenses can only be supported around the outside in the case of large heavy lenses they can potentially sag under their own weight [16].

Despite these drawbacks, refractors are still popular in amateur astronomy, due to their ease of use and their generally wider field of view [18].

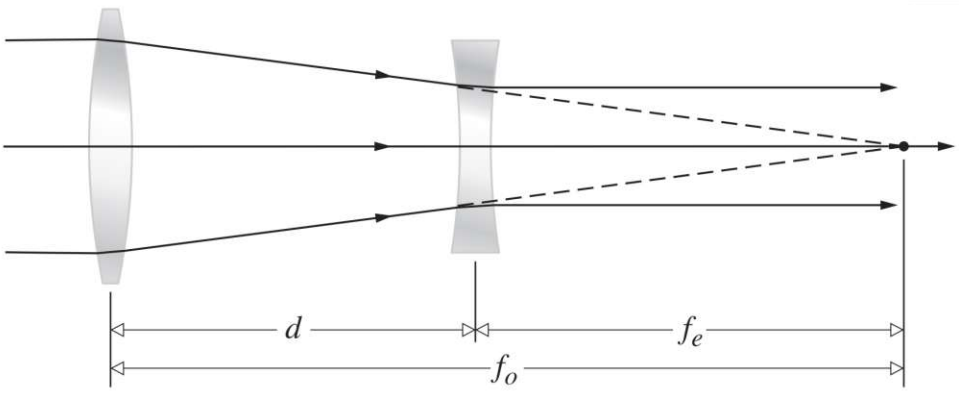

Figure 2.1: Simplified depiction of a lens based telescope design [16].

2.1.2 Reflecting telescopes

Mirror-based telescopes, also called reflecting telescopes, use curved mirrors to bend light and get parallel light rays coming from a far away point source to converge into a focus point. The focus is typically in the same path as the incoming light, although there are specialized off-axis mirror telescopes which direct the light somewhere else. To make an image from the mirror accessible from the outside there are several different ways of achieving that. One example is the Newtonian reflector, where a flat mirror is placed at an angle along the optical axis to point the light out to the side of the telescope towards an eyepiece, as visible in Figure 2.2 [16]. This design is rarely used in professional astronomy due to its bulkiness, but it is still popular in amateur astronomy [19].

A different way to solve the issue of where to focus the light is done by Cassegrain reflectors. They have a convex secondary mirror perpendicular to the optical axis and a hole in the middle of the primary mirror, where the light is focused through. Nasmyth telescopes combine the convex secondary mirror from the Cassegrain focus and the angled mirror from a Newtonian focus to focus the incoming light outside of the telescope [1, 16].

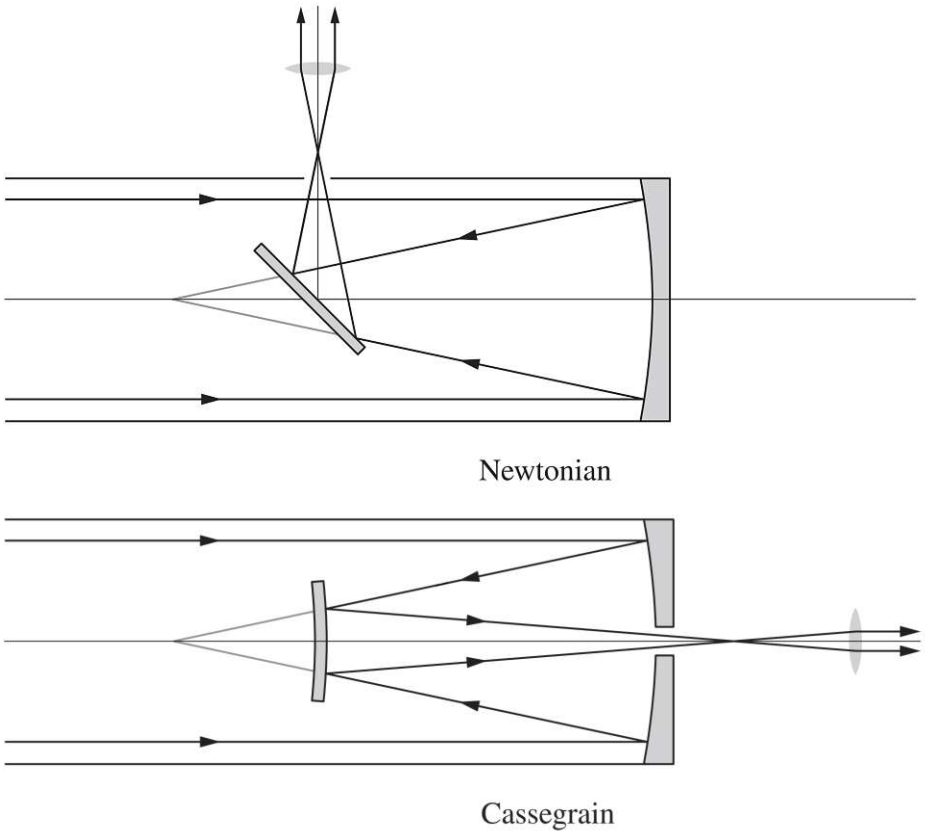

Figure 2.2: Simplified depiction of some reflective telescope designs [16].

Reflecting telescopes have many advantages over refracting telescopes and solve many of their issues. Due to the fact that mirrors are used instead of lenses the issue of chromatic aberrations as well as the difficulty to build large lenses are eliminated as mirrors are both cheaper and easier to build at large sizes. The mounting is also easier because the mount can attach to the back of the mirror. Since reflecting telescopes often have an open design with no protective tube enclosing the primary and secondary mirrors, they are more susceptible to environmental factors and require regular cleaning and recoating [1, 16].

The different mirror telescope designs use different shapes of mirrors. Parabolically shaped mirrors will focus the incoming light rays towards one point. This mirror shape however produces an aberration called coma, where off-axis point sources appear as asymmetric comet-like shapes. Spherically shaped mirrors are relatively easy to make, the focal length of a spherical mirror is however slightly different at different parts of the mirror, which results in some blurriness. Modern telescopes use mirrors in various shapes to reduce these errors. Some telescopes utilise both mirrors and lenses. Schmidt-Cassegrain telescopes for example use a spherical mirror as a primary mirror and a correcting plate at the entrance, which is supposed to correct for the spherical aberration of the primary mirror [1, 16].

The Ritchey-Chrétien Telescope (RC) is a more advanced design, which uses two hyperbolic mirrors as primary and secondary mirrors. This configuration, if aligned properly, can eliminate coma, producing very sharp images across a wide field of view. This design is often chosen for professional observatories, including the Hubble Space Telescope, due to their good image quality and suitability for large-scale imaging surveys [1, 16]. However, a drawback of the RC design is the complexity of mirror manufacturability. Since both the primary and secondary mirrors are hyperbolic, they are more difficult and expensive to manufacture compared to simpler designs. A schematic can be seen in Figure 1.1.

2.2 Metrology for telescope systems

Over the years, different methods have been developed to analyse and quantify telescope performance. Each method can improve the performance of a telescope in different ways [1]. The following section provides an overview of the most commonly used techniques and discusses their application in maintaining and optimising telescope performance.

2.2.1 Dimensional metrology system

Dimensional metrology systems are essential tools for measuring the relative positions, orientations and deformations of telescope components. These systems provide the precision required to align optical elements and maintain structural stability. Two common approaches are interferometry and laser alignment, each suited to specific measurement scenarios [1].

Laser alignment is generally done for longer distances, where less precision is sufficient. Interferometers are the most common choice for short range, high accuracy measurements. They work by splitting a laser beam into two paths: one directed at the component being measured and the other used as a reference. When the beams recombine, they create an interference pattern that varies with changes in the optical path length. This makes interferometry indispensable for tasks such as aligning segmented mirrors or measuring deformations in optical components [1, 20]. For example, the Keck Observatory uses interferometers to align its segmented primary mirrors to ensure they form a continuous optical surface [21]. Modern implementations, such as the laser-truss system used in the Large Binocular Telescope (LBT), utilise interferometric alignment in a large-scale telescope. This system operates over distances of up to 10 m with sub-micron precision and is specifically designed for general alignment tasks, such as monitoring slow structural deformations caused by thermal or gravitational effects. Data acquisition occurs every 10 seconds, making the system well-suited for tracking gradual changes rather than high-frequency aberrations. This is one part of the extensive active optics system of the LBT.

Unlike the wavefront sensors, which rely on light from the telescope, this part can operate independently, allowing alignment corrections even during non-observing conditions or daytime [22].

2.2.2 Wavefront sensing

Wavefront sensors provide another important method for monitoring telescope performance. Unlike dimensional interferometers, which measure mechanical parameters, wavefront sensors analyse the shape and phase of incoming light to detect optical aberrations. Shack-Hartmann sensors are among the most widely used wavefront sensing technologies. They divide incoming light into an array of sub-apertures, each focused onto a detector. The displacement of the focal spots reveals the local slopes of the wavefront, which can then be reconstructed into a detailed map of optical errors. Wavefront sensors are essential for applications like adaptive optics, where real-time correction of aberrations is required [13, 23]. For instance, the Gemini Observatory uses Shack-Hartmann sensors to correct atmospheric turbulence in real time, enabling near-diffraction-limited imaging [24]. Similarly, the Subaru Telescope employs wavefront sensors to deliver data to the adaptive optics system and control the deformable mirror. The scientists there also have a test bench to incorporate both an interferometer measuring the shape of the deformable mirror while the wavefront sensor and the adaptive optics systems adjust the shape to increase image quality [25]. Although wavefront sensors are highly effective for detecting both low-order and high-order aberrations, they take away light from the telescope otherwise usable for observation and are reliant on a reference star or artificial guide star to provide accurate measurements, which can complicate their implementation in certain conditions [13].

2.2.3 Measurement of environmental factors

Environmental conditions such as wind, humidity and temperature can affect the stability and performance of telescopes. These factors are monitored using dedicated sensors that provide real-time data on external conditions. Although environmental monitoring does not directly improve the performance of a telescope, it is an essential part of operational planning and necessary to support the safety of the operations [1].

Almost all large observatories, such as the European Southern Observatory, rely on environmental data to identify optimal observing conditions [26]. By selecting days with stable and favourable conditions, telescopes can minimise external disturbances that could degrade image quality or alignment stability. This approach ensures the best possible performance during observations, while avoiding unnecessary stress on compensation systems [1].

2.3 Compensation approaches

To counteract the influence of external effects, active compensation systems are installed to correct any misalignments or optical aberrations caused by deformations of the telescope structure in real-time [27]. These systems are not only used to ensure a good alignment between the primary and secondary mirrors, but also to actively correct higher order terms by manipulating the shape of the mirror and to achieve a higher image quality [28].

Different types of compensation systems target specific components of the telescope, usually only the primary mirror, the secondary mirror, or the supporting structures are

of interest. Key technologies in this area include actuation systems, hexapod structures, and adaptive optics. These systems are usually custom tailored for each specific telescope and primarily employed in large observatories. In most cases they rely on light from the telescope itself as feedback for the control system.

The following section will give an overview of these systems, their principles, and provide an example of their usage in modern telescopes [1].

2.3.1 Primary mirror system

The primary mirror system will be considered first. A distinction is usually made between an axial part (on the mirror surface) and a lateral part (on the edge of the mirror in most meniscus mirrors). In active optics systems, these parts are controlled using actuators to maintain optimal mirror shape. There are also systems in which the two principles are combined.

Axial support system The axial support system system is used to support the mirror weight along the optical axis and to correct low-order modes [29]. Figure 2.3 shows an example of this arrangement, where the primary mirror is highlighted in green. To simplify the design, the supports are usually arranged in concentric rings. By pushing and in rare cases also pulling the supports, controlled forces are applied to the back of the mirror to obtain the appropriate shape to compensate for the aberrations. The distribution and number of supports and forces is determined by an optimisation problem. The main criterion for this is the minimisation of the RMS deformation when the mirror is at rest on the axial supports. The support system is usually realised with electromechanical pressure actuators. These have the advantage of precise controllability and low costs. Figure 2.3 also shows the axial fixed points in red, which determine the axial position of the mirror. In addition, they bear the force imbalance due to inaccuracies in the force settings of the active supports [29].

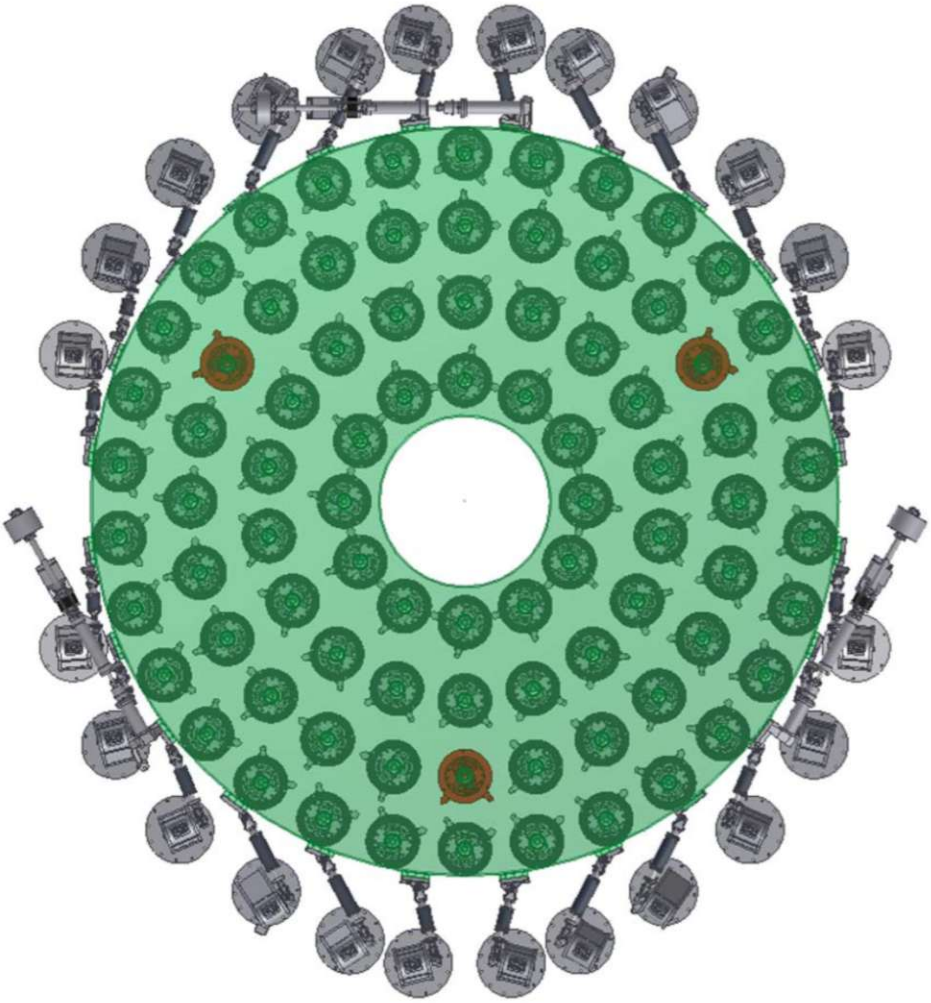

Figure 2.3: Schematic presentation of an axial and lateral actuation system [29].

Lateral support system The lateral support system holds the weight of the mirror perpendicular to the optical axis. It is typically based on passive systems and three lateral fixed points that define the position of the mirror in the x-y plane [29].

2.3.2 Secondary mirror system

The hexapod shown in Figure 2.4 can be used to position the secondary mirror in six degrees of freedom. This is a parallel robot with six degrees of freedom, x, y, z, ϕ, θ and ψ. The angles ϕ and θ describe the rotation around the x and y axes, while ψ describes an additional rotation around the optical axis. The hexapod has six linear motors that connect a fixed platform to a mobile platform. The fixed platform is connected to the telescope structure, while the mobile platform is connected to the secondary mirror. The motors adjust the length of the links so that the mirror is in the desired position [30]. This means that the hexapod can now be used for translation along the optical axis for focusing, tilting around the centre of curvature of the mirror for coma correction, and tilting around a neutral point for tilt reduction in the image [31]. The possibility of applying this concept to smaller telescopes is limited by the size and complexity of the hexapod.

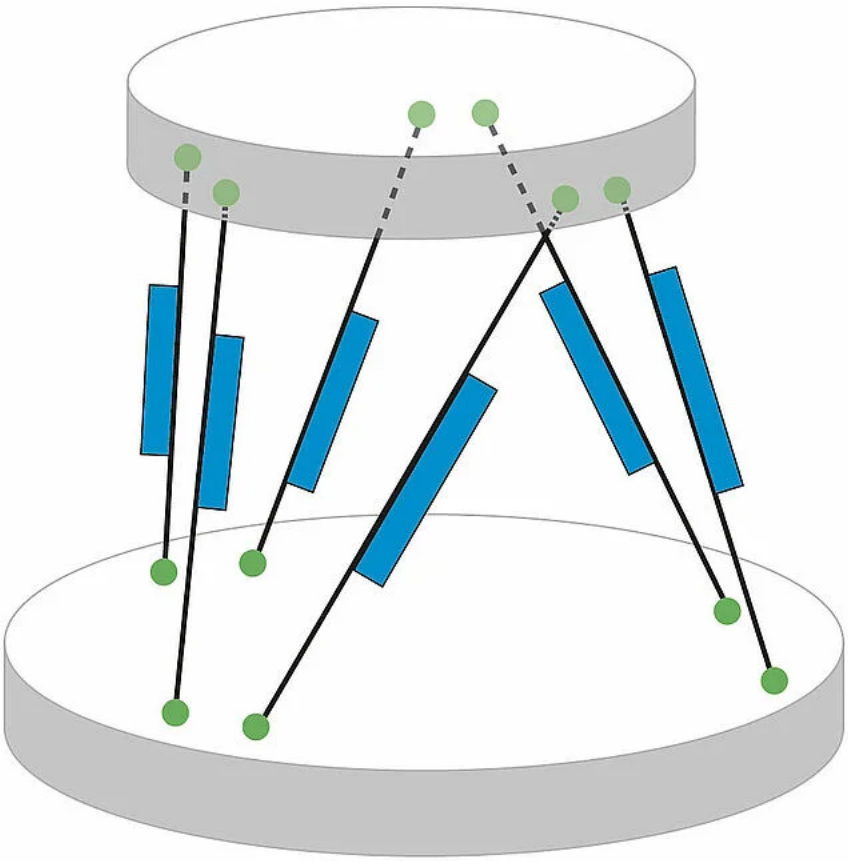

Figure 2.4: Schematic presentation of a hexapod [32].

The secondary mirror system of the New Technology Telescope (NTT), a large telescope, has the ability to actively position the secondary mirror in three degrees of freedom. After a long search in the publications on the active optics of the NTT, no more detailed description of the actuation of the secondary mirror could be found. However, a three-degree-of-freedom approach can also be effective and, more importantly, easier to implement in smaller telescopes, as demonstrated by the work on a small RC-telescope in [15].

2.3.3 Adjusted secondary mirror system

However, the design of the hexapod has some disadvantages, which is why the concept was modified. Due to the volume limitations of the individual connections, they cannot be positioned anywhere between the two platforms. This is particularly noticeable when positioning at small angles [33]. In addition, the entire mass of the actuator is distributed over only two joints, which has a negative effect on the dynamic behaviour [33]. For this reason, an extension as shown in Figure 2.5 was implemented in new telescopes. The linear motors are connected to the base plate along a hexagon. Each actuator can exert both a compressive force and a tensile force on the hexagon, which transmits the force to an inclined connection. This is connected to the hexagon by a flexible pivot point. At the other end, the six connections are again attached to three points with a flexible pivot point. By combining the control of all linear motors, movement can now be performed in the six degrees of freedom. Vertical movements in particular (for focusing) can be

carried out directly by the linear motors without coupling with other degrees of freedom or interfering lateral forces [33].

Figure 2.5: Schematic presentation of an advancement to a standard hexapod [15].

2.3.4 Actuation of the secondary mirror mounting

Another possibility is the actuation of the secondary mirror mount in combination with the active mounting of the secondary mirror. Figure 2.6 shows the concept of the Discovery Channel Telescope (DCT) [34]. The secondary mirror is attached to the lateral positioners and is actuated with very high accuracy by the three drive units. However, only the piston and tip/tilt can be corrected. To move the remaining degrees of freedom, the secondary mirror is carried by a vacuum system with three axial and one radial post [35]. Very fast and precise positioning is possible with this configuration. However, in the event of a fault in the vacuum system, the posts would damage the secondary mirror, which is why additional pressure relief measures are necessary.

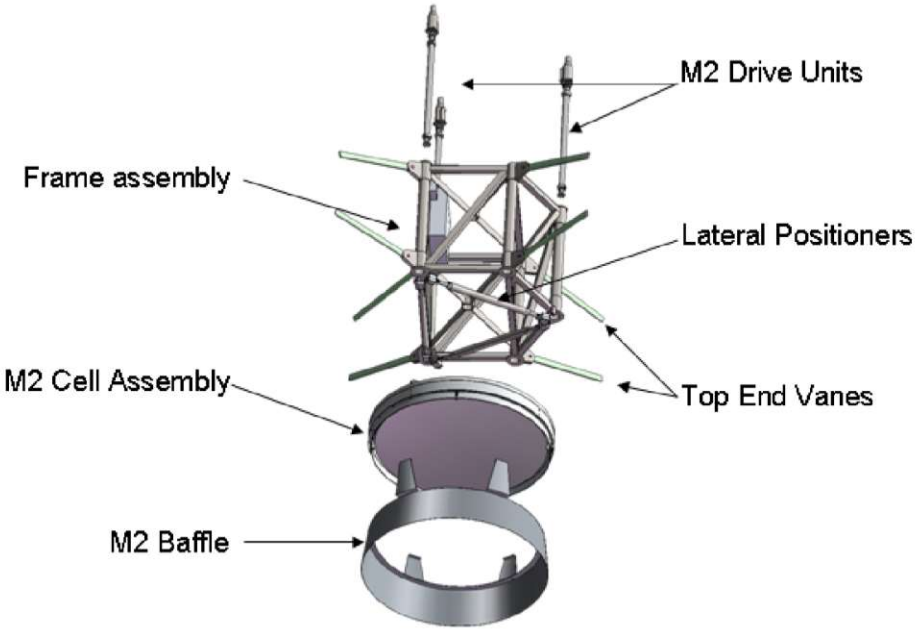

Figure 2.6: Secondary mirror structure of the DCT [34].

A similar approach was used in the development of an active optics system for a small RC-telescope, as presented in [15], which is also used in this thesis. Active optics systems are typically designed for large telescopes and are custom built, often integrating WFS to provide real time optical correction. However, WFS require a portion of the telescope's light, making them less suitable for small telescopes where available light is highly valuable.

To overcome this limitation, the system replaces wavefront sensing with a dimensional measurement system, that determines the relative position of the primary and secondary mirrors without directly taking light away from the telescope. The system integrates actuators into the secondary mirror mounting, allowing for precise control of the mirror in three degrees of freedom, ensuring optimal alignment while preserving all of the collected light for the scientific application.

2.3.5 Adaptive optics systems

Adaptive optics systems are important for real-time corrections of optical aberrations caused by atmospheric turbulence and mechanical distortions. These systems consist of three primary components: a wavefront sensor, a deformable mirror, and a control system. The wavefront sensor measures the shape of the incoming wavefront, the control system calculates the necessary adjustments, and the deformable mirror then compensates for the aberrations by altering its shape accordingly [13].

The principle of adaptive optics is based on the wavefront sensor, i.e. a Shack-Hartmann wavefront sensor. The wavefront error, is then corrected by the deformable mirror. This mirror, composed of many small actuators, changes its surface shape to counteract the measured aberrations.

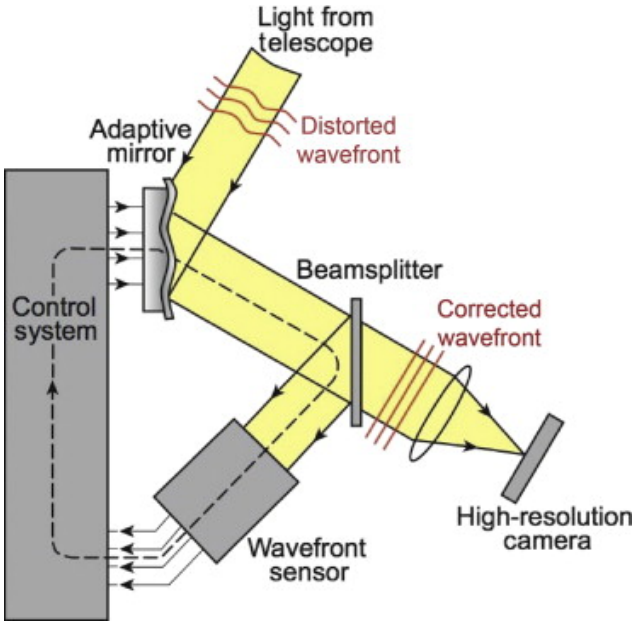

Figure 2.7: Graphic visualisation of an adaptive optics system [36].

Adaptive optics systems can significantly improve image quality, especially for ground-based telescopes that have to deal with atmospheric turbulence. However, these systems are complex and expensive, requiring high-speed control systems and deformable mirrors with many actuators [13]. Figure 2.8 shows an example of a picture taken from Uranus in the near infrared light without utilizing an adatpive optics system (left) and with the system turned on (right). This gives an idea of how well adaptive optics can improve image quality.

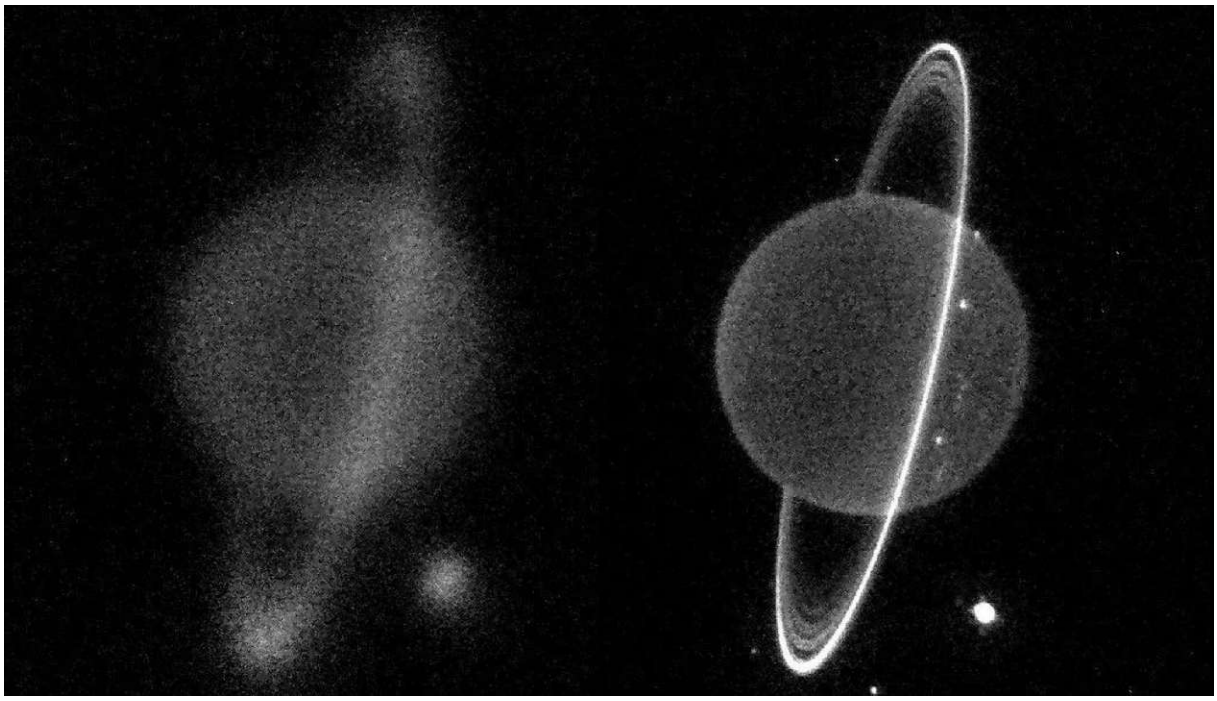

Figure 2.8: Comparison of an image of Uranus without (left) and with AO (right) by Heidi B. Hammel and Imke de Pater [37].

2.3.6 Compensation systems for thermal expansion

Large ground-based telescopes use temperature sensors to monitor ambient conditions and thermal gradients across their structure. This data is used to automatically adjust the position of optical elements, such as the secondary mirror, to minimize defocus and other thermally induced aberrations. In practice, every absolute temperature value can correspond to a predefined adjustment along the optical axis for the secondary mirror to maintain good focus [5, 38].

Cooling and heavy thermal shielding are not commonly used because these systems are costly and impractical. More importantly, their effectiveness depends on the telescope's operating conditions. Large ground-based observatories, which primarily operate at night, experience relatively gradual cooling after sunset, where local temperature differences rather than absolute temperature levels are the main contributors to image degradation. As a result, active cooling systems offer limited benefits under these conditions [5].

However, for telescopes operating in rapidly changing thermal environments, such as during sunset transitions or daytime observations, cooling and thermal shielding can be more impactful. Instead of direct cooling, most observatories focus on minimizing thermal gradients by using low thermal expansion materials (e.g., Zerodur) and airflow control systems, which are simpler and generally more effective for maintaining optical performance over extended periods [5].

When large thermal gradients do occur, they degrade image quality through two primary mechanisms: mirror seeing and dome seeing. Mirror seeing arises from turbulent air layers forming near the primary mirror due to temperature differences between the mirror and surrounding air. Dome seeing results from turbulence caused by temperature differences between the enclosed air and the external atmosphere. Warmer mirrors have been shown to significantly degrade image quality, whereas cooler mirrors (up to 2.5 °C below ambient air) have a negligible impact. Dome seeing, while generally less critical than mirror seeing, can still contribute to image degradation, particularly in older domes with insufficient ventilation [5].

To mitigate thermal effects, modern telescopes use active ventilation and optimized enclosures. The ESO 3.5 m NTT features a semi-open design with removable walls that enhance natural ventilation and reduce thermal gradients. The Multiple Mirror Telescope's (MMT) fully open-top enclosure follows a similar approach, improving airflow and limiting heat buildup. In contrast, older telescopes, such as Bowen-class designs, required retrofitting with cooling systems and airflow controls due to poor ventilation [5].

Active cooling of primary mirrors remains rare due to cost and complexity, though some telescopes, like the Canada-France-Hawaii-Telescope (CFHT), have tested ducted air cooling. Reflective coatings and low-emissivity treatments, such as aluminium foil, are also used to reduce radiative heat loss [5].

However this does not mean that active cooling is not done at all. Among the main methods for active temperature compensation are liquid cooling systems and thermally controlled optical elements. The Daniel K. Inouye Solar Telescope (DKIST) utilises a reflective-absorptive thermal stop, where both the reflector and absorber are actively cooled to keep the temperature rise within 6 K above ambient air. Similarly, the European Solar Telescope (EST) features a flat-plate reflective thermal stop, which maintains a controlled surface temperature using a jet impingement cooling method to stay within 8 K of ambient air [38].

Recent telescope designs favour low-profile, open enclosures that promote wind flushing, which effectively disperses hot air layers and improves image quality. Unlike older

domes that prioritized height, modern enclosures are optimized for ventilation, yielding superior performance [5].

2.3.7 Summary

Active optics are a powerful tool for improving telescope performance by compensating for misalignments and optical distortions. However, these systems are typically custom-built for large telescopes, making them complex, expensive, and not commercially available as off-the-shelf solutions.

A key limitation of conventional active optics is the reliance on WFS, which require a portion of the telescope's light for feedback. While this is feasible in large observatories, it poses a significant challenge for smaller telescopes, where light is a crucial and limited resource. As a result, active optics systems are rarely implemented in small telescopes, despite the fact that they suffer from many of the same disturbances as larger ones.

Furthermore, smaller telescopes are more likely to be used in daytime observations, mobile applications, or fast-tracking scenarios, where traditional WFS-based solutions may not be practical.

2.4 Leopold Figl-Observatory

The Leopold Figl-Observatory (LFO), named after the then former Chancellor of Austria and Governor of Lower Austria, is located southwest of Vienna, Austria near the highest mountain of the Wienerwald at 883 m. The plan for an outstation of the Vienna University Observatory was realised in order to escape the disturbing influences of the city. Scientific use of the observatory began in December 1970. The optical elements of the 1.5 m Ritchey-Chretien telescope were manufactured by the Carl Zeiss company in Oberkochen (Germany). The diameter of the primary mirror is 1.52 m and the mirror weight is 1 tonne. The focal length of the telescope is 12.5 m. The telescope mechanism was manufactured by Rademakers in Rotterdam (Netherlands). The total weight of the telescope is 23 t. The telescope control system, based on a LabVIEW RT kernel and hardware from National Instruments, was developed at the Vienna University Observatory.

The Leopold Figl-Observatory for Astrophysics is used for astronomical research, for teaching as part of the astronomy degree programme at the University of Vienna and for public relations work.

Figure 2.9: LFO as seen from outside [39].

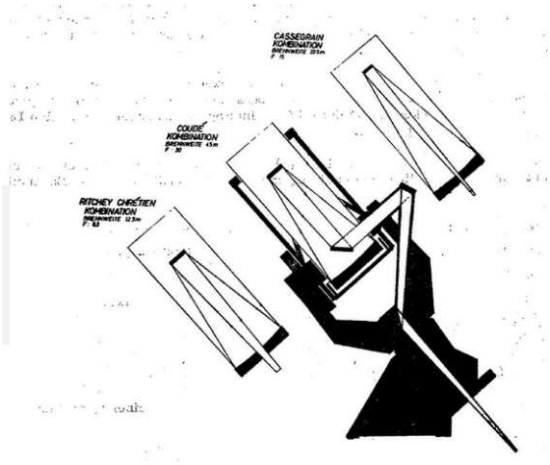

Figure 2.10: Different lightpaths of LFO [39].

The telescope was originally designed to be a versatile observing instrument that could be used for as many different observing programmes as possible.

It has 3 light paths:

- RC focus: wide-field imaging (correction of image field curvature using an achromatic lens)
- Cassegrain focus: spectroscopy
- Coudé focus: high-resolution spectroscopy

However, only the Cassegrain and RC focus were equipped with instruments. The Coudé focus was never used. A direct change from the Cassegrain to the RC light path is possible by means of a rotating device of the secondary mirror cells ("flip-flop"). In current operation, only the RC focus is used. In Table 2.1 the technical specifications of the different focusing mechanism can be seen. D/f is the relative aperture, which describes the ratio of the focal length to the aperture and determines the light-gathering speed and magnification. FoV is the field of view, which gives the angular size of the sky observable in a single image. D_1 and D_2 are the diameters of the primary and secondary mirror respectively and g is the back focal distance, the distance from the secondary mirror to the focal plane, which is essential for instrument placement [16].

Table 2.1: Technical data of different lightpaths [39].

Light Path	D/f	FoV	D_1 $[mm]$	D_2 $[mm]$	g $[mm]$
Cassegrain	$f/15$	$0.5° \times 0.5°$	1524	323	750.5
Ritchey-Chrétien	$f/8.3$	$1.0° \times 1.0°$	1524	519	750.2
Coudé	$f/30$	$0.1° \times 0.1°$	1524	467.5	10853.6

As a mounting option the fork type in an equatorial configuration was chosen. The telescope tube is designed as a central segment with two outer segments for the main and

secondary mirrors. The outer segments are connected with Serrurier struts, which ensure a position-independent collimation of the optical system within a tolerance of ±0.1 mm. The total weight of the moving parts is 20 t [39].

In recent years, concerns have arisen regarding the image quality produced by the telescope, which seems to fall short of what could be expected from a telescope of its size. While there were no expectations when the telescope was first built that it would make breakthrough discoveries, operators have noticed that its performance does not meet current standards, and the reasons for this remain unclear. It is suspected that mechanical or optical factors within the telescope design may be contributing to this, though the exact cause has yet to be determined.

One potential issue lies in the telescope's secondary mirror mounting, which was originally designed to accommodate the different operational modes. The secondary mirror is supported by a heavy and robust structure, designed to handle a range of observing configurations, though only the RC mode is in use today. This mounting system, while offering versatility, could now only add unnecessary weight to a point that is particularly sensitive and difficult to stabilize, as that is where the longest lever is. This can potentially introduce alignment issues or mechanical instabilities. Since the telescope only operates in RC mode, the current secondary mirror setup could be rebuilt and made lighter as it may no longer be essential and could even be contributing to the degradation of image quality by adding complexity and weight that disturb the mirror's alignment.

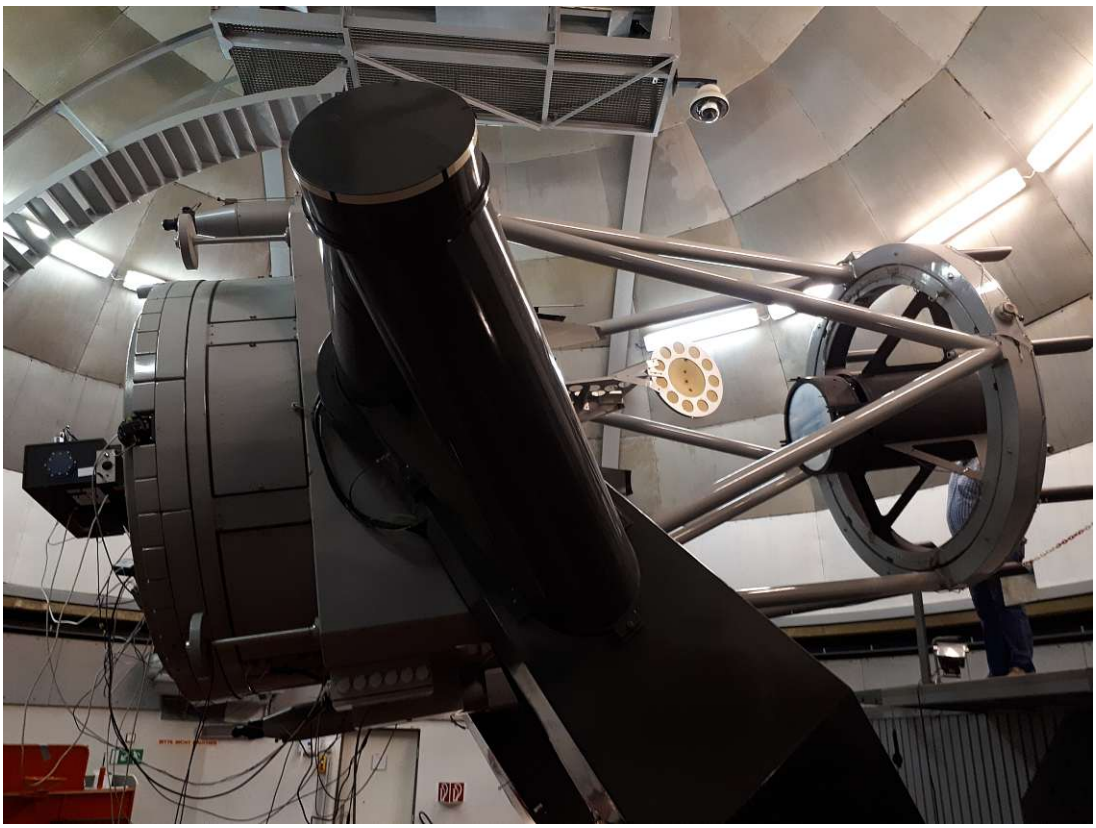

Figure 2.11: LFO from inside the dome.

Given these concerns, the research in this thesis is focused on conducting a detailed assessment of the telescope's performance by performing a series of dimensional measurements and proving a way to do more optical measurements, which could then help to explain what contributes to the image quality issues. This data can then be used in

the future to make decisions on how to potentially alter the telescope design, whether modifications to the design, particularly the removal or redesign of the secondary mirror mounting could help improve the overall performance of the telescope. Ultimately, ensuring that the Leopold Figl-Observatory remains an important resource for both research and education.

2.5 Research questions

Before starting any measurements the system first needs to be properly understood. This leads to the first research question.

Research question 1. *What are the factors limiting imaging quality at the Leopold Figl-Observatory?*

One key aspect of telescope performance is the precise alignment of optical components. Mechanical deformations, whether caused by gravitational sag, thermal expansion, or operational movements, can result in misalignment that directly impact image quality. To monitor and track any positional changes, dimensional metrology is well suited. However, its effectiveness in a large-scale environment such as the LFO needs to be tested. This leads to the second research question:

Research question 2. *Can the expected distance changes between primary and secondary mirror of the Leopold Figl-Observatory be effectively measured with dimensional metrology?*

Besides a mechanical analysis a WFS can additionally provide an optical analysis. How well the WFS can operate in the given conditions and how well the WFS can be incorporated at the LFO also needs to be tested. This leads to the last research question:

Research question 3. *Is a wavefront sensor suited to monitor image quality despite atmospheric turbulences?*

3 Theoretical background

This section aims to give a comprehensive overview of the necessary theoretical background and quantities that are used in the process of this thesis. For this purpose, imaging-quality, options of quantifying it, and the principle of wavefront sensing are considered.

3.1 Imaging-quality

A imaging setup generally consists of an object plane, an optical system and an image plane. Typically the optical system includes lenses and an aperture. The entrance and exit pupil are the images that are formed by the optics either in front or behind the aperture, as can be seen in Figure 3.1 [40]. In astronomy light sources are very far away from the observer, which is why it can be assumed that the incoming light rays will be parallel [5]. The wavefront is always perpendicular to the geometrical rays. A wavefront is defined as the set of points, where each point has the same phase. In our case, since we have light coming from infinity, the wavefront is a plane. In the shown scenario there are no aberrations after propagating through the lenses the wavefront changes to a spherical one and all the light rays converge to a single point. This is not true for any real optical system, since there will always be aberrations, which will cause the wavefront to deviate from a spherical shape [40].

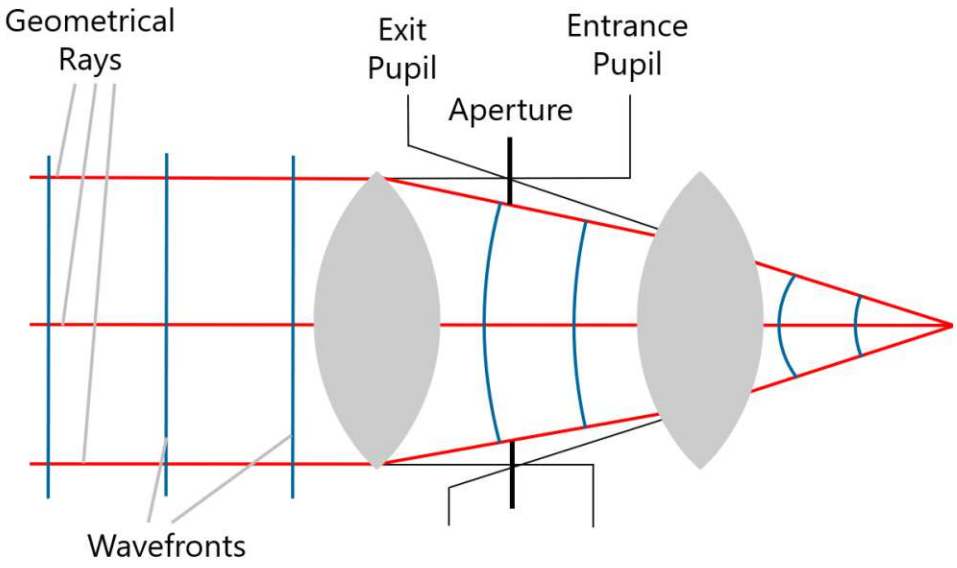

Figure 3.1: Geometrical ray trace of a general optical system.

Snell's law describes the refraction of light when interacting with optical surfaces. It is given partly by the sine function $\sin(\phi) = \sum_{n=0}^{n}(-1)^n \frac{\phi^{2n+1}}{(2n+1)!}$, which is non-linear. Therefore aberrations also occur with perfectly spherical lenses or when inserting a perfectly plane plate perpendicular to the optical axis of a converging or divergent beam of light. The wave aberration function $W(x, y)$ is expected to follow a similar pattern. It gives the distance that the wavefront deviates from a reference spherical wavefront [40].

$$W(r,\theta) = W_{020}r^2 + W_{040}r^4 + W_{131}hr^3\cos\theta + W_{222}h^2r^2\cos^2\theta + W_{220}h^2r^2 + W_{311}h^3r\cos\theta + ...(higher\ order\ terms) \quad (1)$$

W_{klm} represents the wave aberration coefficients, h is the object height, and r and θ describe the polar coordinates of the pupil plane.

The terms in the Taylor series do not form an orthogonal set of basis functions and are therefore not suited for data fitting or describing measurements of experiments [40].

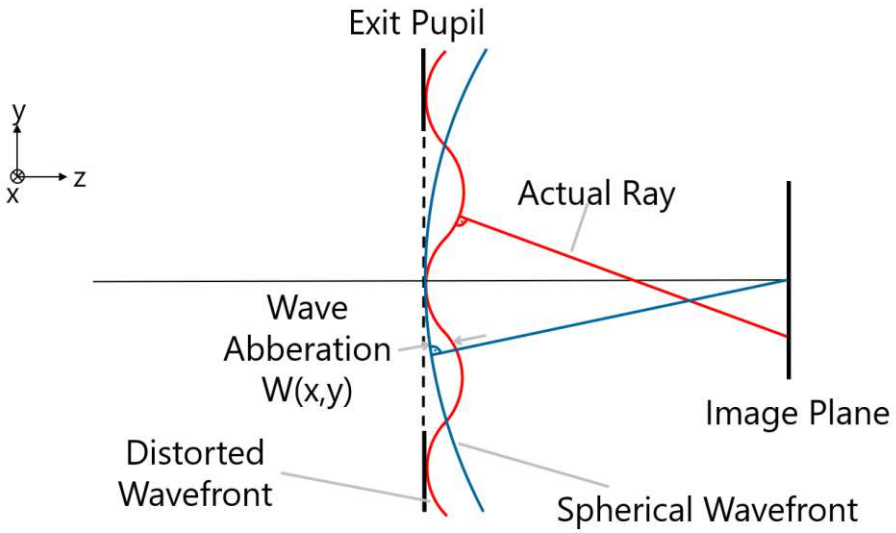

Figure 3.2: Visual representation of the wave aberration function.

3.2 Zernike polynomials

Zernike polynomials are widely used in optical science, since they form a complete orthogonal set of functions over a unit circle. This characteristic makes them suitable for fitting data. Since many optical system use circular pupils (e.g. telescopes) it is convenient to have a set of functions that form a basis and are orthogonal over the interior of a circle. They are therefore often expressed in polar coordinates but are easily convertible to Cartesian coordinates.

The definition of the Zernike polynomials is given by,

$$\begin{aligned} Z_n^m(\rho,\theta) &= N_n^m R_n^{|m|}(\rho)\cos(m\theta) \quad \text{for } m \geq 0,\ 0 \leq \rho \leq 1,\ 0 \leq \theta \leq 2\pi \\ &= -N_n^m R_n^{|m|}(\rho)\sin(m\theta) \text{ for } m < 0,\ 0 \leq \rho \leq 1,\ 0 \leq \theta \leq 2\pi. \end{aligned} \quad (2)$$

Equation 2 shows that each polynomial consists of three components. N_n^m normalises the polynom such that $\int_0^{2\pi}\int_0^1 Z^2\rho d\rho d\theta = \pi$, $R_n^{|m|}$ is a radially dependent polynom and the third component is an angular function of the azimuthal-angle. The index n indicates the highest order of the radial polynomial $R_n^{|m|}$ and m indicates the frequency of the angular function. A third index j is employed to specify the mode number [40].

Comparing Equation 1 and Equation 2 it is visible that the original form of the wave aberration function is still preserved in the different Zernike polynomials.

In some instances it is preferable to express the Zernike polynomials in a Cartesian form. The data from Shack-Hartmann Wavefront Sensors for example is calculated via the partial derivatives of wave aberration function with respect to x and y. Table 3.1 lists the Zernike polynomial up to the 4th order and their meaning in relation to the Seidel or Primary aberrations. These are directly related to the visualisation in Figure 3.3 [40, 41].

Table 3.1: List of Zernike polynomials up to the 4th order [40].

Mode j	Order n	Frequency m	$Z_n^m(\rho,\theta)$	Meaning
0	0	0	1	Constant term, or Piston
1	1	-1	$2\rho\sin(\theta)$	Tilt in y - direction, Distortion
2	1	1	$2\rho\cos(\theta)$	Tilt in x– direction, Distortion
3	2	-2	$\sqrt{6}\rho^2\sin(2\theta)$	Astigmatism with axis at $\pm 45°$
4	2	0	$\sqrt{3}\,(2\rho^2-1)$	Field curvature, Defocus
5	2	2	$\sqrt{6}\rho^2\cos(2\theta)$	Astigmatism at $0°$ or $90°$
6	3	-3	$\sqrt{8}\rho^3\sin(3\theta)$	
7	3	-1	$\sqrt{8}\,(3\rho^3-2\rho)\sin(\theta)$	Coma along y - axis
8	3	1	$\sqrt{8}\,(3\rho^3-2\rho)\cos(\theta)$	Coma along x - axis
9	3	3	$\sqrt{8}\rho^3\cos(3\theta)$	
10	4	-4	$\sqrt{10}\rho^4\sin(4\theta)$	
11	4	-2	$\sqrt{10}\,(4\rho^4-3\rho^2)\sin(2\theta)$	Secondary Astigmatis m
12	4	0	$\sqrt{5}\,(6\rho^4-6\rho^2+1)$	Spherical Aberration, Defocus
13	4	2	$\sqrt{10}\,(4\rho^4-3\rho^2)\cos(2\theta)$	Secondary Astigmatism m
14	4	4	$\sqrt{10}\rho^4\cos(4\theta)$	
⋮	⋮	⋮	⋮	

The wave aberration function can also be expressed via Zernike polynomials:

$$\begin{aligned} W(\rho,\theta) &= \sum_{n=1}^{k}\sum_{m=-n}^{n} W_n^m Z_n^m(\rho,\theta) \\ &= \sum_{n=1}^{k}\left[\sum_{m=-n}^{-1} W_n^m\left(-N_n^m R_n^{|m|}(\rho)\sin(m\theta)\right) + \sum_{m=0}^{n} W_n^m\left(N_n^m R_n^{|m|}(\rho)\cos(m\theta)\right)\right], \end{aligned} \tag{3}$$

where k is the polynomial order, W_n^m is the coefficient to the corresponding Z_n^m mode.

For calculations it is often more convenient to use Cartesian coordinates and a single indexing scheme:

$$W(x,y) = \sum_{j=0}^{j_{\max}} W_j Z_j(x,y) \;\text{ where }\; W_j = W_n^m \;\text{ and }\; Z_j(x,y) = Z_n^m(x,y) \;\; j = \frac{n(n+2)+m}{2},$$

where $j_{\max}$ is supposed to be the highest mode number in the expansion.

Figure 3.3 displays the first 21 Zernike polynomials, each represented as a wavefront pattern, corresponding to individual modes of optical aberrations. Each polynomial is

labelled by its specific order and type, such as piston, tilt, defocus, astigmatism, coma, or spherical aberration. To easier relate the polynomials to an aberration Z_n^m can be cross-referenced with Table 3.1 above. The patterns show variations in phase or optical path difference across the aperture, where regions in the direction of blue or red indicate negative and positive deviations from a reference wavefront.

Lower-order Zernike modes, such as tilt and defocus, show simpler, large-scale distortions. Tilt shifts the wavefront linearly across the aperture, while defocus introduces a symmetric ring pattern. Higher-order modes like astigmatism and coma introduce more complex shapes, including asymmetric or elliptical distortions, representing how these aberrations affect the image quality [40]. This is also shown in Figure 3.3, where the wavefront distortion is visualized. Red indicates a positive deviation, which means the wavefront is above the reference plane, blue means the opposite and green represents the neutral point where there is no deviation from the reference plane.

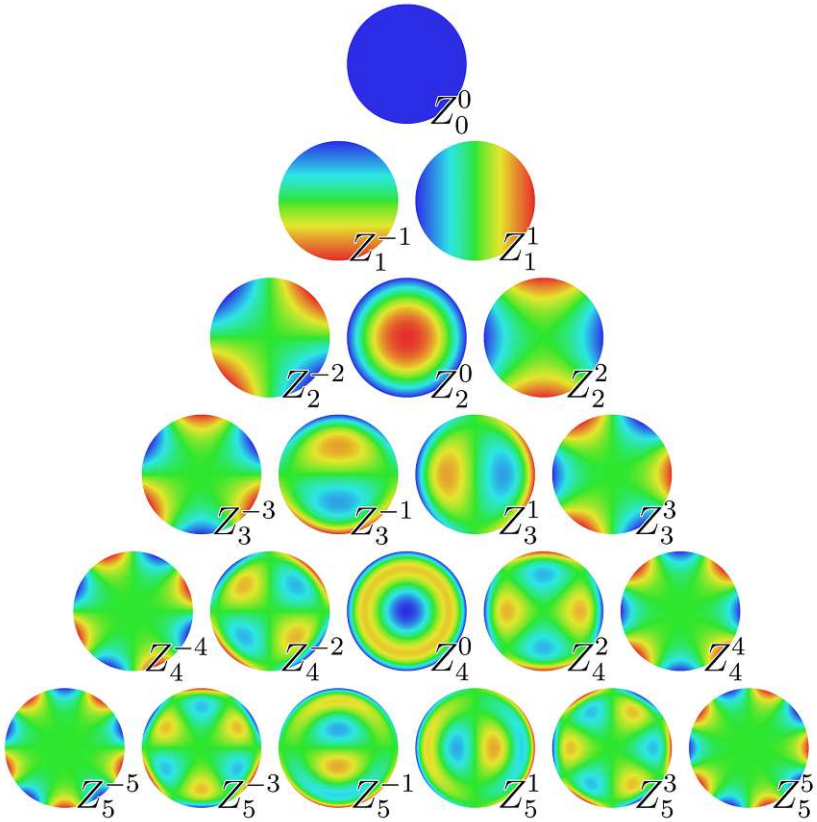

Figure 3.3: Visualisation of the first 21 Zernike polynomials, arranged vertically by radial degree and horizontally by azimuthal degree [42].

3.3 Strehl ratio

Since no optical system is aberration free, there is always a loss in imaging quality, affecting crucial metrics such as the Point Spread Function (PSF) and the Strehl ratio [40].

Point spread function (PSF)

The PSF represents the response of the optical system to a point source, such as a distant star, and serves as a measure of the system's resolution. In an ideal, aberration-free

system, the PSF forms a compact, symmetric shape with a single central peak, known as the Airy disk, surrounded by faint rings. Aberrations alter the PSF, causing it to spread out, become asymmetric, or shift from the central point. This spreading diminishes the intensity of the central peak, reducing the system's ability to resolve fine details [43].

Strehl ratio

The Strehl ratio is a metric that quantifies the optical quality of an imaging system by comparing the central irradiance of the observed PSF in the presence of aberrations to that of a diffraction-limited (ideal) PSF, where no aberrations were present. It is defined as the ratio:

$$\text{Strehl ratio} = \frac{I}{I_0} \tag{4}$$

where I is the intensity at the central irradiance of the measured PSF, and I_0 is the peak intensity of a theoretical, aberration-free PSF. A Strehl ratio close to 1 indicates high optical quality with minimal aberrations, while lower values suggest significant deviation from the ideal. In general optical systems like telescopes, a Strehl ratio of 0.8 or higher, which corresponds to a wavefront error of $\lambda/14$, is considered well corrected and is called diffraction limited [13, 43].

In case of small RMS wavefront errors the Strehl ratio can be approximated as,

$$\text{Strehl ratio} \approx e^{-\left(\frac{2\pi\sigma}{\lambda}\right)^2}, \tag{5}$$

where σ is the root mean square wavefront error, and λ is the wavelength of light being used [44].

This formula provides a close estimate of the Strehl ratio for systems with low levels of aberration, where the RMS wavefront error is small. For larger wavefront errors, this relationship becomes less accurate, as it does not fully capture the complex effects of severe aberrations on the PSF [43].

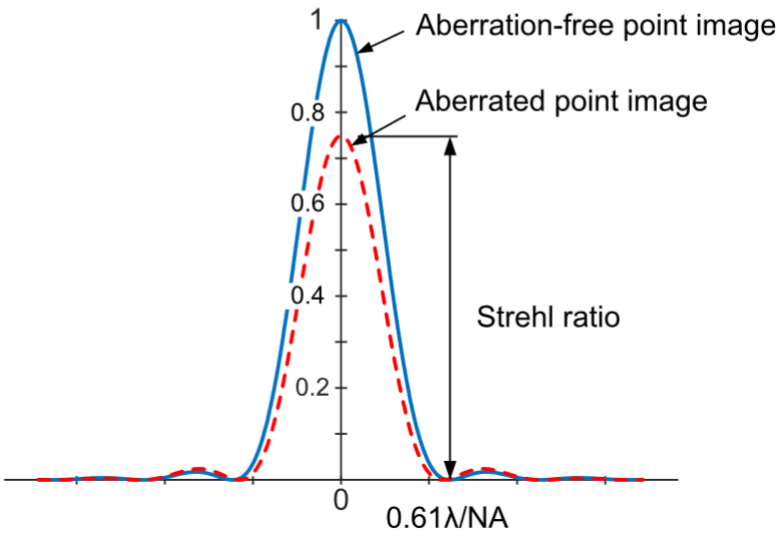

Figure 3.4: Plot showing an irradiance distribution normalized by its aberration free value, visualising the Strehl ratio [43].

3.4 General aberration theory

Aberrations are deviations from the ideal wavefront shape and are a common source of imaging degradation in telescope systems. These deviations cause the wavefront to differ from the desired spherical or plane form, leading to a range of image distortions. Aberrations can be systematically categorized and analysed using Zernike polynomials, which are well-suited for describing optical errors in systems with circular pupils [1, 16].

The most prominent aberrations affecting telescopes are shortly described below, each impacting image quality in distinct ways.

Defocus

Defocus occurs when the image plane does not coincide with the intended focal plane, causing the wavefront to deviate symmetrically along the optical axis. This results in a blurred image as light rays converge either before or after the image plane, leading to an expanded, circular PSF. In telescopic systems, defocus is one of the primary aberrations that can be mitigated by adjusting the position of the mirrors [45].

Tip/Tilt aberrations

Tip and tilt are simple shifts of the entire wavefront, effectively moving the position of the image without significantly changing its shape. These are low order aberrations and in many systems they are compensated for by adjusting the pointing of the telescope or by making small corrections to the optical alignment. Since they don't deform the PSF itself, their effect on image quality is minimal once the image is recentred. Therefore, when analysing wavefront quality, tip and tilt are often removed or compensated for, allowing the focus to be on higher order aberrations which have a more direct effect on resolution and Strehl ratio [5].

Coma

Coma is an aberration that causes off-axis point sources to appear as asymmetric, comet-like shapes. It is caused by differences in magnification between rays passing through different parts of the optical system, resulting in an elongated PSF with a 'tail' on one side. Coma becomes more pronounced for objects further from the optical axis and is particularly important in wide field applications where image quality across the full field is important [16]. The ligthpath is visualised in Figure 3.5 and the result can be seen in an example picture in Figure 3.6.

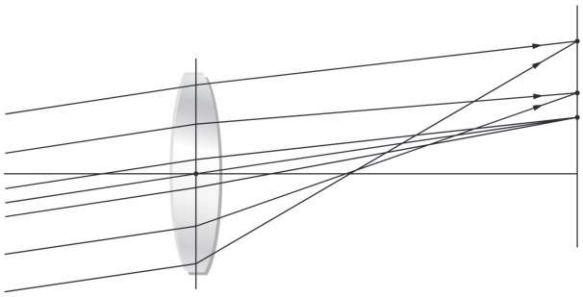

Figure 3.5: Light path in case of coma [16].

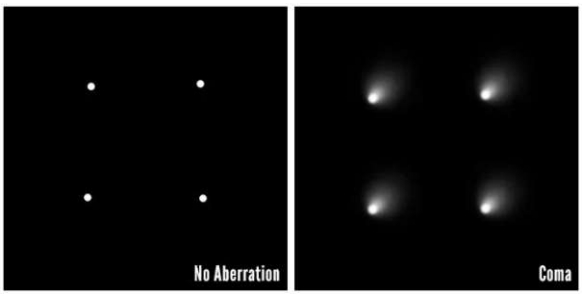

Figure 3.6: Picture visualising the effect of coma [46].

Astigmatism

Astigmatism occurs when there is a difference in focus along two perpendicular planes. This aberration causes point sources to appear elliptical or stretched, with different focus in the vertical and horizontal directions. Astigmatism can cause elongated PSFs and affects both on-axis and off-axis objects, although it typically worsens with distance from the optical centre [16]. The ligthpath is visualised in Figure 3.7 and the result can be seen in an example picture in Figure 3.8.

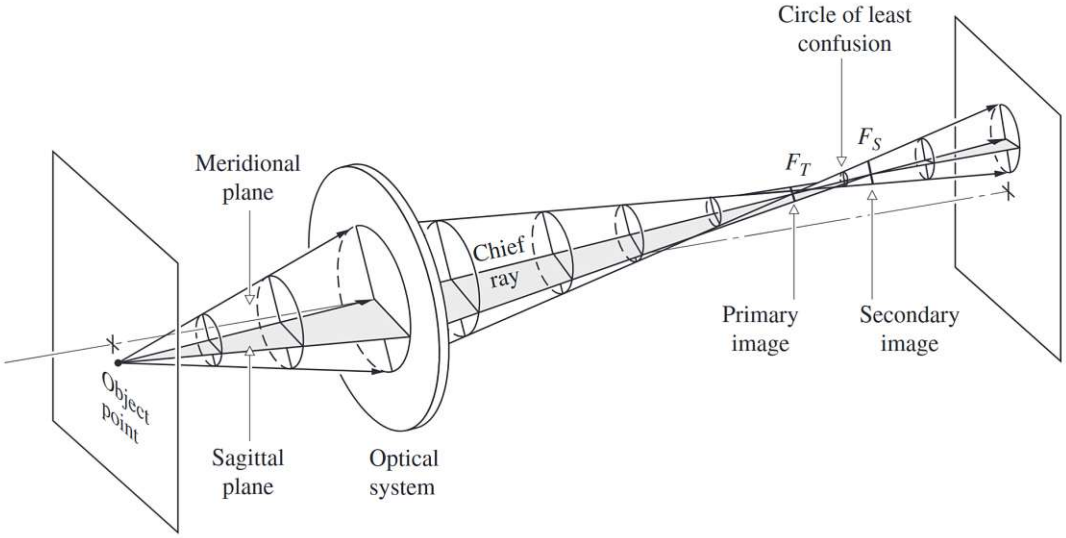

Figure 3.7: Light path in case of astigmatism [16].

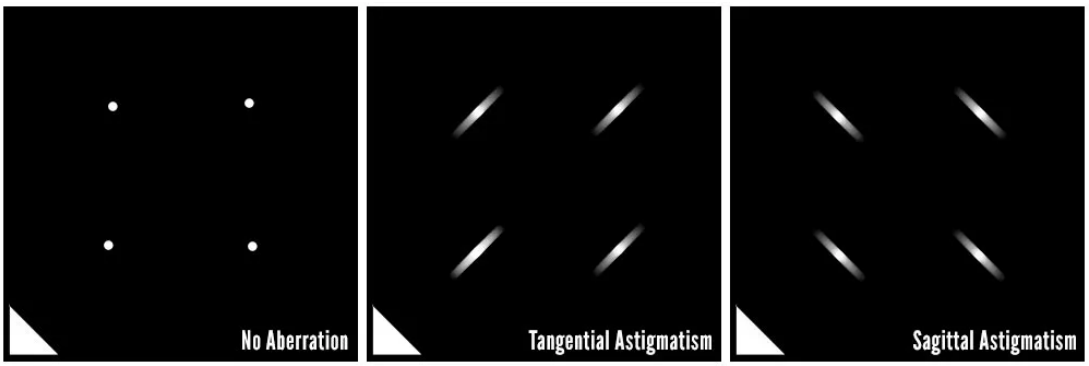

Figure 3.8: Picture visualising the effect of astigmatism [46].

Spherical aberration

Spherical aberration occurs when light rays passing through the edges of a spherical lens or mirror are focused at a different point to rays passing through the centre. This occurs because spherical surfaces do not perfectly converge light to a single focal point, resulting in a blurred or softened image. In well-designed telescopes, spherical aberration is minimised by using aspherical optics, such as parabolic or hyperbolic mirrors, to ensure that all incoming rays meet at the same focal point [16].

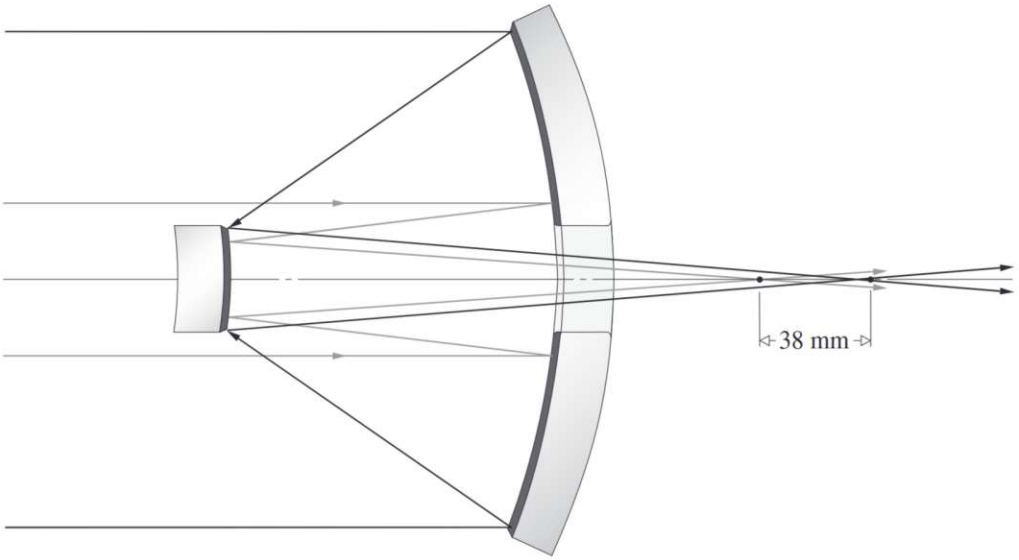

Figure 3.9: Light path of spherical aberration of the Hubble Space Telescope [16].

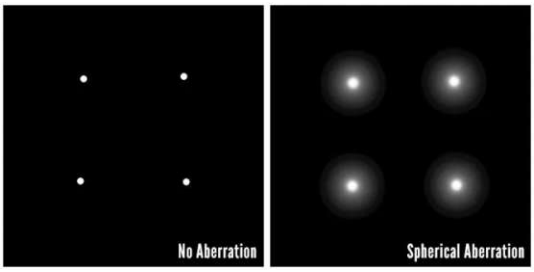

Figure 3.10: Picture visualising the effect of spherical aberration [46].

Spherical aberration played a big role in the Hubble Space Telescope (HST), where the primary mirror was polished with a slightly wrong curvature resulting in a blurry image. The mirror was too flat towards tge edges by about half a wavelength. This resulted in light rays from the edges focusing on the optical axis behind those from the central region ending up with a spherical aberration of 38 mm. A difficult and expensive repair mission, where the aberrated wavefront was corrected with an inverse error, successfully solved the issue. In Figure 3.11 the improvement after the repair can be seen.

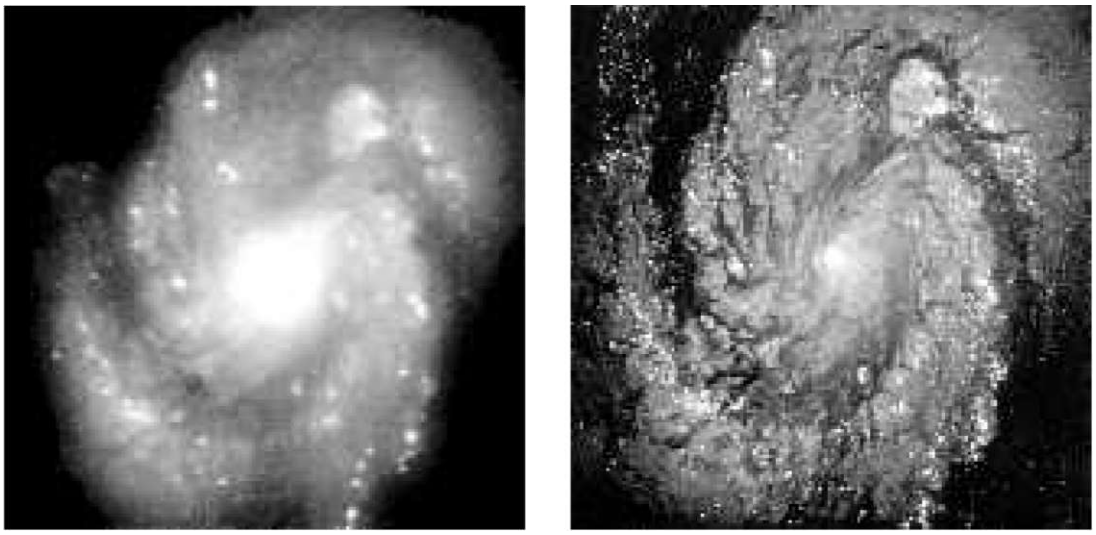

Figure 3.11: HST images before (left) and after (right) repair [16].

3.5 Wavefront sensor

The Shack-Hartmann wavefront sensor (SH-WFS) is widely used in optical systems to measure the shape and distortions of incoming wavefronts. Its basic principle involves dividing the incoming wavefront into an array of smaller segments using a lenslet array, which is a grid of small lenses placed in front of a detector. Each lenslet focuses light passing through its segment of the wavefront onto a position-sensitive detector, typically a CCD camera, creating a grid of focal spots. If the incoming wavefront is flat and free from aberrations, the focal spots form a regular grid on the detector. However, if the wavefront is distorted, the focal spots are displaced and deformed from their ideal positions and form [13, 23].

This concept is shown in Figure 3.12, which illustrates how a flat and a distorted wavefront produce different patterns on the detector: the flat wavefront results in evenly spaced, point-like spots, while the distorted wavefront produces displaced, irregularly spaced and deformed focal spots.

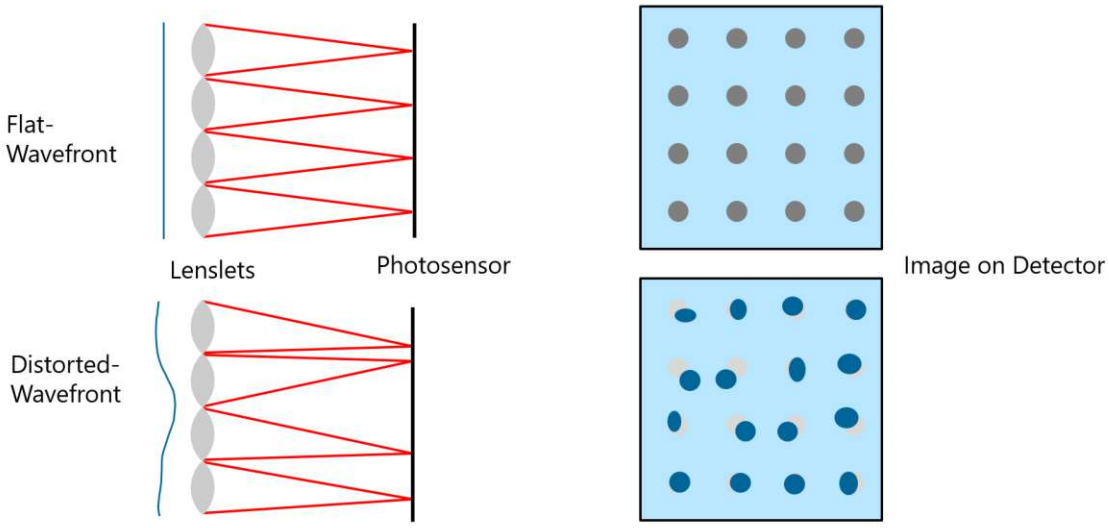

Figure 3.12: Schematic presentation of the principle of operation of a SH-WFS.

In the case of a focused beam such as in telescopes a collimating lens is placed in front of the sensor at a distance such that beam size matches the sensor size, as can be seen in Figure 3.13 [23].

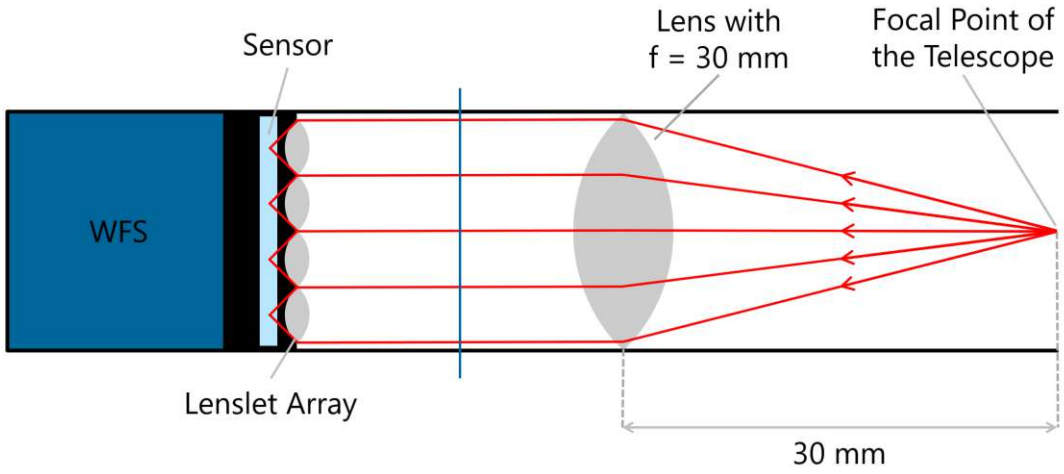

Figure 3.13: Developed WFS module compatible with a focused beam such as in a telescope.

The displacements Δx and Δy along the x- and y- axis, the focal length of a lenslet f of the WFS and the local slope of the wavefront $\frac{\partial W(x,y)}{\partial x}$ are related via Equation 6.

$$\Delta x(x,y) = f\frac{\partial W(x,y)}{\partial x}, \tag{6}$$

A similar equation exists for displacements along the y-axis. The measured displacement data can then be fit to a Zernike polynomial expansion. A least-squares estimation is used to determine the expansion coefficients.

In a more general mathematical form, the wavefront $W(x,y)$ can be expressed as a sum of Zernike polynomials:

$$W(x,y) = \sum_j W_j Z_j(x,y), \tag{7}$$

where W_j is the coefficient of the Z_j mode in the expansion, as previously stated in Section 3.2. Inserting this in the above expression gives:

$$\frac{\partial W(x,y)}{\partial x} = \sum_j W_j \frac{\partial Z_j(x,y)}{\partial x} = \frac{\Delta x(x,y)}{f} \tag{8}$$

$$= \sum_j W_j g_j(x,y) = b(x,y) \tag{9}$$

$$\frac{\partial W(x,y)}{\partial y} = \sum_j W_j \frac{\partial Z_j(x,y)}{\partial y} = \frac{\Delta y(x,y)}{f} \tag{10}$$

$$= \sum_j W_j h_j(x,y) = c(x,y) \tag{11}$$

These equations can be written in matrix form as:

$$\begin{bmatrix} b_x(x_1,y_1) \\ b_x(x_2,y_2) \\ \vdots \\ b_x(x_n,y_n) \\ c_y(x_1,y_1) \\ c_y(x_2,y_2) \\ \vdots \\ c_y(x_n,y_n) \end{bmatrix} = \begin{bmatrix} g_1(x_1,y_1) & g_2(x_1,y_1) & \dots & g_m(x_1,y_1) \\ g_1(x_2,y_2) & g_2(x_2,y_2) & \dots & g_m(x_2,y_2) \\ \vdots & \vdots & \ddots & \vdots \\ g_1(x_n,y_n) & g_2(x_n,y_n) & \dots & g_m(x_n,y_n) \\ h_1(x_1,y_1) & h_2(x_1,y_1) & \dots & h_m(x_1,y_1) \\ h_1(x_2,y_2) & h_2(x_2,y_2) & \dots & h_m(x_2,y_2) \\ \vdots & \vdots & \ddots & \vdots \\ h_1(x_n,y_n) & h_2(x_n,y_n) & \dots & h_m(x_n,y_n) \end{bmatrix} \begin{bmatrix} W_1 \\ W_2 \\ \vdots \\ W_m \end{bmatrix}, \tag{12}$$

or abbreviated as:

$$\beta = \alpha\omega, \tag{13}$$

where β represents the measured displacements, α is the matrix containing the partial derivatives of the Zernike polynomials, and ω is the vector of wavefront coefficients.

The least-squares estimate of ω can be obtained by:

$$\omega_{LS} = (\alpha^T\alpha)^{-1}\alpha^T\beta, \tag{14}$$

Since the Zernike polynomials are orthogonal their partial derivatives are orthogonal as well, which means the columns in α are also orthogonal and the matrix $\alpha^T\alpha$ becomes diagonal, simplifying the calculation of the wavefront coefficients. By projecting the data onto the partial derivatives of the Zernike polynomials and multiplying them by a diagonal matrix, the wave aberration coefficients can be obtained [40].

Through the analysis of these modes, the wavefront sensor can help identify which aberrations are present and to what extent they influence the imaging performance. The Shack-Hartmann WFS can thus serve as a feedback mechanism in active optics systems, where real-time corrections are applied to maintain or improve the telescope's imaging quality [23].

4 Implementation of the metrology system

This chapter contains a full description of the small RC-telescope, which is used to implement and evaluate the dimensional metrology system together with the WFS module. In the first part, the characteristics of the small RC-telescope are described, including a description of how the active compensation was implemented and the general setup of the experiment. In the second part, the results are presented, analysed and discussed.

The investigated telescope is a Ritchey-Chretién telescope (GSO RC 254/2000, Guang Sheng Optical, Taiwan) with a focal length of $f = 2000\,\text{mm}$. The primary mirror has a diameter of 25 cm. In Figure 4.1 a schematic depiction of the telescope can be seen. Instead of an optical tube the telescope utilises a truss structure to connect primary and secondary mirror. The mirrors are each attached to the structure by three screws, which at the same time serve as collimation adjustment screws. In a previous thesis an actuation system for the secondary mirror was developed [15]. The existing setup was further used and tested. Since the secondary mirror mounting has been modified to incorporate an active actuation system, the collimation is done slightly differently, which will be explained in more detail.

4.1 Telescope system

Light will be reflected from the primary mirror to the secondary and from there towards the wavefront sensor, which is mounted behind the primary mirror at the focuser tube which is not depicted in the figure. Additionally a baffle tube is also mounted in front of the primary to prevent stray light from reaching the sensor which would skew the experiment results. Both the baffle tube and focuser tube are mounted directly to the primary mirror cell.

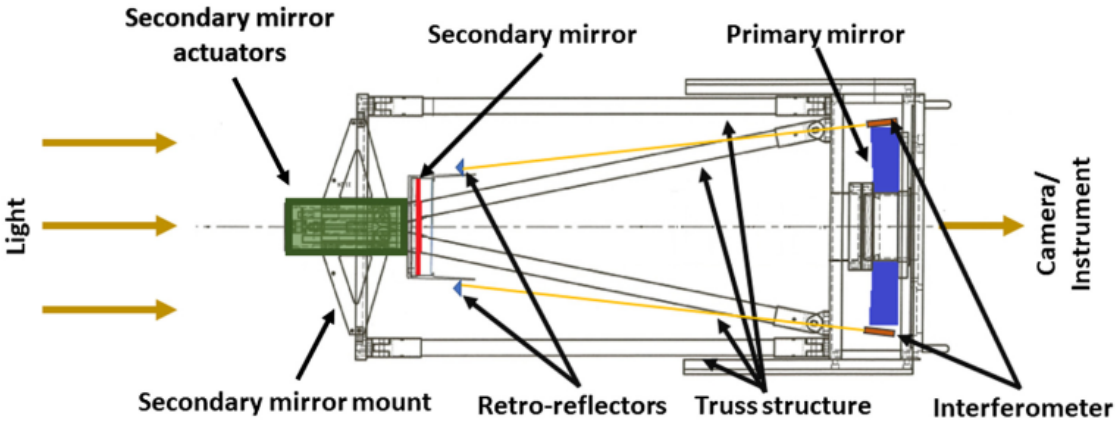

Figure 4.1: Schematics of the small RC-telescope setup [47].

The adapted secondary mirror setup to accommodate for an active system can be seen in Figure 4.2. There are three Lorentz actuators, which can pull and press against a notch flexure and therefore tip or tilt the secondary mirror (SM) relative to the primary mirror (PM) or change the distance between them. To secure the setup to the SM it is attached to a membrane flexure at the back of the SM, which still allows for enough movement in the desired range. In case the telescope wants to be operated without the active system

the membrane flexure is replaced by a solid aluminium block, which secures the SM to the telescope.

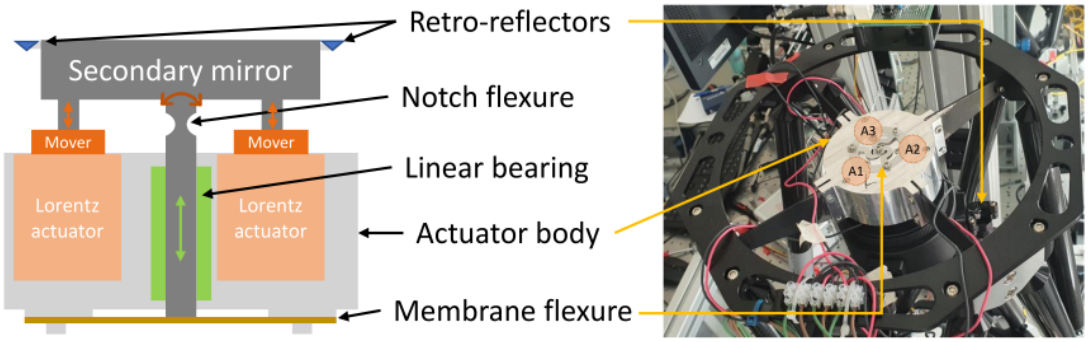

Figure 4.2: Design of the active secondary mirror system [47].

The actuation system can be seen in more detail in Figure 4.3. A thorough explanation of the design, installation and testing process of the actuation system can be found in [15] and [47].

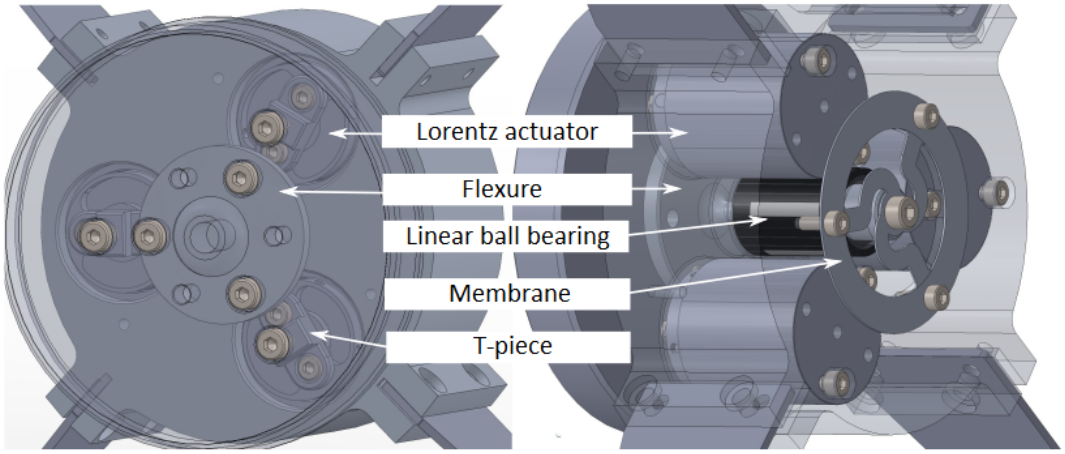

Figure 4.3: 3D model of the secondary mirror system [15].

4.2 Collimation

In a first step a well collimated telescope is required to make meaningful measurements. First a laser guided collimation approach was attempted which was not successful enough. Then a visual collimation was done following an approach often used in amateur astronomy [48, 49].

Before starting the collimation the primary mirror cell has to be reset, so that none of the screws are going to hit a limit during the collimation process and the baffle tube needs to be removed to allow for better visibility and a wider field of view. The first step is to adjust the secondary mirror. When looking through the focuser tube there are now concentric rings visible and the torus marking the center of the secondary mirror. The rings are reflections of the mirror edges and the torus marks where the optical axis is if directly looking at it. This marking can be moved by adjusting the clamps installed at the secondary mirror which replace the original adjustment screws which had to be removed

to make place for the actuation system, see Figure 4.5. By looking through the focuser tube, aligning the eye with the torus marking and illuminating the eye with for example a flashlight the marking can be centered very precisely in the illuminated reflection and the concentric rings, as shown in Figure 4.4.

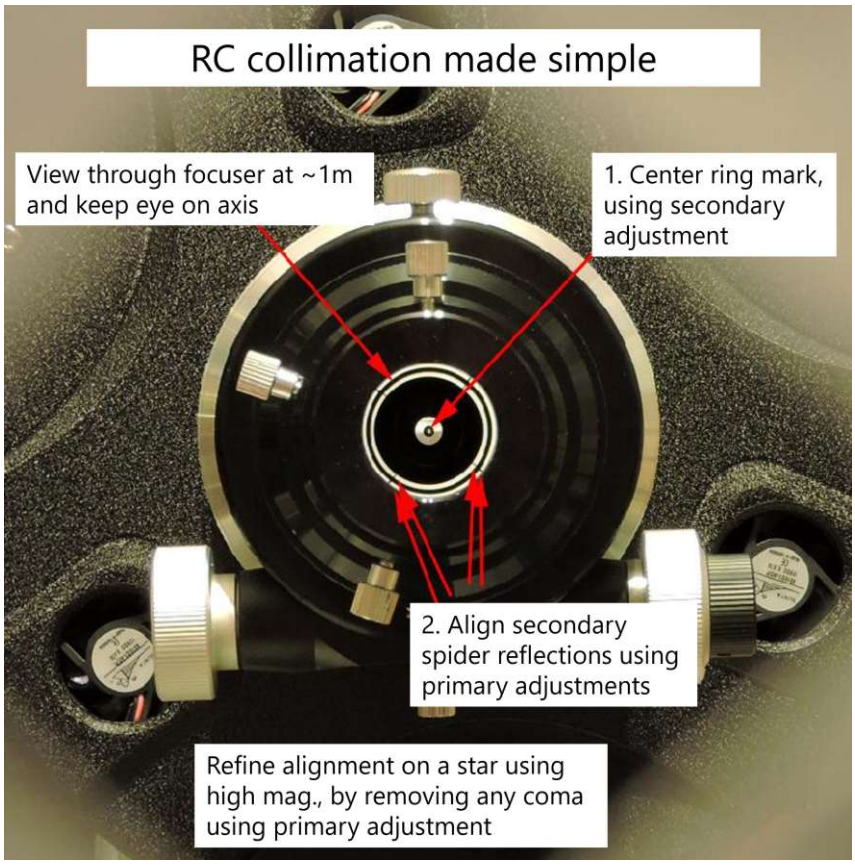

Figure 4.4: Description of a visual collimation method for a RC-telescope [48].

In the second step the primary mirror cell needs to be adjusted so that the optical axis of the primary aligns with the optical axis of the secondary. This is achieved by adjusting the primary mirror screws in such a way that the two sets of reflections of the secondary mirror spider run into each other. When assessing this alignment the observer needs to be in line with the optical axis, i.e. the eye needs to be centered over the torus of the secondary mirror.

As this adjustment will affect the previous step this process will need to be done iteratively till both the torus is centered and the spider is aligned.

Once the actuation system is in use, the collimation needs to be done slightly different and ideally be done before every use at least partially. With the flexure installed the SM sags under gravitational influence and the correct SM position needs to be set by correctly controlling the respective actuators. The required force is slightly different every use because the position of the SM in its mount changes very slightly between uses, as the telescope gets moved through the laboratory. Since only the secondary mirror position changes when switching to the active system it is enough to readjust only the secondary mirror to achieve good collimation again [48, 49].

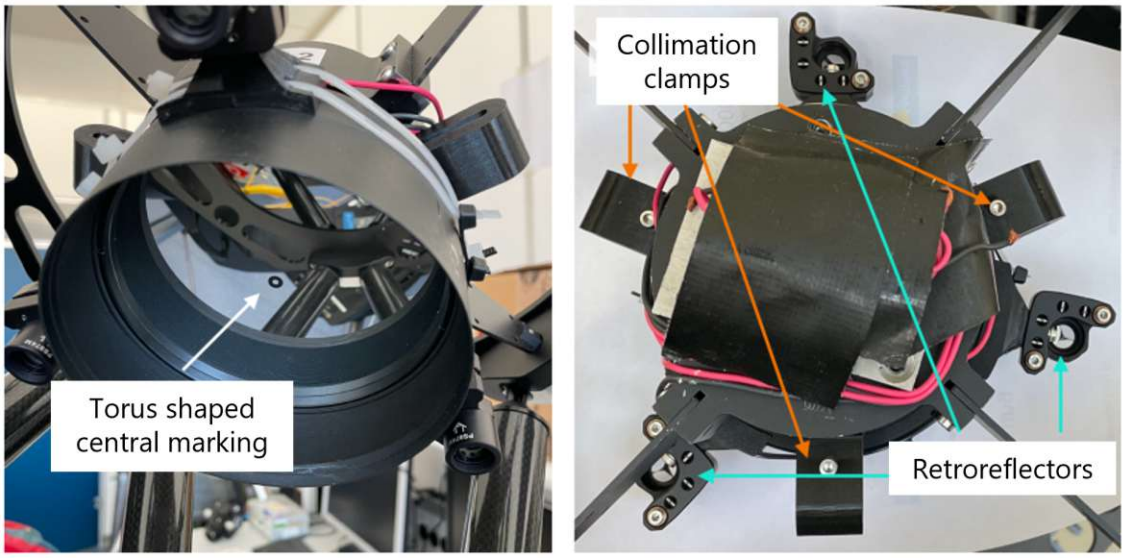

Figure 4.5: Alternative collimation screws of the secondary mirror [15].

Star test A measure to check how well the system is collimated, is to point the telescope at a star, in our case an artificial one, attach a camera to it and defocus the star till a more or less concentric pattern of light rings is visible. In case the system is perfectly aligned the shadow of the secondary mirror should be perfectly centered and the light rings concentric. This will most likely not be the case, but as the system should already be very close to a good collimation the needed adjustment of the primary screws should be less than 20°. For more help, camera softwares usually have a tool to overlay concentric rings over the image which can make the assessment more precise. This method proved much more precise than the laser-guided one and is popular among amateur astronomers and is even sometimes used in a professional environment [50]

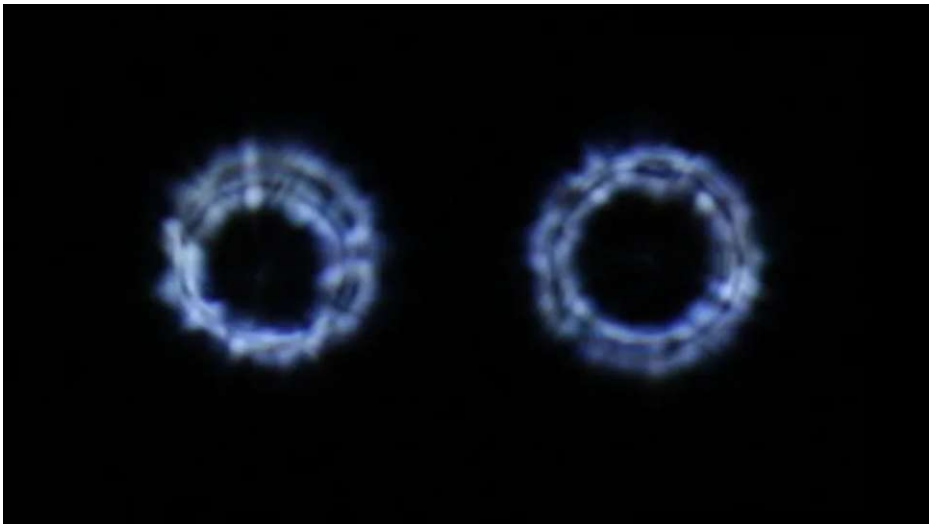

Figure 4.6: Star test, where the SM is misaligned (left) and after adjustment (right) [51].

4.3 Measurement system

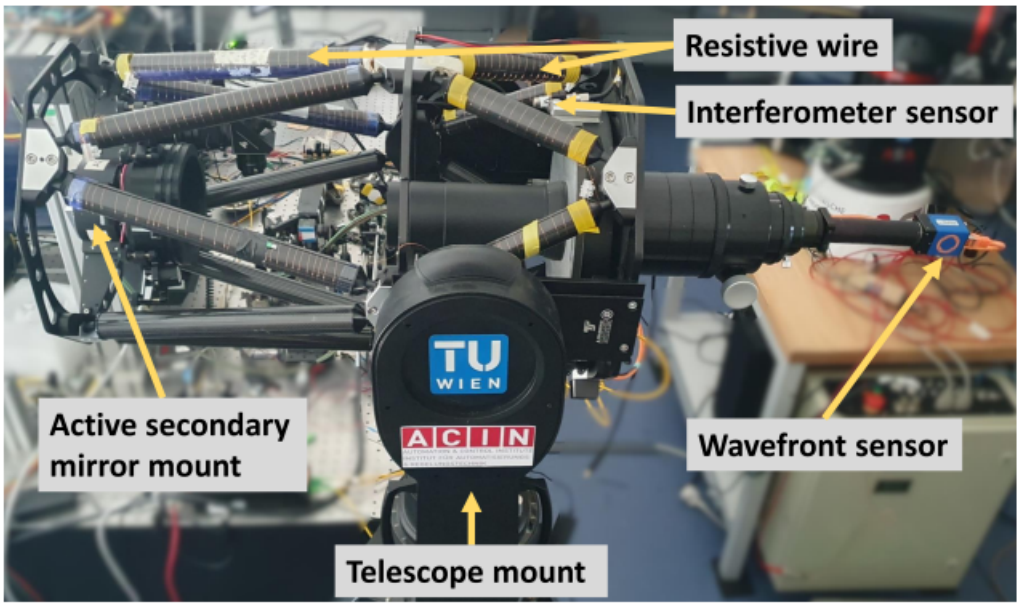

Figure 4.7: Experimental setup of the small RC-telescope.

Dimensional metrology system The dimensional metrology system is responsible for measuring the relative distances between the primary and secondary mirror and constantly updating this distance as it changes or in case of the compensation system kept as constant as possible. For this system an absolute displacement measuring interferometer (IF), which utilises a Fabry-Pérot design, was chosen. The measurement is non-contact as a laser beam is emitted from a sensor head and reflected by an object. The interference generated at the sensor head is used to determine the distance travelled by the laser beam. Connected are three identical sensor heads (IDS3010 with three M12/C7.6, Attocube Systems AG, Haar, Germany). Three retroreflectors (RR) are mounted on the secondary mirror in a 120° pattern directly opposite of the sensor heads which are mounted directly to the primary mirror circumference. This setup does not require any light from the telescope.

The most important properties are summarised in Table 4.1. In particular, the combination of a high working distance with a high resolution is ideal for measuring the distance between the primary and secondary mirrors. This is specified by the manufacturer as 441.6 mm, whereby the individual length changes of each axis is in the micrometer range. This means that the requirements placed on the distance sensor are met with the properties in Table 4.1.

Table 4.1: Properties of IDS3010 interferometer.

Parameter	Value
Working distance	5 mm – 30 m
Resolution	5 pm
Bandwidth	10 MHz

The measured distance is approximately 445 mm. A high speed serial link (HSSL) is used to transmit the signals of the sensors to a Matlab program, which records the signals and converts them to the corresponding tip and tilt angles as well as the total distance change of the secondary mirror along the optical axis. In the case of active compensation, the measurement of the three axis is used to keep the respective distances as constant as possible.

Wavefront sensor As a wavefront sensor the Shack-Hartmann WFS (SHSCam AR2-110-GE, Optocraft GmbH, Erlangen, Germany) was chosen. It has an array of 43×32 lenslets and a detection area of $(4.8 \times 3.6)\text{mm}^2$. The wavefront sensor is attached to the telescope to assess both the effects of disturbances and the effect of the compensation system on the wavefront error. Operating at a sampling rate of up to 30 Hz, the sensor reconstructs the wavefront, which is then expressed using Zernike polynomials. To minimize atmospheric effects, the resulting data is smoothed using a moving mean filter with a block size of 18000 samples ($\sim$ 12.5 min). A collimation lens with a 30 mm focal length is positioned in front of the wavefront sensor to align the sensor with the telescope's pupil plane. The wavefront sensor data is transmitted via an Ethernet connection, while the operation, control, and data acquisition for both the compensation system and the sensor are managed using MATLAB software (MathWorks, Natick, USA). Figure 4.8 shows the WFS and the tube containing the collimation lens as well as the adapters used to attach to the telescope. In Figure 4.9 a model of the optical system shows the telescope, the collimation lens and the WFS plane, as well as the light path.

Figure 4.8: SHWFS and adapter tube with collimating lens.

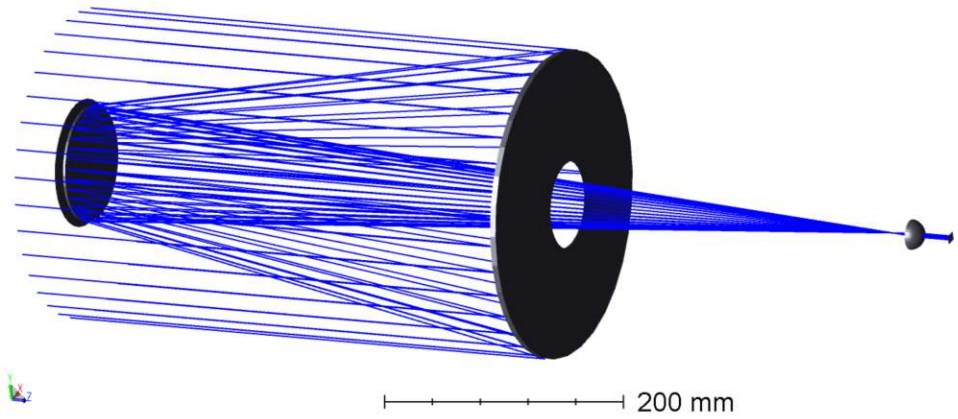

Figure 4.9: Ray tracing of the complete optical setup [52].

4.4 Experiment setup

The discussed 25 cm RC-telescope was adapted with the mentioned actuation system replacing the original passive secondary mirror mount, while keeping the telescope spider assembly and the secondary mirror's position as in the initial setup. The telescope is placed on a motorized fork mount configured in an alt-azimuth configuration and placed on a tripod in a laboratory. The laboratory provides a direct line of sight to a second building of TU Wien, located almost 300 m away. An artificial star, created using a high-power LED and a pinhole, is mounted on the roof of this building to serve as a reference point for measurements. The top half of the the telescope truss structure is wrapped in a resistive wire, which in some measurements is used to heat up the system by electric current. This temperature change is measured by a temperature sensor of the type NTC030WH01 (Carel Industries S.p.A, Brugine, Padova, Italy). Real-time hardware, specifically a MicroLabBox (dSpace GmbH, Paderborn, Germany), is used for signal acquisition, PWM signal output for actuator control, and feedback control, operating at a sampling frequency of 10 kHz. Three independent proportional-integral (PI) controllers are configured to achieve a closed-loop bandwidth of 2 Hz [47].

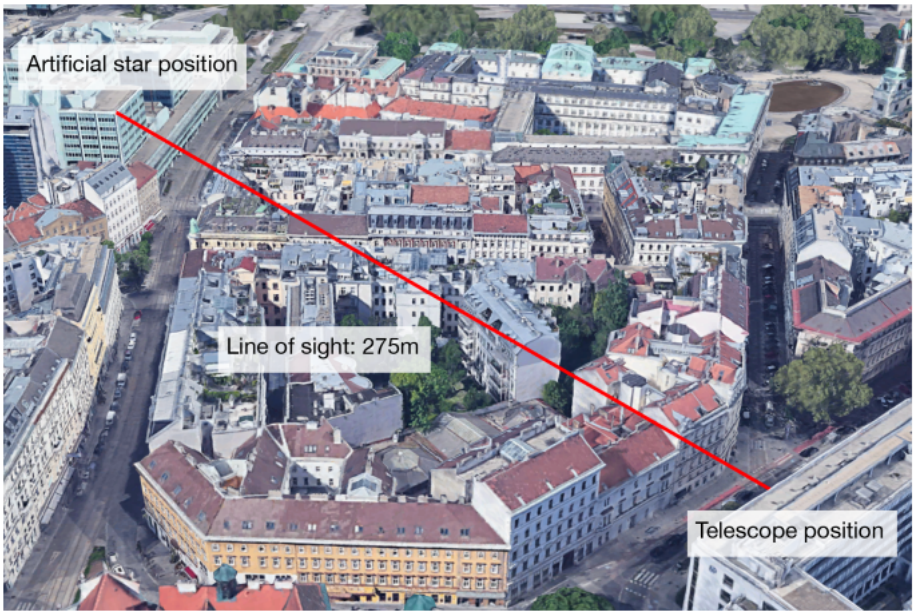

Figure 4.10: Overview from the laboratory to the artificial star [53].

4.5 Results of the small RC-telescope

Asymmetric heating of a telescope has a huge effect on the image quality that the telescope can produce. To study this effect, a resistive wire was wrapped around the upper half of the telescope's truss structure, simulating sunlight. As a first measurement, the distance changes due to the expansion of the material with increasing temperature were measured with the metrology system and the optical aberrations were simultaneously measured with a wavefront sensor. The measurements were made for 15 min and a temperature difference of over 20 °C could be achieved. The system was observed while it heated up and while it cooled down, and also while it was left completely alone to get a reference of the static system. Measurements were taken both with and without the active compensation system and a comparison is presented. All measurements were taken several times to verify the behaviour, and a moving mean filter with a block size of 18000 samples is applied to smooth out atmospheric turbulences. The temperature dependence of the measured quantities is clearly visible, with a strong effect on tip and tilt and axial displacement.

4.5.1 Comparison of undisturbed system with and without compensation

In Figure 4.11 a comparison of the dimensional measurements with and without actively compensating for any distance changes while no disturbances were introduced is shown. It is clear that the compensation system is working correctly and there is a very small drift in axial displacement while not actively compensating for that, but when compared to for example Figure 4.13 where a disturbance in the form of heat is introduced, this displacement is a lot smaller.

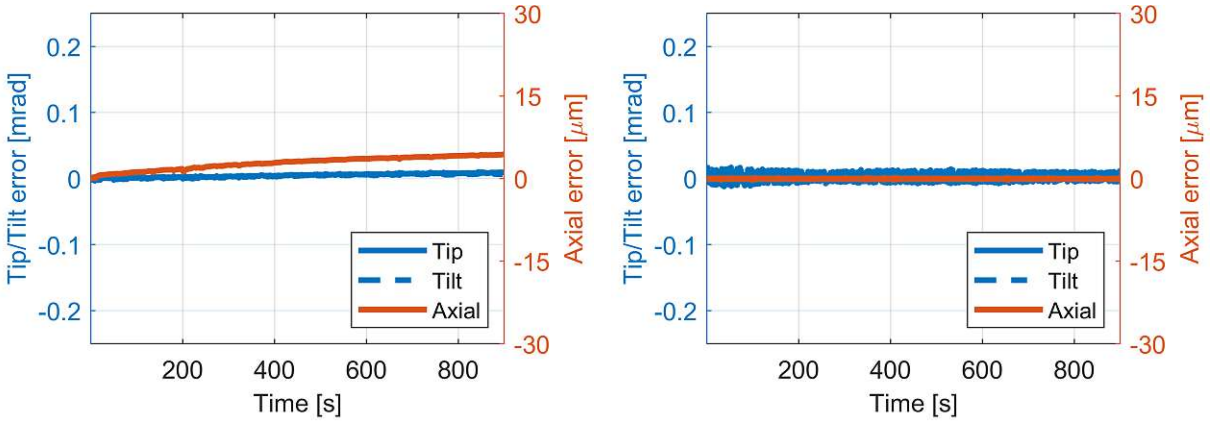

(a) Uncompensated system.

(b) Compensated system.

Figure 4.11: Dimensional measurement of the undisturbed system.

In Figure 4.12 a comparison of the first eight Zernike polynomials measured by the wavefront sensor over 15 min while no disturbances were introduced is shown. The errors measured by the WFS in Figure 4.12a align with the ones measured by the dimensional measurement system in Figure 4.11a. Defocus is, while still small, the most dominant error with tip and tilt being a bit smaller. As the dimensional measurement system and the wavefront sensor do not share the same coordinate system the sign and for some aberrations the magnitude can be different. The visible WFE increase in Figure 4.12b, although no change in distance can be seen in Figure 4.11b, is due to the fact that the WFS takes into account more aberrations than the metrology system and also ones that are not directly compensated for by the active optics system.

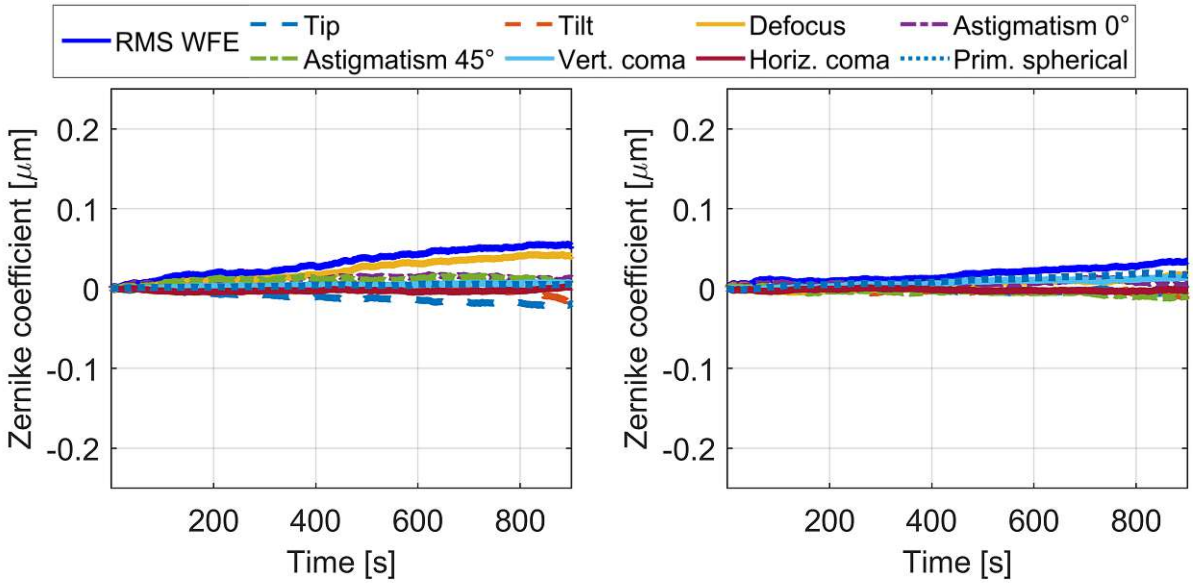

(a) Zernike polynomials of the uncompensated system.

(b) Zernike polynomials of the compensated system.

Figure 4.12: Zernike polynomial measurement and RMS WFE of the undisturbed system.

4.5.2 Comparison of disturbed system (heating) with and without compensation)

In Figure 4.13 a comparison of two dimensional measurements is shown. The system was heated up asymmetrically over 15 minutes in both cases. This led to a noticeable change in axial displacement and tilt, which directly correlates to the asymmetric temperature change, as shown in Figure 4.13a. A maximum axial distance change of 25.89 µm was recorded and tip/tilt changed for a combined maximum value of 0.24 mrad. The second measurement was performed in the same way, but the resulting distance changes were actively compensated for, which can be seen in Figure 4.13b. Here a maximum axial distance change of 0.32 µm and a combined maximum tip/tilt value of 0.02 mrad were recorded.

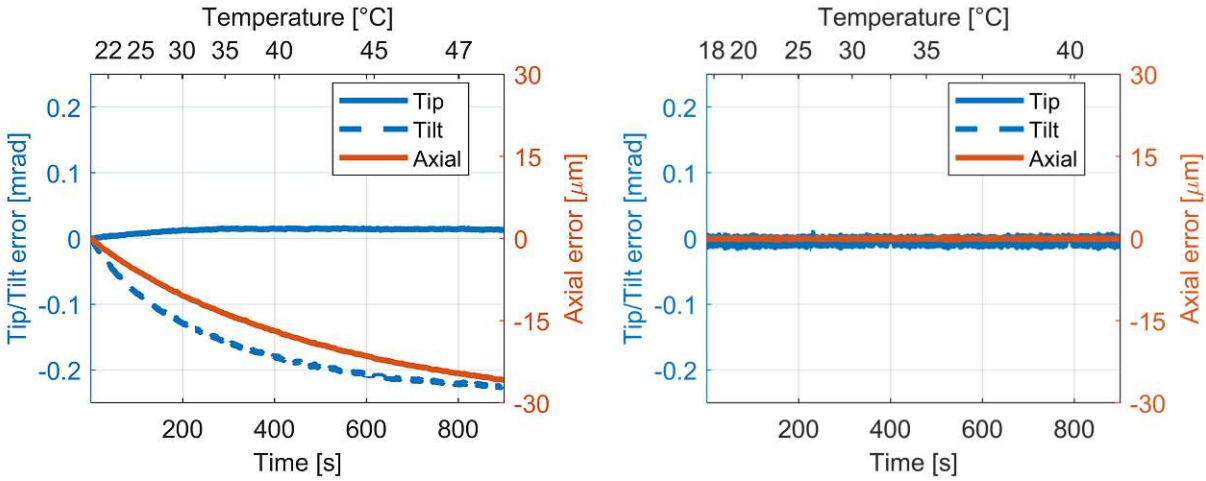

(a) Uncompensated system.

(b) Compensated system.

Figure 4.13: Dimensional measurement of the system while heating.

The comparison of Figure 4.14 shows that the compensation system manages to reduce several different errors. Especially defocus and tilt in x and y direction are reduced significantly, which are also the errors the compensation system aimed to directly manage. The maximum defocus value was reduced from -102 nm to 8 nm and the combined tip/tilt value was reduced from 181 nm to 19 nm, which gives an improvement of 12.7 and 9.6.

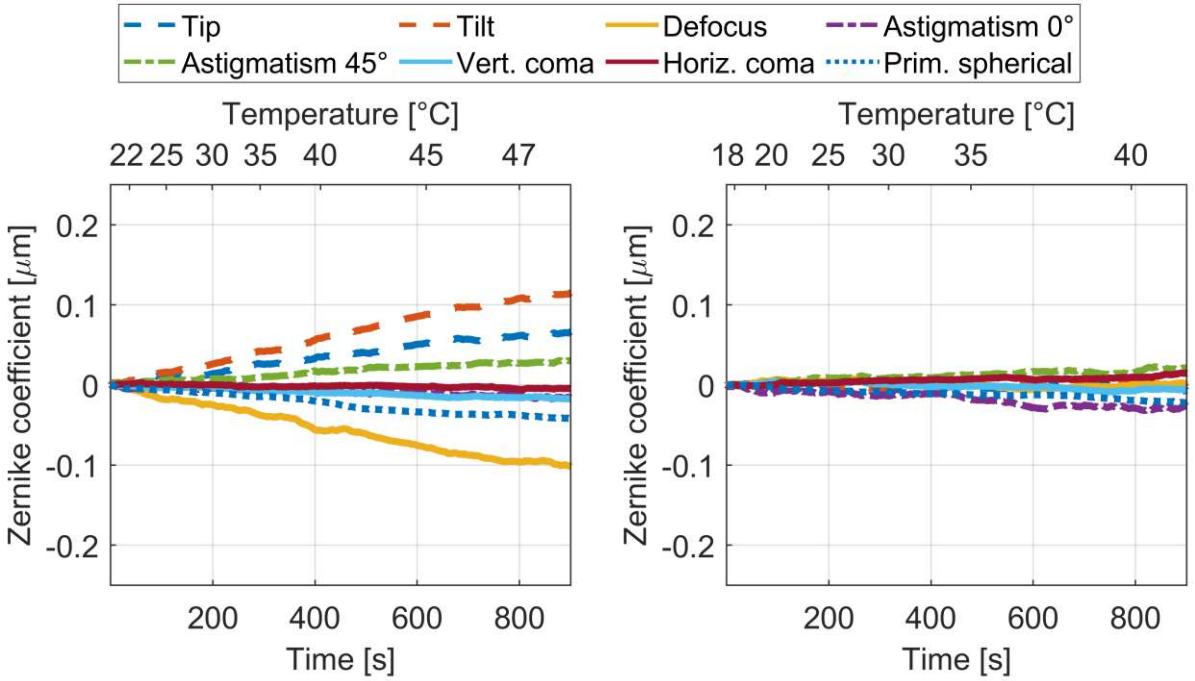

(a) Zernike polynomials of the uncompensated system.

(b) Zernike polynomials of the compensated system.

Figure 4.14: Zernike polynomial measurement during the heating phase.

For a clearer comparison the calculated RMS wavefront error is plotted separately in Figure 4.15. While not actively compensating any distance changes the RMS wavefront error reaches a maximum value of 185 nm as seen in Figure 4.15a and while actively keeping a constant distance a maximum value of 46 nm, resulting in an improvement by a factor of 4.0. The RMS WFE correspond to a Strehl ratio of 3.5% and 81.1% respectively. The Strehl ratio was calculated via Equation 5, which is only valid for relatively small aberrations which is not the case for the uncompensated system but for the sake of comparison it was used nonetheless.

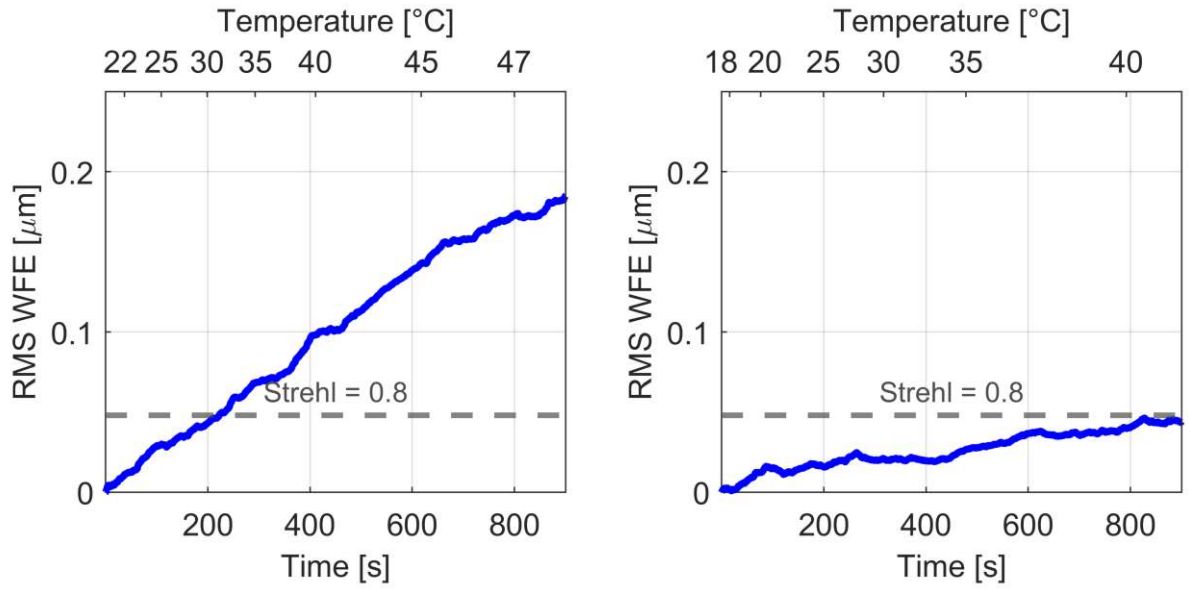

(a) Uncompensated system.

(b) Compensated system.

Figure 4.15: Measured RMS WFE of the heating phase. The RMS error for a diffraction limited Strehl ratio of 80% is indicated by a grey dashed line.

As the compensation system mainly regulates defocus and tip/tilt it is also interesting to analyse what improvement can be achieved when only viewing those specific errors. Here it is much more clearly visible that defocus, tip and tilt are very well compensated. Using only those three values one gets an RMS WFE of 167 nm and 13 nm, which results in a Strehl ratio of 6.5% and 98.3%. The RMS WFE improved by a factor of 12.8.

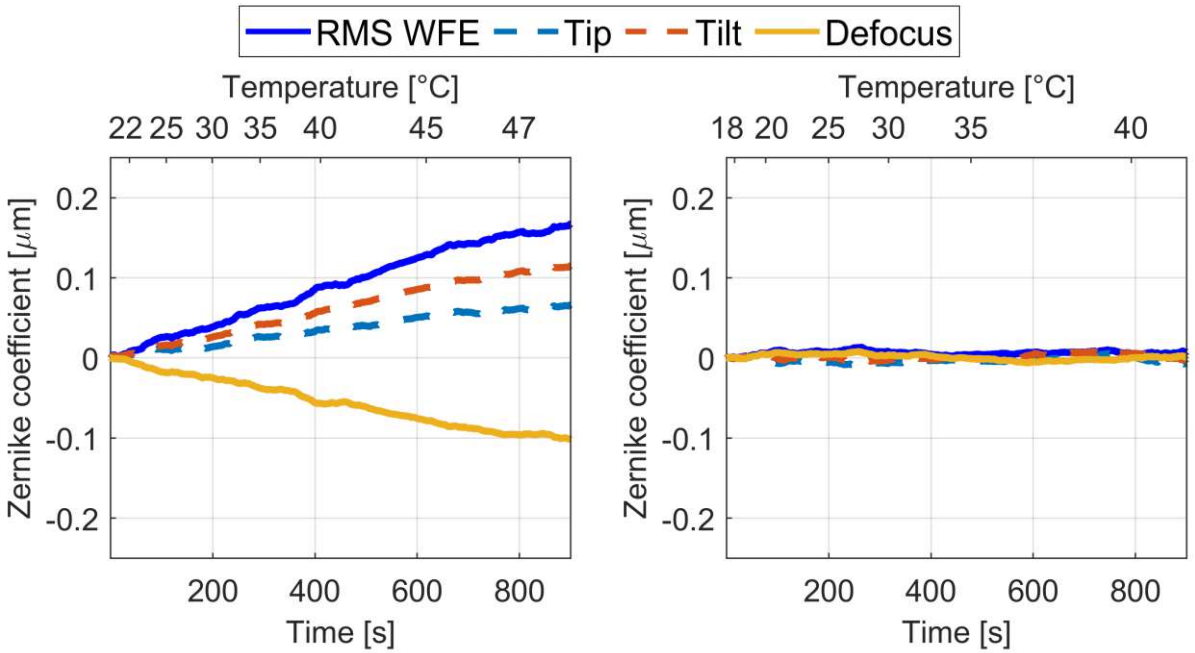

(a) Uncompensated system.

(b) Compensated system.

Figure 4.16: Major Zernike polynomials and resulting RMS WFE while heating.

For a complete analysis the aberrations not directly targeted by the compensation

system are also plotted separately in Figure 4.17. It is visible that the errors are a lot smaller than in Figure 4.16 and that the errors in the compensated and uncompensated case only deviate minimally from each other.

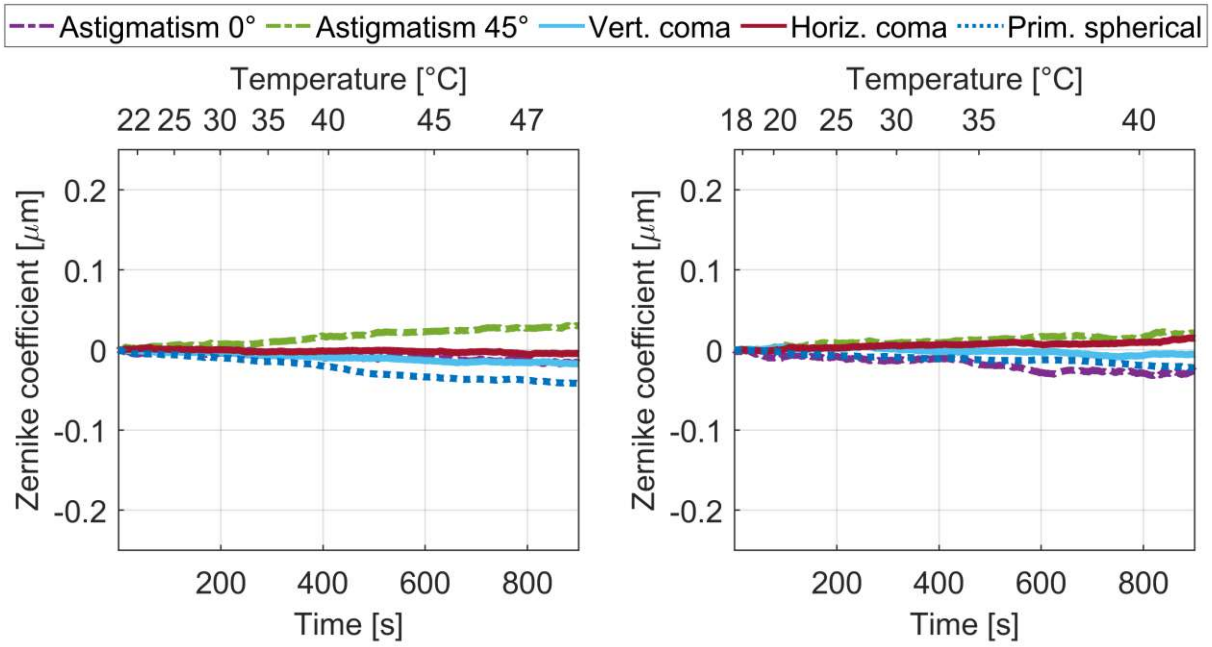

(a) Uncompensated system.

(b) Compensated system.

Figure 4.17: Zernike polynomials not targeted by compensation system while heating.

4.5.3 Comparison of disturbed system (cooldown) with and without compensation)

In Figure 4.18 again two dimensional measurements can be seen. The measurement was performed immediately after a heating phase like in Section 4.5.2. Again the distance changes were recorded over 15 min while the system cooled down, once without compensating for any distance changes and another time while the distance was kept constant. When comparing Figure 4.13a and 4.18a it shows that the displacement along the optical axis as well as tip and tilt are of the same magnitude but in different directions, which is to be expected. A maximum axial distance change of 26.53 µm was recorded and tip/tilt changed for a combined maximum value of 0.23 mrad. Figure 4.18b shows that the compensation system works well also when the temperature of the system cools back down.

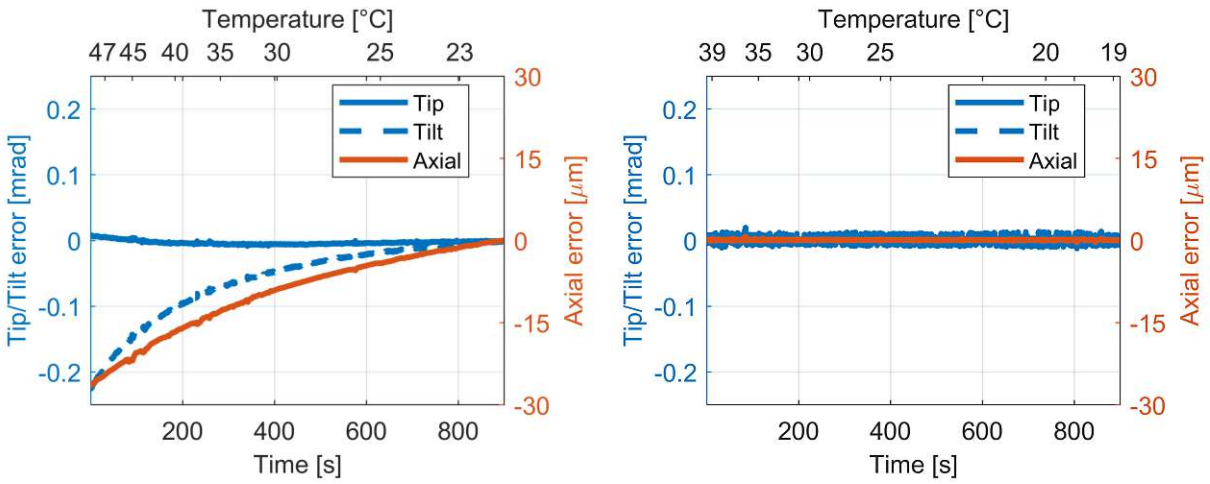

(a) Uncompensated system.

(b) Compensated system.

Figure 4.18: Dimensional measurement during the cooldown phase.

The measurement of the Zernike polynomials done by the WFS confirms that the compensation system can indeed reduce the various errors also while the system cools down, as seen in Figure 4.19. The dominant errors are defocus, tip and tilt with astigmatism also being significantly larger than during the heating phase (Fig. 4.14a). The maximum defocus value was reduced from −128 nm to −10 nm and the combined tip/tilt value was reduced from 205 nm to 32 nm respectively, which gives an improvement factor of 12.4 and 6.4.

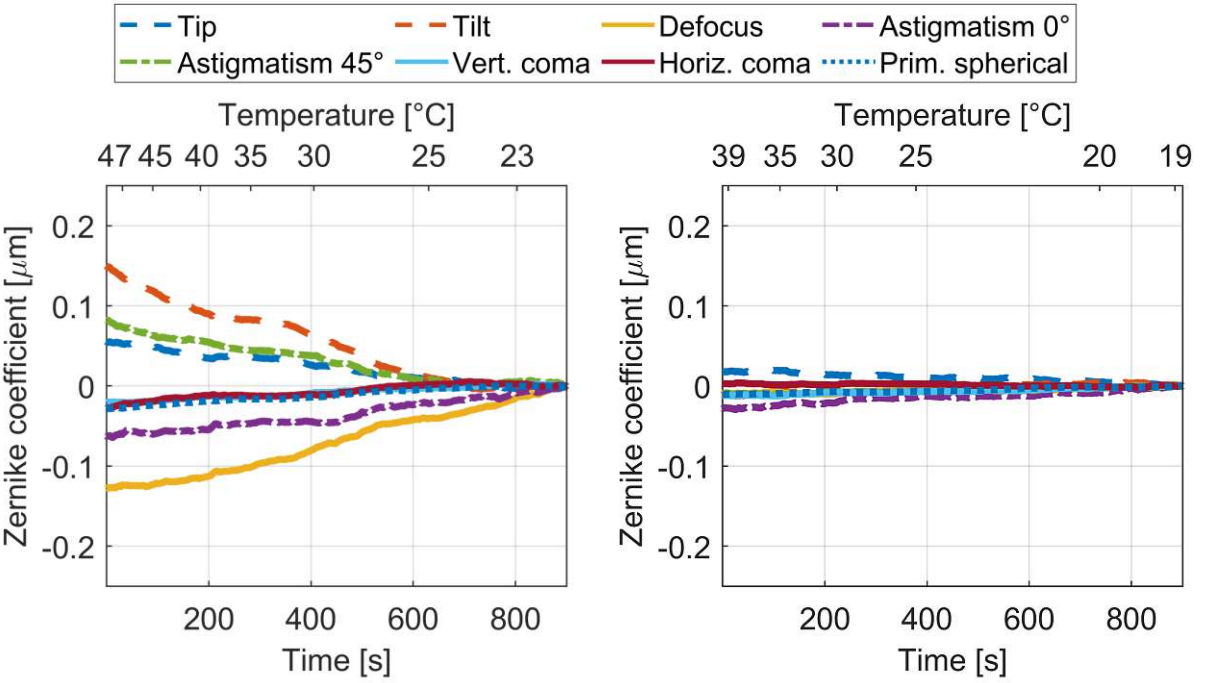

(a) Zernike polynomials of the uncompensated system.

(b) Zernike polynomials of the compensated system.

Figure 4.19: Zernike polynomial measurement during the cooldown phase.

The RMS wavefront error is again plotted separately for more clarity. The maximum

value of the RMS wavefront error during the measurement where no compensation system was being used was 243 nm and when repeating the same measurement while actively maintaining the distance between primary and secondary mirror the maximum value was 43 nm, resulting in an improvement factor of 5.65. The RMS wavefront errors correspond to a Strehl ratio of 0.3% and 83.7% respectively.

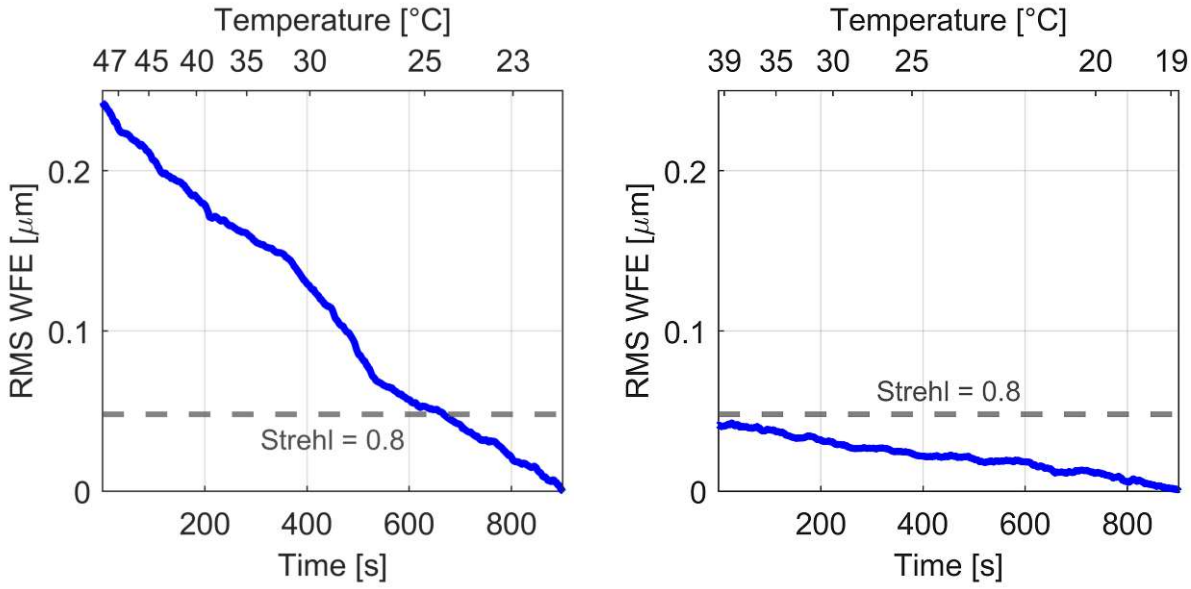

(a) Uncompensated system.

(b) Compensated system.

Figure 4.20: Measured RMS WFE during a cooldown phase. The RMS error for a diffraction limited Strehl ratio of 80% is indicated by a grey dashed line.

As stated in the previous section the compensation system mainly regulates defocus and tip/tilt, which makes it interesting to also analyse these errors specifically and what improvement can be achieved when only viewing those specific errors. Using only those three values this gives a maximum RMS WFE of 204 nm and 23 nm, which results in an improvement by a factor of 8.9. The corresponding Strehl ratios are 1.7% and 94.6% respectively.

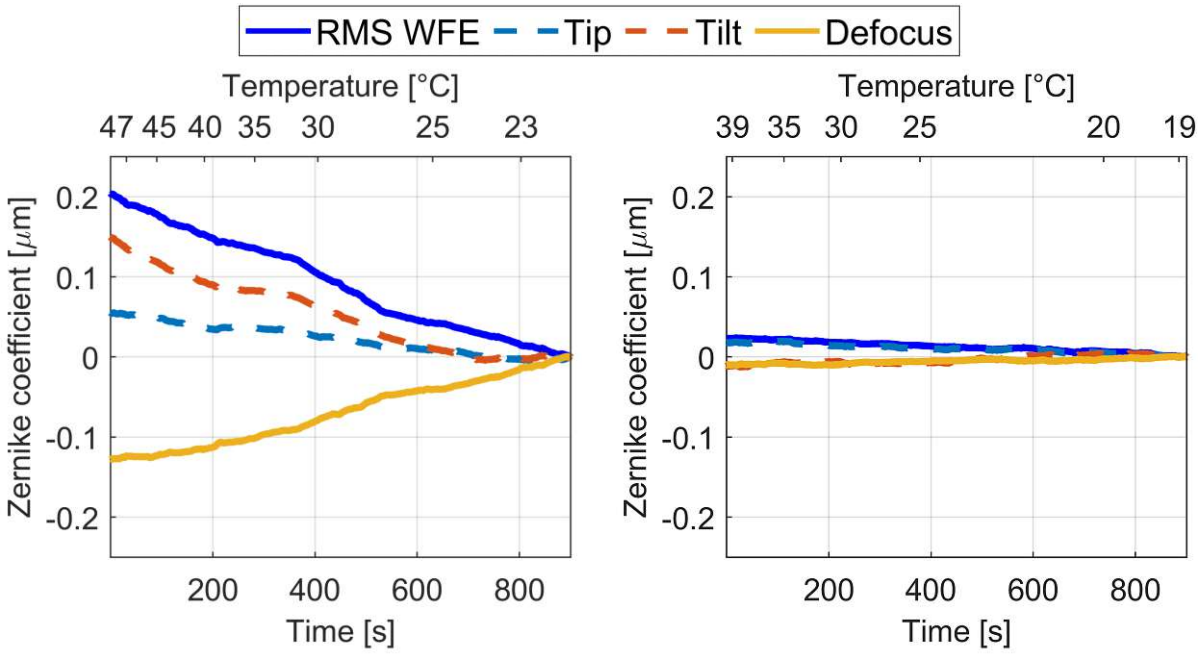

(a) Uncompensated system. (b) Compensated system.

Figure 4.21: Major Zernike polynomials and resulting RMS WFE while cooling down.

For a complete analysis the Zernike polynomials not directly targeted by the compensation system are again plotted separately in Figure 4.22. Unlike in the heating process, this time there is a clear distinction between the uncompensated and compensated case, with astigmatism being much more prominent in the uncompensated case.

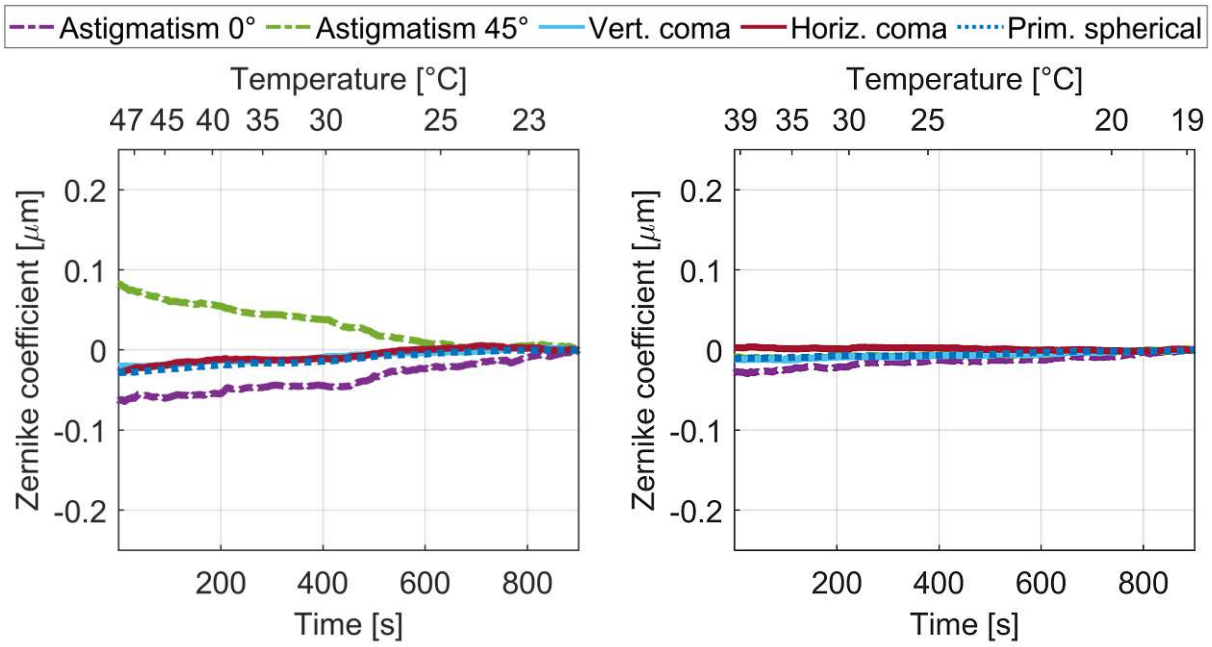

(a) Uncompensated system. (b) Compensated system.

Figure 4.22: Zernike polynomials not targeted by compensation system while cooling down.

4.5.4 Comparison heating and cooldown phases

Uncompensated: In the following plots two back to back measurements consisting of one heating phase and the following cooldown phase are combined into one plot. Figure 4.23 shows the data of the metrology system. There is a slight discontinuity at 900 s since there is a short pause between the two measurements to turn off the heating, save the data and start the next measurement. This is indicated in all following figures by the straight grey line. It is visible that after the telescope has cooled back down to the ambient temperature almost the same alignment and axial distance are restored.

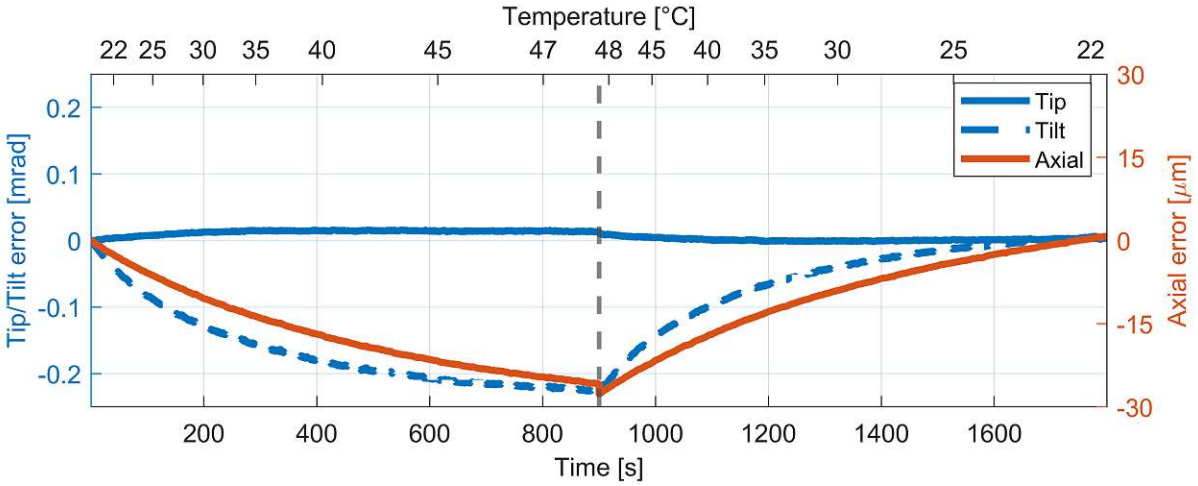

Figure 4.23: Metrology data of an uncompensated combined heating and cooldown phase.

The same is done in Figure 4.24 for the wavefront sensor data. There is a clear discontinuity where the measurement was interrupted and an expected inverse behaviour after the temperature sinks again. All the errors move towards a constant value, which is slightly different than the original one, with defocus, tilt and astigmatism being the errors where this behaviour is most pronounced. A possible explanation for this is that, as so many measurements were taken in succession that the temperature sensor may show the same starting and end temperature but the system itself may not have been in thermal equilibrium at the start of the measurement.

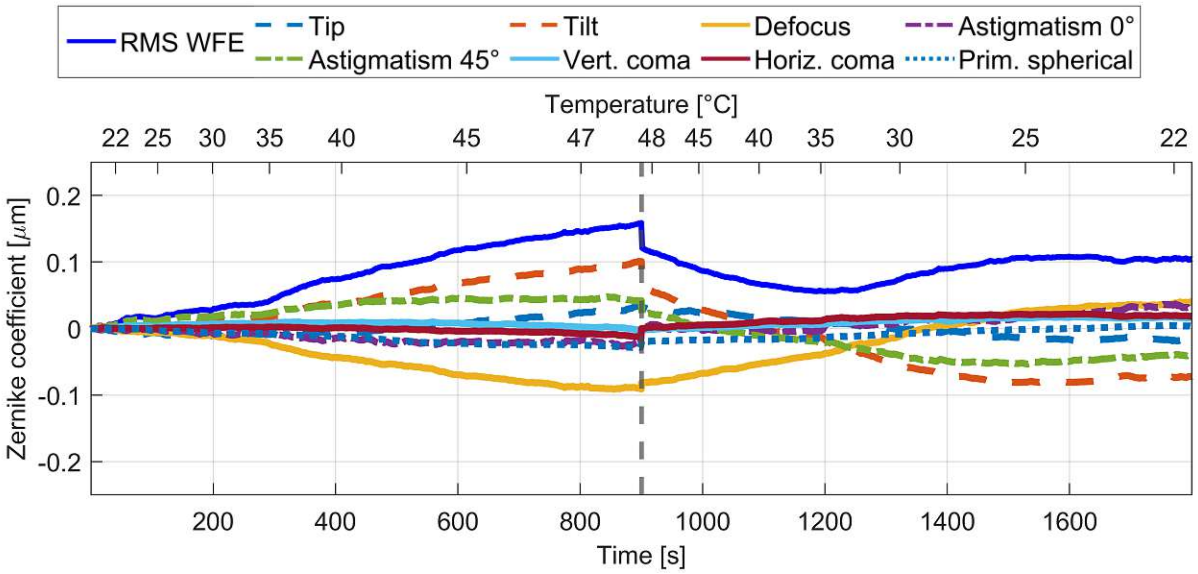

Figure 4.24: WFS data of an uncompensated combined heating and cooldown phase.

Compensated: In the next short section the plots of two compensated back to back measurements with one heating and the following cooldown phase being combined into one are presented. This time even though there again is a pause between the two measurements no discontinuity can be seen in Figure 4.25, since the compensation system was active the whole time. The straight grey line indicates where the measurement was paused.

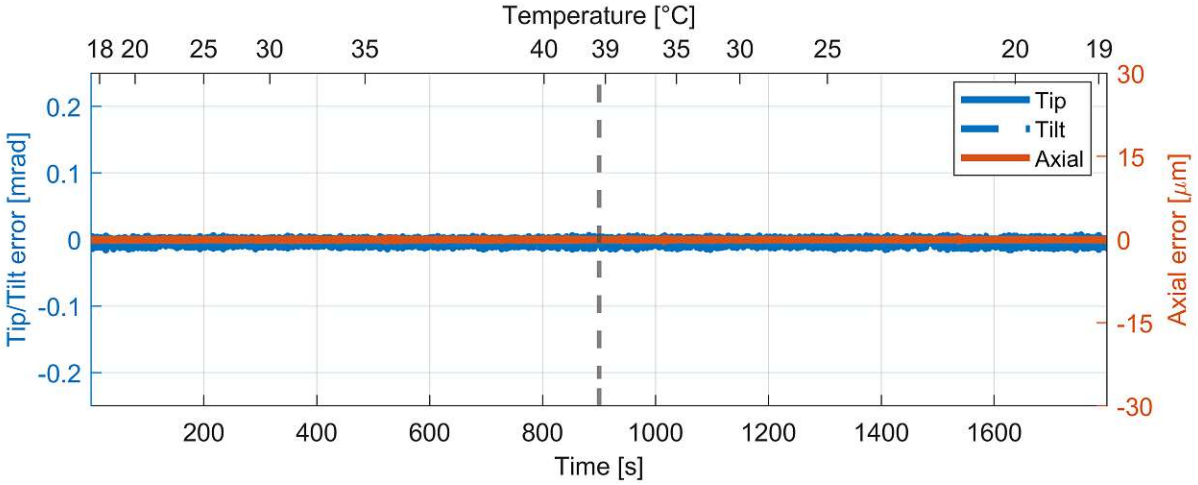

Figure 4.25: Metrology data of a compensated combined heating and cooldown phase.

The combined WFS measurement again shows a discontinuity at 900 s when the measurement was interrupted, although it is smaller than the one in the uncompensated case. All the aberrations keep a very low value with no special outliers.

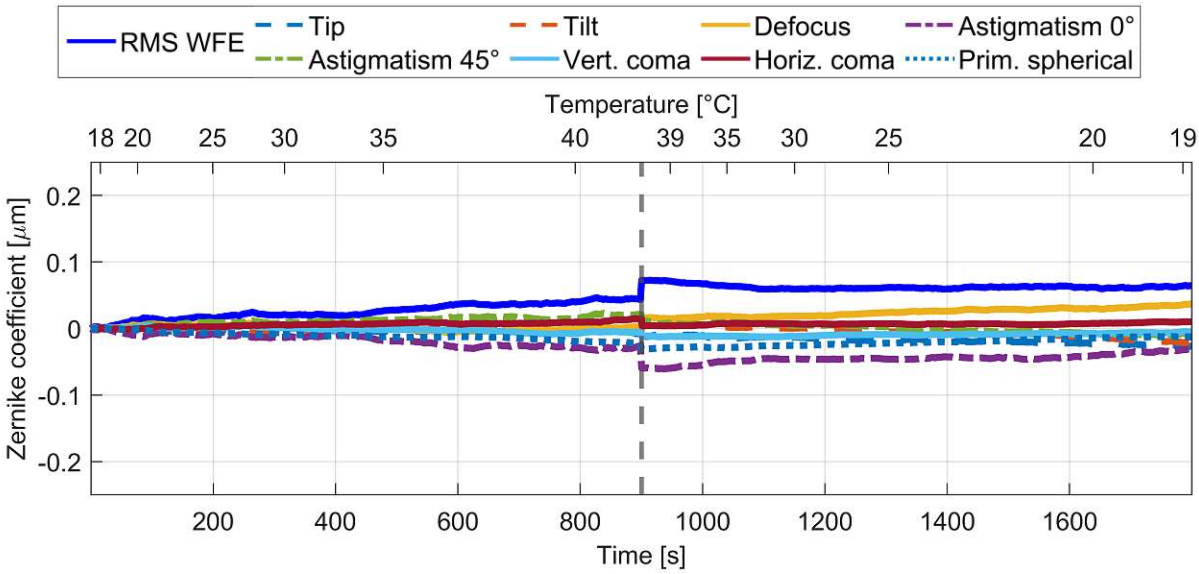

Figure 4.26: WFS data of a compensated combined heating and cooldown phase.

It would be interesting to see a continued measurement over a heating and cooldown cycle to further study the compensation system. The discontinuity in the uncompensated case stems from the interruption of the measurement while the errors were still propagating in the meantime. In the compensated case it is most likely mainly caused by the static error propagation as seen in Figure 4.11b. Since there was also an error increase in the static measurement, it could be an option to subtract the static data from the heating/cooldown data to see how well the compensation handles the extra disturbances introduced by a temperature difference and if can affect the other aberrations besides defocus and tip/tilt at all. The very successful effect on defocus and tip/tilt could already be seen in Figures 4.16 and 4.21.

4.6 Discussion

The active secondary mirror system demonstrated that it was easily capable of regulating distance changes of over 25 µm effectively, as shown for example in Figure 4.13 and 4.18. By doing so a Strehl ratio of over 80% could be maintained in all cases. When focusing solely on the aberrations that the compensation system is actively targeting (defocus, tip/tilt), the Strehl ratio could consistently be kept above 94%.

During the combined heating and cooldown WFS measurements, the aberrations returned to a slightly different constant value compared to the initial state, as shown in Figure 4.24 and 4.26. However, the metrology system returned to or was kept at its starting point (Figure 4.23 and 4.25), indicating that the system's behaviour is more complex than what can be regulated through the information fed to the compensation system. It would be interesting to investigate whether this discrepancy between the dimensional metrology and the WFS measurement is due to interruptions during the measurement process or movement around the laboratory or due to a more complex mechanism.

5 Leopold Figl-Observatory

This chapter contains a complete description of the Leopold Figl-Observatory (LFO). In the first part, a sensitivity analysis is presented to first get an idea of how much the image quality is affected by different distance changes and also to choose appropriate measurement devices. This is followed by a description of how the measurement system was installed on the telescope. This includes a description of all the adapters that had to be designed and manufactured to successfully install the measurement system on the telescope. Following this is a section on how the measurements were performed and analysed. Since the WFS measurement could not be performed at the LFO despite several attempts, due to a combination of unavailable remote access and bad weather conditions, the setup was used on another telescope with a real star to prove that it works. Finally, all results are presented and discussed.

5.1 Sensitivity analysis

Before starting any measurements it is important to get an idea in what order of magnitude the measured distances are going to change, so that a suitable measuring device can be selected. The telescope was modelled in Zemax, a common software for modelling and simulating optical systems. Then for various distance changes a RMS WFE was calculated and a corresponding Strehl ratio was calculated via Equation 5. These data points were plotted and a linear fit was added between the points, as visible in Figure 5.1. It is evident that the lateral displacement affects the Strehl ratio much less compared to an axial displacement and a tilt. To maintain a Strehl ratio of over 0.8 the maximum individual deviation may not exceed:

- Lateral displacement: 240 µm
- Tilt: 215 µrad
- Axial displacement: 9.5 µm

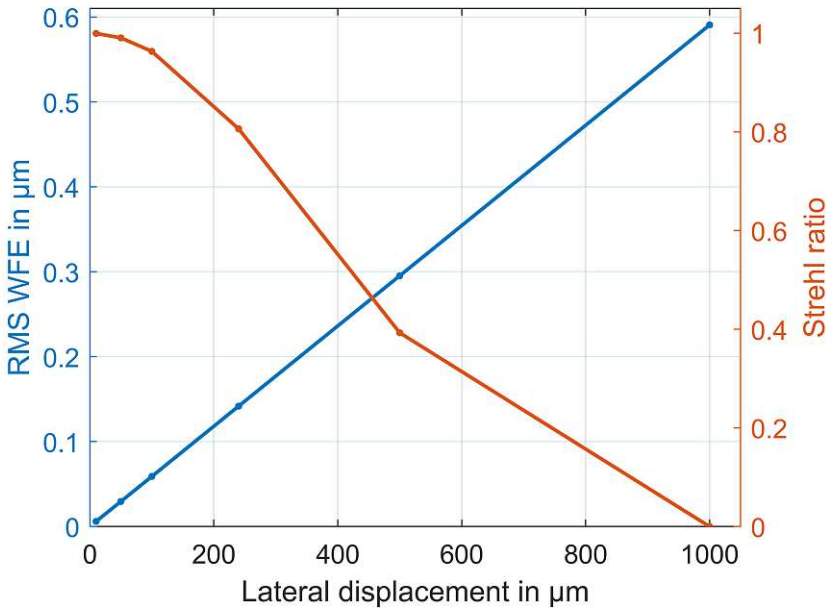

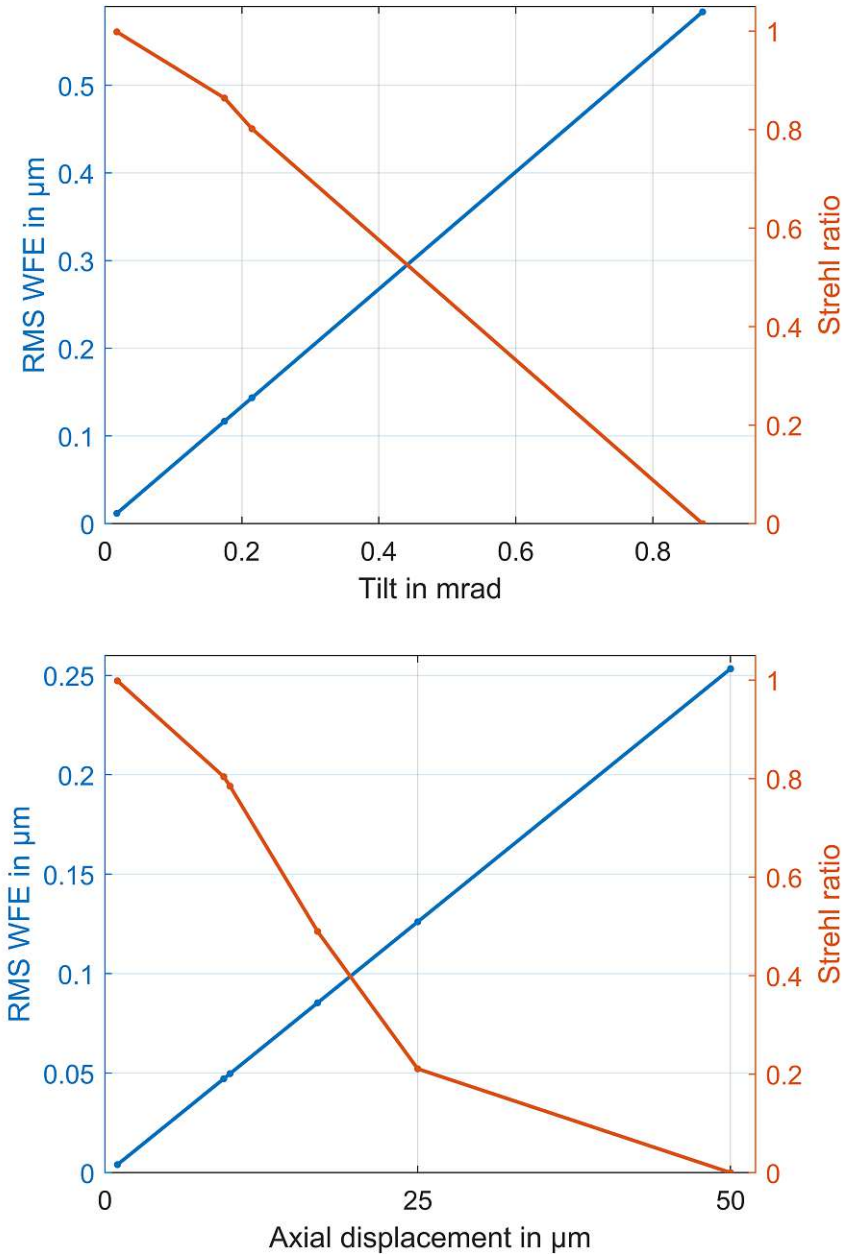

Figure 5.1: Sensitivity analysis of the LFO conducted in simulation with Zemax.

5.2 Design of the metrology mounting adapters

The adapter has some requirements it needed to fulfil. Firstly it needs to be attached as closely as possible to the primary mirror cell and the secondary mirror, so that changes in distance can be directly correlated to changes in distance between the mirrors and not any other mounting party built in between the adapter and the mirrors. Secondly a line of sight between the retroreflectors and the interferometer-heads has to be achieved. The only viable option to achieve the first two requirements was to mount the metrology system on the outside of the secondary mirror and at the opening of the primary mirror. However, this created a third requirement where the line of sight is not allowed to block the light path of the telescope. Lastly the design and connection between the adapter

and telescope should be stiff enough, as to not influence alignment or pick up vibrations while tracking.

In Figure 5.2 a schematic of the primary mirror ring adapter can be seen. The green area represents a position sensitive detector (PSD), which is used in a measurement for lateral displacement between the two mirrors in a different project and in black are the mounts for the interferometer-heads.

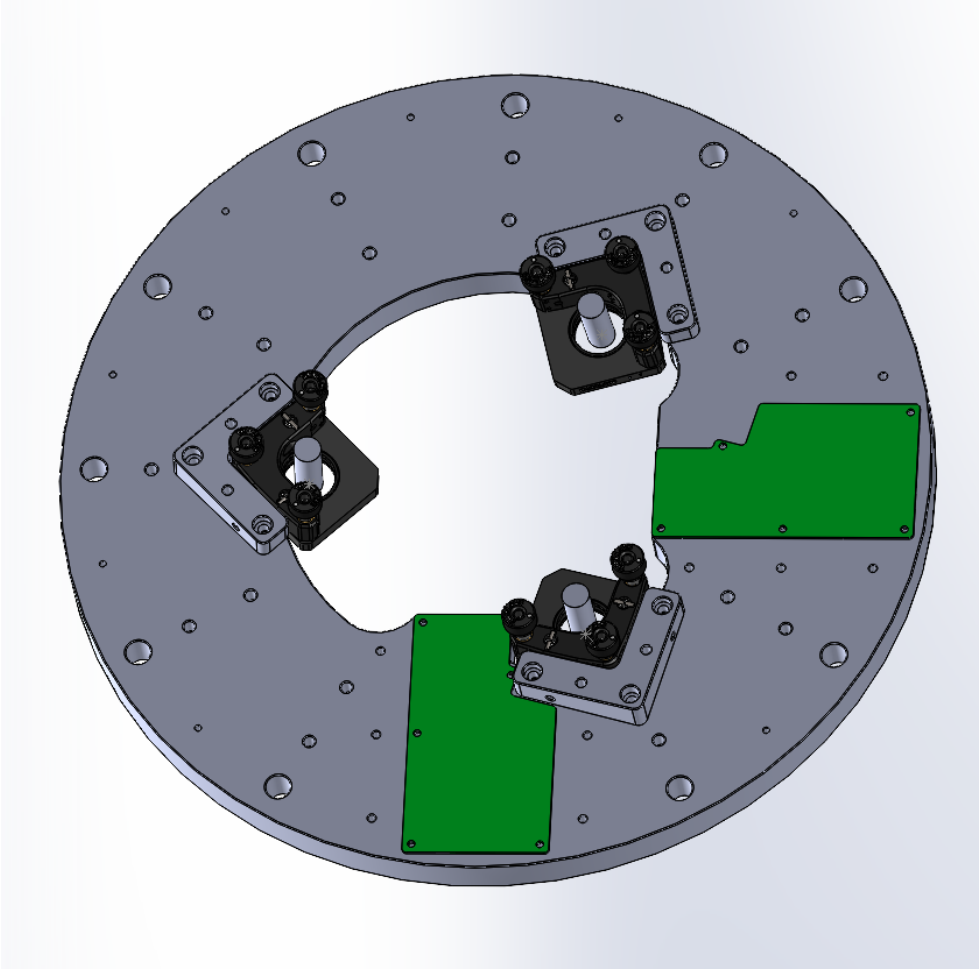

Figure 5.2: 3D-model of the PM ring adapter.

The manufactured parts from the design in Figure 5.2 can be seen in Figure 5.3 and 5.4.

Figure 5.3: Manufactured PM ring adapter.

Figure 5.4: Closeup of the PM and IF adapters.

Figure 5.5 shows the opening of the primary mirror, where the primary mirror ring adapter can be screwed in via ten M10 screws. Next to it in Figure 5.6 an adapter for the secondary mirror is shown. A retroreflector is already inserted and can be secured via four M3 screws. In total five of those adapters are mounted on the secondary mirror. Three have retroreflectors inserted as shown in the image and two have lasers mounted at the L-shape which point towards the PSD to measure lateral displacement. The bottom has a small ledge to attach to the edge of the secondary mirror and is slightly curved to match the curvature of the secondary mirror. The top has a notch for a metal cable tie, which was used to attach it to the secondary mirror.

Figure 5.5: Opening of the PM of LFO where the PM adapter is mounted.

Figure 5.6: Manufactured RR adapter.

In Figure 5.8 and Figure 5.9 the metrology system can be seen in full. The primary mirror ring adapter is attached to the telescope and the three interferometer-axis are

installed, in the distance the secondary mirror adapters with the retroreflectors can be seen as well. The red circle in Figure 5.7 is one of the guide lasers from the interferometer, which are used during the alignment phase. Ideally the interferometer-heads and the retroreflectors would be directly opposite from each other, as that would make the tip/tilt calculation slightly more straightforward but this could not be achieved without entering the light path, see Figure 5.7 for the closest possible.

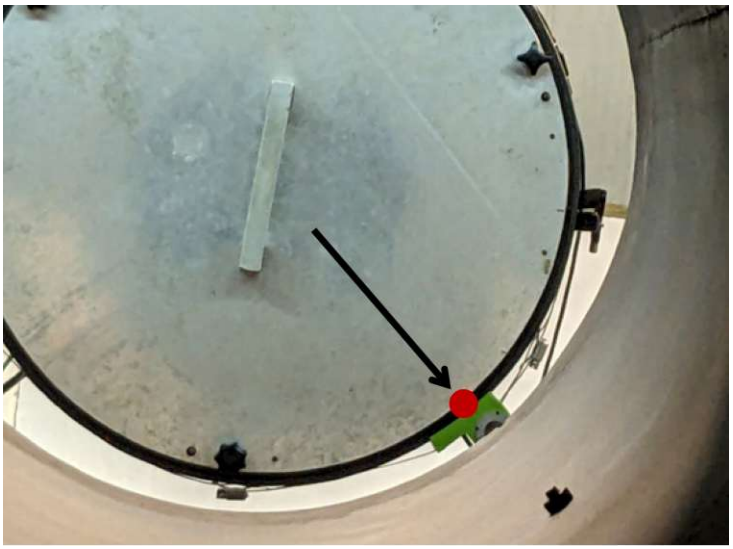

Figure 5.7: Maximum achievable tilt angle of the adjustment stage without entering light path.

This is why the retroreflectors are rotated on the secondary mirror circumference relative to the positions of the interferometer-heads, which slightly changes the setup for the tip/tilt calculation, see the end of Section 5 for more details.

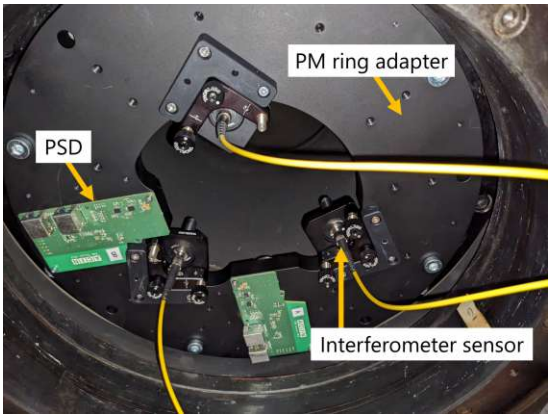

Figure 5.8: Mounted dimensional metrology system on PM side.

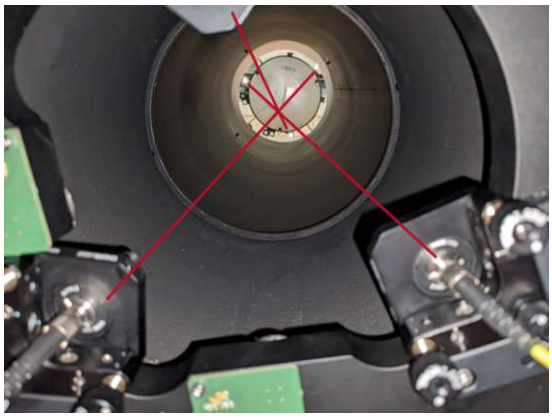

Figure 5.9: Alignment of the three IF axis with the three RR.

5.3 Measurement procedure

To perform measurements on the LFO, the metrology system and a laptop were securely mounted directly onto the telescope structure. They are connected via an Ethernet connection. A secondary laptop is used for monitoring and to remotely start the measurements. This allowed the measurements to be done with minimal physical interference.

Interferometer measurements were performed in multiple telescope positions, both while the telescope was stationary and while it was actively tracking. A precise list can be found in Table 5.1 in Section 5.4.2. For stationary scenarios, data was collected for 10 min per measurement, whereas measurements while in tracking mode were performed for 15 min to increase the likelihood of identifying any unsmooth or anomalous behaviour, as it was expected that the chances of finding any were higher while the telescope was tracking. Selected positions also were measured multiple times to verify the repeatability and consistency of the observed results.

Due to limitations of the unavailable remote access and multiple unfortunate weather conditions, the WFS measurements could not be performed. However, a step-by-step procedure is outlined to ensure that such measurements can be successfully conducted in future experiments.

First the adapter unit at the back of the telescope needs to be switched out to the one shown in Figure 5.11. As this adapter unit connects tightly to the back of the telescope the fiber cables need to be carefully routed through the adapter making sure that they do not cross the lightpath. Then the backplate shown in Figure 5.10can be screwed to the adapter unit and the WFS can be attached. A camera can be attached to the other side of the adapter unit and with a lever the lightpath can be switched between the two exits or the same approach that is shown in Section 5.5 can be chosen, where the camera and WFS connect to the same end via a beamsplitter.

Figure 5.10: Connection between the WFS and the backplate of the telescope.

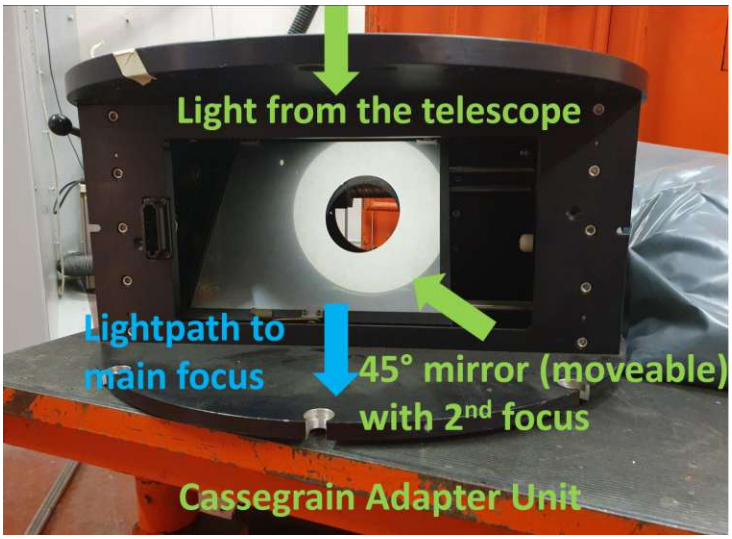

Figure 5.11: Adapter unit of the LFO for the WFS.

Tip/tilt calculation For the LFO setup the conversion has been done analogue to the small RC-telescope. A detailed derivation can be found in Chapter 3.3 in [15]. The only difference is the position of the interferometer heads and their pairing to the retroreflectors, which does not change anything for the principle of the calculation. An illustration of the interferometer head and retroreflector pairing can be seen in Figure 5.12.

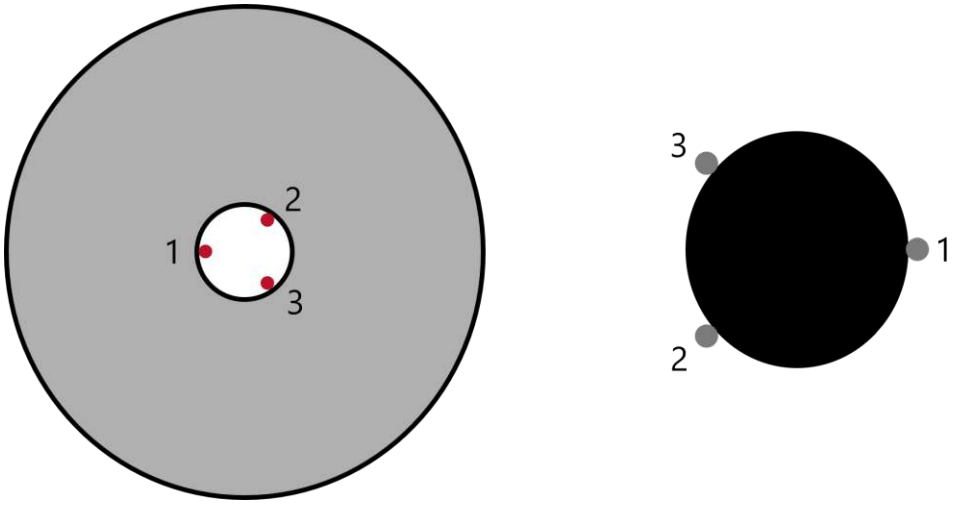

Figure 5.12: Overview of the position of the interferometer heads (left) and their paired retroreflector (right).

5.4 Results of the LFO

In this section the results for the dimensional metrology system for the Leopold Figl-Observatory will be presented, as well as a proof of concept for the WFS. In total 20 measurements were done in different positions, while the telescope was standing still and while the tracking was enabled. Some positions were measured multiple times to see if the behaviour remains the same and two measurements showed some irregular behaviour. First all the individual measurements will be presented and after a comparison between the different measurements and positions will be made. To make it easier to distinguish

between measurements with and without active tracking, the measurements with tracking enabled are framed. Following this section there is also a full summary of the results in Table 5.2.

5.4.1 Individual measurements

Zenith Three measurements in the Zenith position (RA = 0°, Dec. ≈ 48°) were performed. Figure 5.13a was the very first measurement taken and is one out of two measurements that show some irregular behaviour, in this case it could be due to a cable being pulled. The other two measurements show a similar behaviour to the rest of the measurements, with an axial distance change of a few micrometers and a tip/tilt change in the range of $(0 - 3)\mu$m.

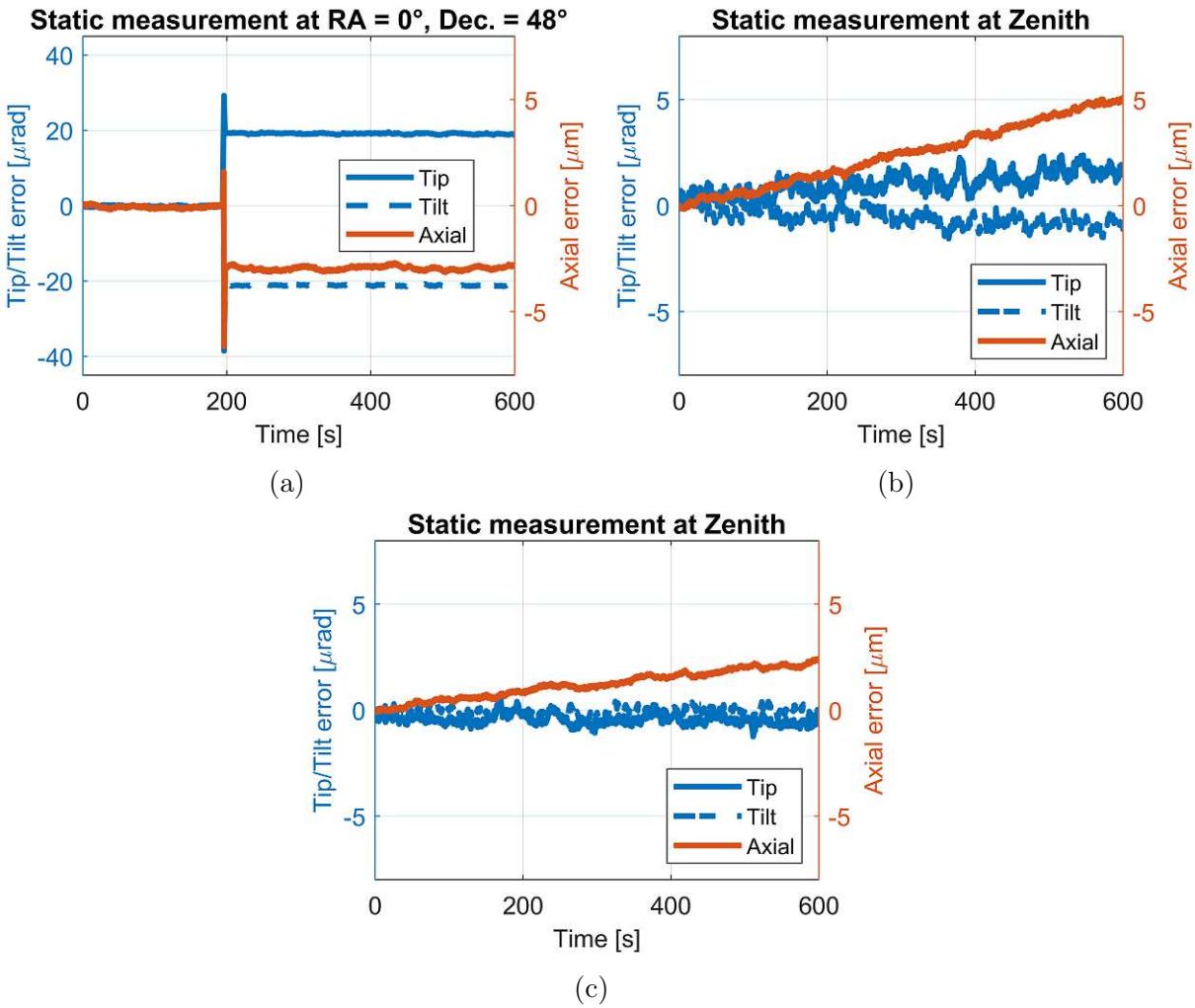

Figure 5.13: Collection of the dimensional measurements in the Zenith position. The irregular behaviour of the first measurement could be due to a cable being pulled

South Six measurements were performed with the telescope pointing southwards. Different declinations and the tracking mode were tested. This direction has the most measurements since it is the most relevant for observations. Interesting to see is that in Figure 5.14a the position seems to be very stable, but when repeating the same measurement in the same position at a later time an axial drift can be seen again.

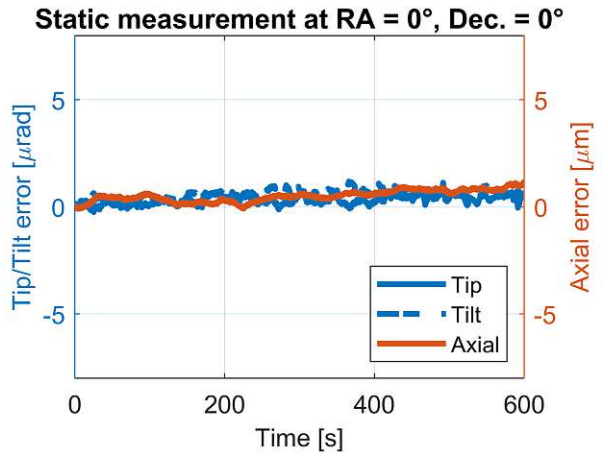

(a)

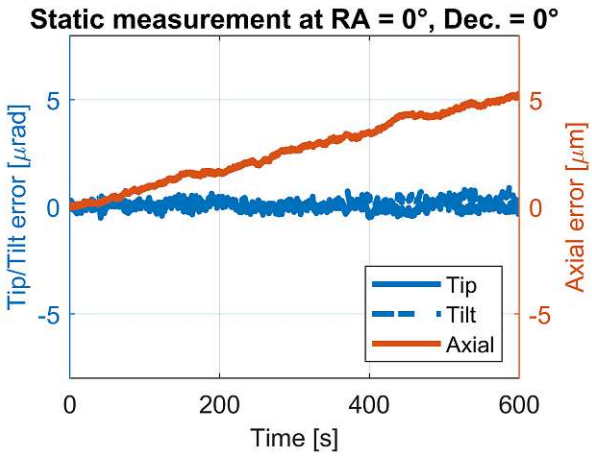

(b)

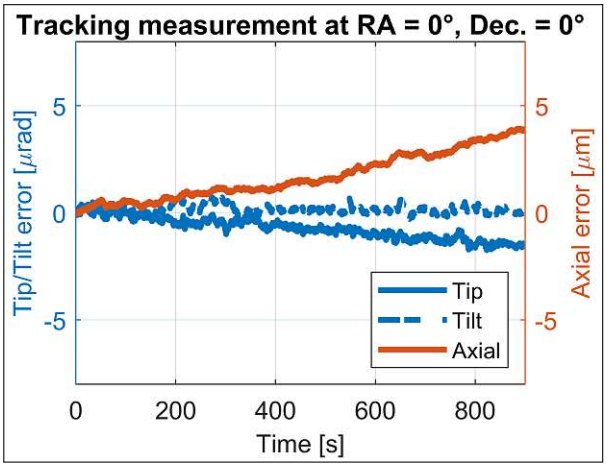

(c)

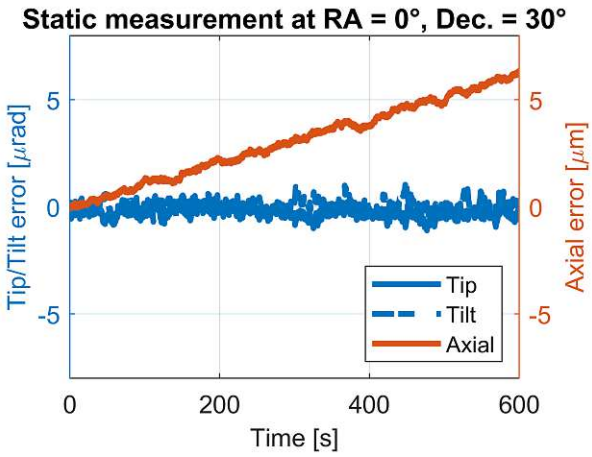

(d)

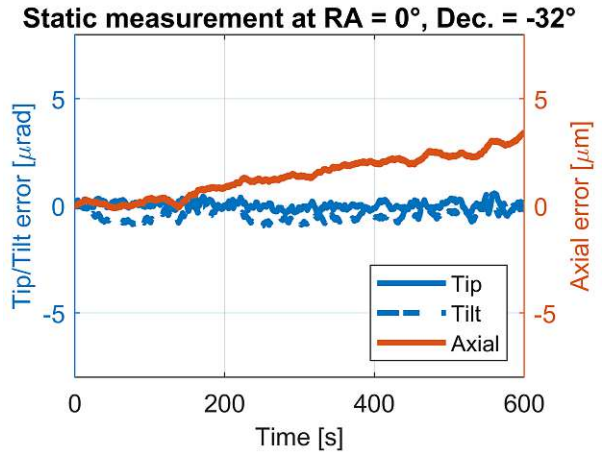

(e)

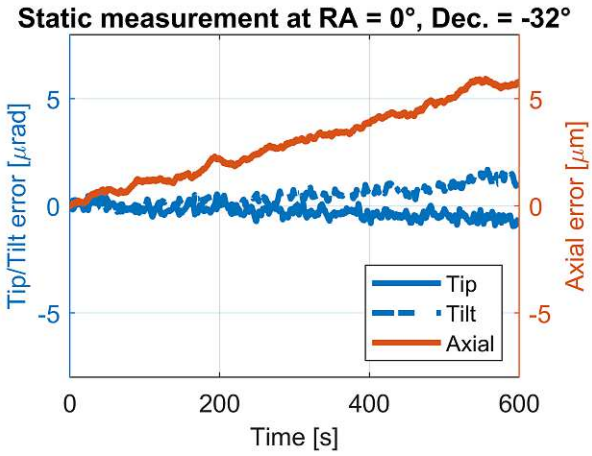

(f)

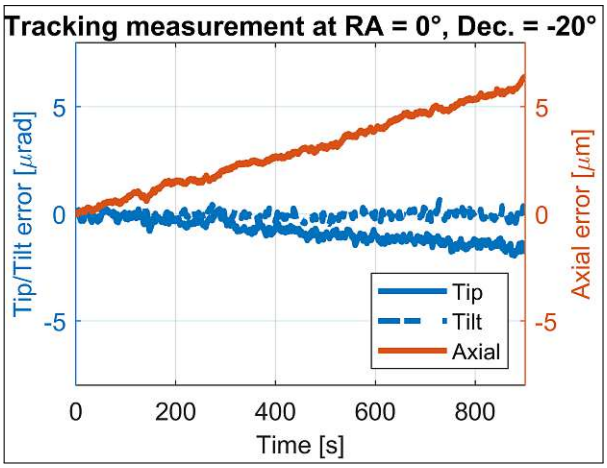

(g)

Figure 5.14: Collection of the dimensional measurements pointing southwards.

East Four measurements were done in an eastern direction. Two positions were selected and measured twice on separate days. In Figure 5.15a and 5.15b it can be seen that while tip and tilt are stable and stay very small, the axial error is slightly larger in the second measurement. The position of Figure 5.15c was very stable in the first measurement but in the second attempt some irregular behaviour was observed. It is unclear what happened there and if this is connected to the tracking.

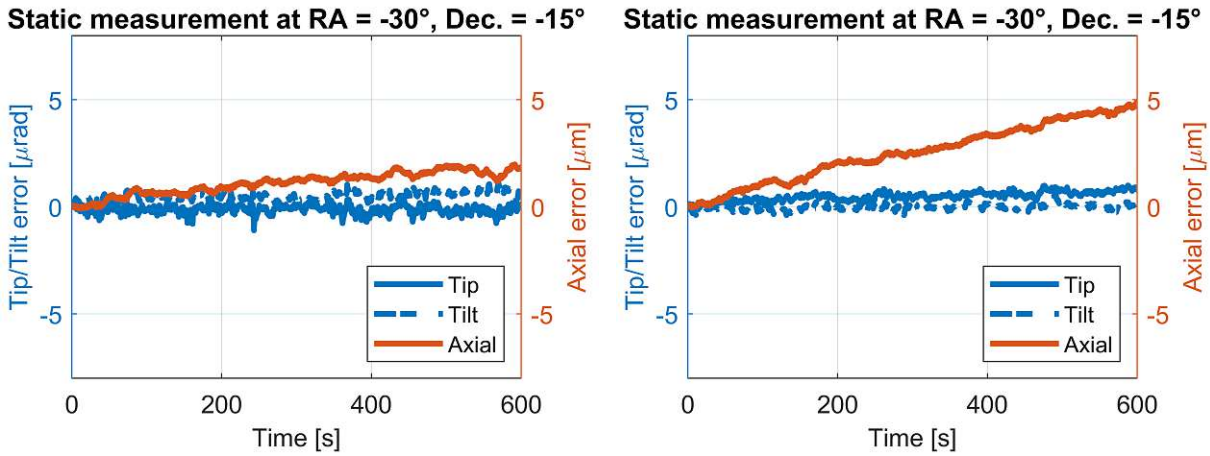

(a) (b)

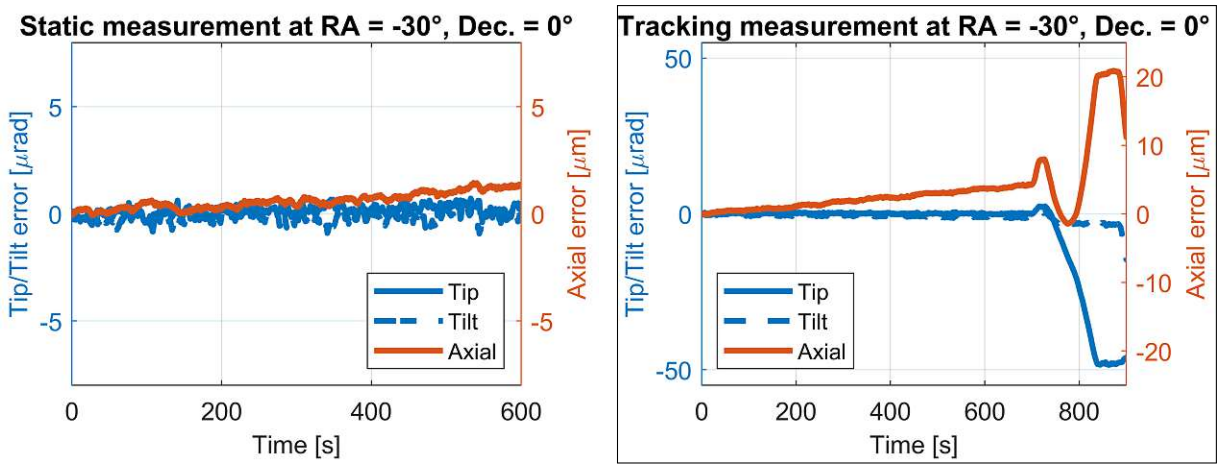

(c) (d)

Figure 5.15: Collection of the dimensional measurements pointing in an eastern direction.

West Again four measurements were taken. Two positions were selected and measured twice on separate days. Figure 5.16a and 5.16b show almost the exact same behaviour, while in the second position, there is a noticeably larger axial drift in the second attempt, which can be seen in Figure 5.16c and 5.16d.

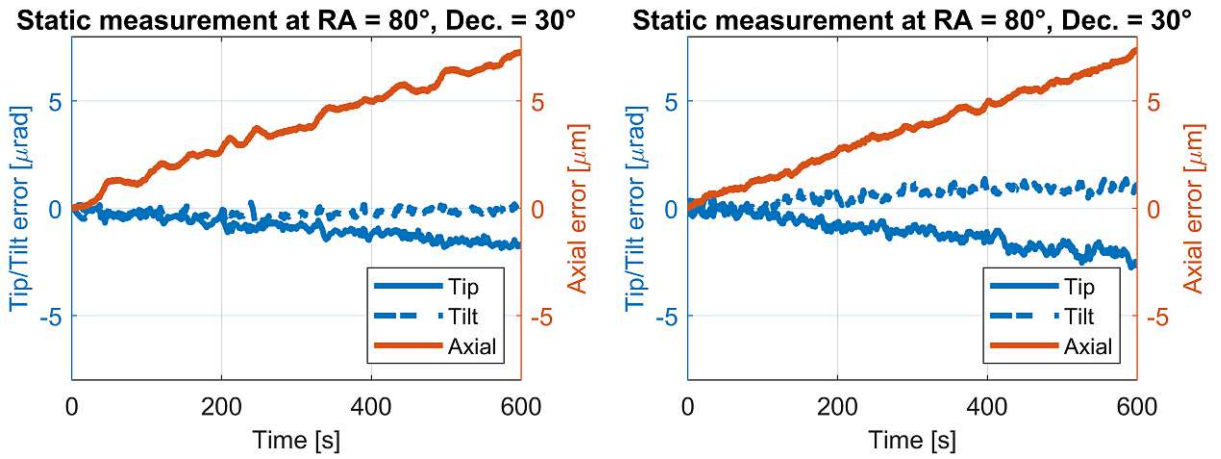

(a) (b)

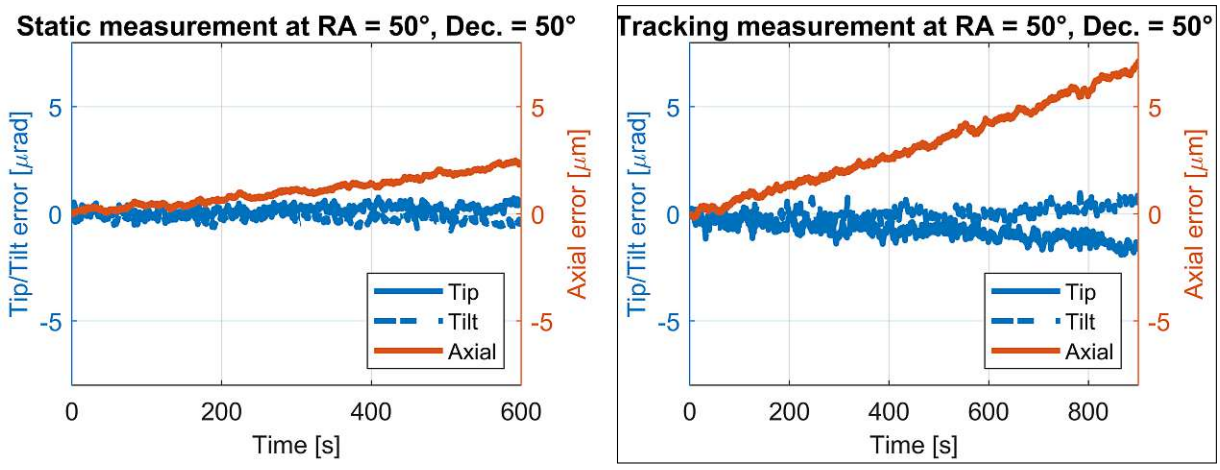

(c) (d)

Figure 5.16: Collection of the dimensional measurements pointing in a western direction.

Pole For the pole measurement, the telescope was flipped, which means gravity pulls more on the opposite side of the telescope structure than most of the time. One measurement was performed and after a few different positions the measurement was repeated while enabling a manual tracking mode. A very similar behaviour can be seen in both measurements, with no noticeable change in Figure 5.17b when tracking was enabled.

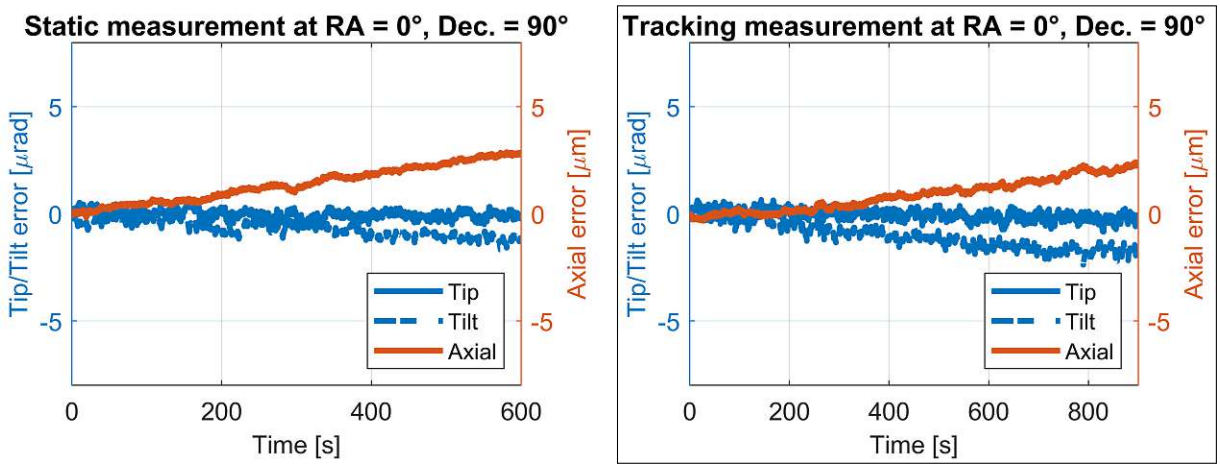

(a) (b)

Figure 5.17: Collection of the dimensional measurements in the Pole position.

5.4.2 Comparison of absolute distances

This section compares the absolute distances and sets them in relation to the first measurement as a reference. In Table 5.1 the measurements are listed chronologically, with their pointing direction and whether tracking was enabled or not, which also means whether the measurement took place for 600 s or 900 s.

Figure 5.18 shows the absolute axial distance change in relation to the first measurement. Only the axial distance change has been chosen to be shown, since the observed changes in tip/tilt have a much smaller impact on image quality according to the sensi-

Table 5.1: Metadata for Measurements.

	Measurement #	Right Ascension (RA)	Declination (Dec)	Mode
Day 1	1	0°	48°	Static
	2	−30°	−15°	Static
	3	−30°	0°	Static
	4	0°	0°	Static
	5	0°	−32°	Static
	6	80°	30°	Static
	7	50°	50°	Static
	8	0°	0°	Tracking
Day 2	9	0°	30°	Static
	10	0°	47°	Static
	11	0°	0°	Static
	12	0°	−32°	Static
	13	0°	−20°	Tracking
	14	−30°	−15°	Static
	15	−30°	0°	Tracking
	16	50°	50°	Tracking
	17	0°	90°	Static
	18	80°	30°	Static
	19	0°	90°	Tracking
	20	0°	48°	Static

tivity analysis from Figure 5.1. The maximum tilt value of the regular individual measurements is 2.3 µrad and the maximum tip value is 2.8 µrad, which is 94 and 77 times smaller than the maximum individual deviation allowed to maintain a Strehl ratio above 0.8. The maximum axial distance change for all individual measurements is 7.4 µm, which would already reduce the Strehl ratio to 85.2% according to the sensitivity analysis.

In Table 5.2 all the results of the individual measurements are summarised. The two irregular measurements have been excluded from this calculation. When comparing those numbers with the values of the sensitivity analysis, it can be predicted how the individual errors would affect the Strehl ratio. It can be seen that the distance changes observed during individual measurements have little effect on image quality when looking at the average standard deviation. The observed axial shift is much more noticeable than tip/tilt, especially when the error propagation would proceed at the same rate over longer measurements. Since already over a relative short period of time, the maximum observed axial deviation already reduces the Strehl ratio to 85.2%.

Table 5.2: Summary of maximum and average standard deviation of the individual measurements.

	Day 1			Day 2		
	Axial [μm]	**Tip** [μrad]	**Tilt** [μrad]	**Axial** [μm]	**Tip** [μrad]	**Tilt** [μrad]
$\boldsymbol{\Delta_{max}}$ / **SR** [%]	7.29/85.4	1.86/100	1.19/100	7.40/85.2	2.76/100	2.38/100
$\boldsymbol{\sigma}$	0.84	0.28	0.21	1.44	0.34	0.32

The blue circles in Figure 5.18 represent the mean value of the individual measurement and the slightly hard to see errorbar is the standard deviation of each measurement. There is a big gap between measurement 8 and 9, which is most likely caused because the first eight measurements were performed on one day and the following measurements on a different day and a very small alignment adjustment, by turning two out of the three thumbscrews where the interferometer heads are installed, had to be made. This does not rule out that the telescope mirrors itself could have moved as well.

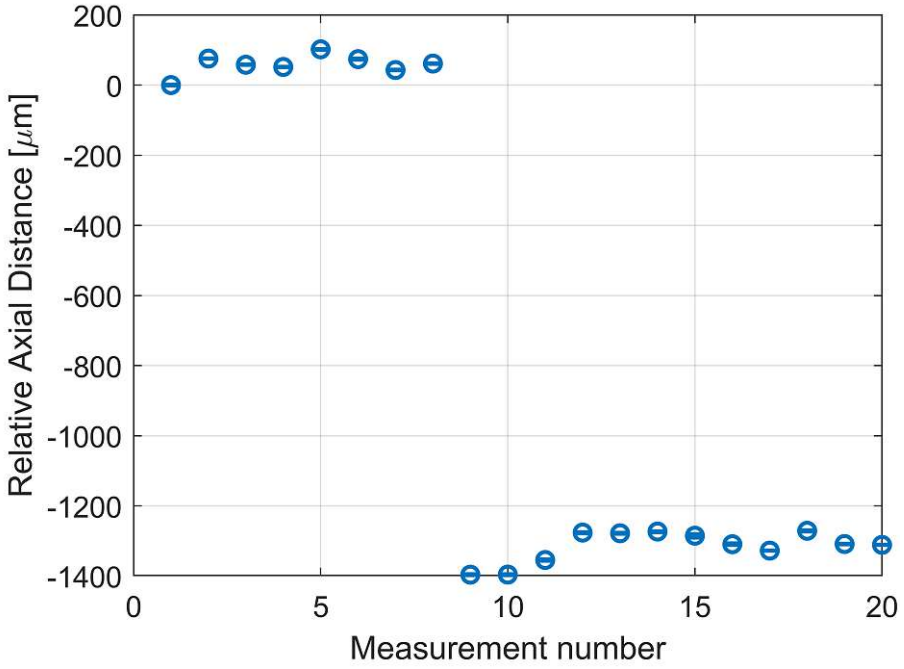

Figure 5.18: Absolute axial distances of all individual measurements relative to the first measurement, with their respective errorbars.

Since there is such a big gap between the two measurement days, they are also both plotted separately for a closer comparison. In Figure 5.19 the first eight mean absolute axial distances are plotted relative to the first one. It is clearly visible that the distance change when moving to a different position is much larger than during a single measurement. Therefore checking alignment after moving to a new position and before starting an observation is very important.

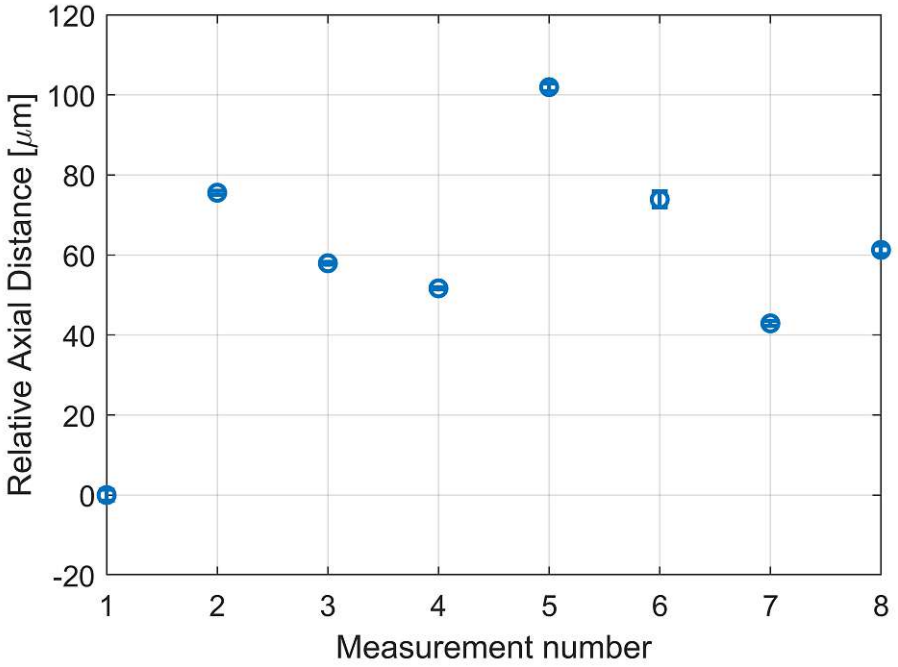

Figure 5.19: Absolute axial distances of the first eight measurements with errorbars.

In Figure 5.20 the last twelve mean absolute axial distances are plotted relative to the first of that day. The distance changes are in a very similar range as on the first measurement day. One measurement shows a significantly larger standard deviation than the rest but it is unclear what could have happened during this measurement.

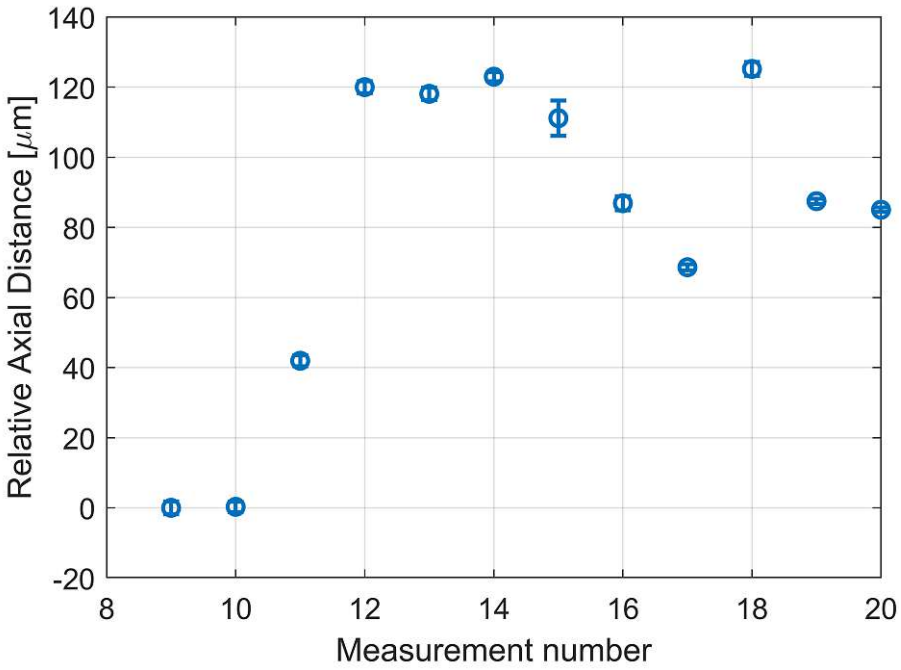

Figure 5.20: Absolute axial distances of the last twelve measurements with errorbars.

In Table 5.3 a summary of the comparison of the absolute axial distance changes between all positions can be found. The standard deviation σ of the measurement points of Figure 5.18 - 5.20 and the largest deviation between two positions are taken. The Strehl

ratio is again taken from the sensitivity analysis. It can be seen that the distance changes when switching to a new position can affect the Strehl ratio significantly. In comparison to the calculated limit of 9.5 µm axial shift for a seeing limited imaging performance, significantly larger values are observed, indicating a severe reduction of the Strehl ratio. Especially when considering all 20 measurements, where there was a significant jump between the two measurement days but also when considering the two days separately, which was done since the jump most likely occurred while readjusting alignment.

Table 5.3: LFO summary of absolute axial distance changes.

	Measurements		
	All	**1-8**	**9-20**
$\boldsymbol{\Delta_{max}}$ [μm]	1457.61	75.56	78.04
$\boldsymbol{\sigma}$ [μm] /**SR** [%]	691.62 / 0	29.60 / 17.20	45.08 / 4.15

5.5 ACINOGS

Since a WFS measurement was not possible at the Leopold Figl-Observatory, although everything was prepared and works in theory, the setup was tested at a different telescope. For this purpose a small adapter was built which combined a camera (ZWO ASI 185) and the WFS through a beamsplitter, which allowed for them to used at the same time. The distance of the two instruments from the focal point was tested in the lab and the camera was attached to a linear stage for finetuning. This helped with getting good initial focus when using it with the telescope. The camera also helped with centering the star so that it would appear in the FoV of the WFS. Figure 5.21 shows the ACINOGS, an 80 cm RC-telescope, where the measurement system was attached and Figure 5.22 shows the described adapter.

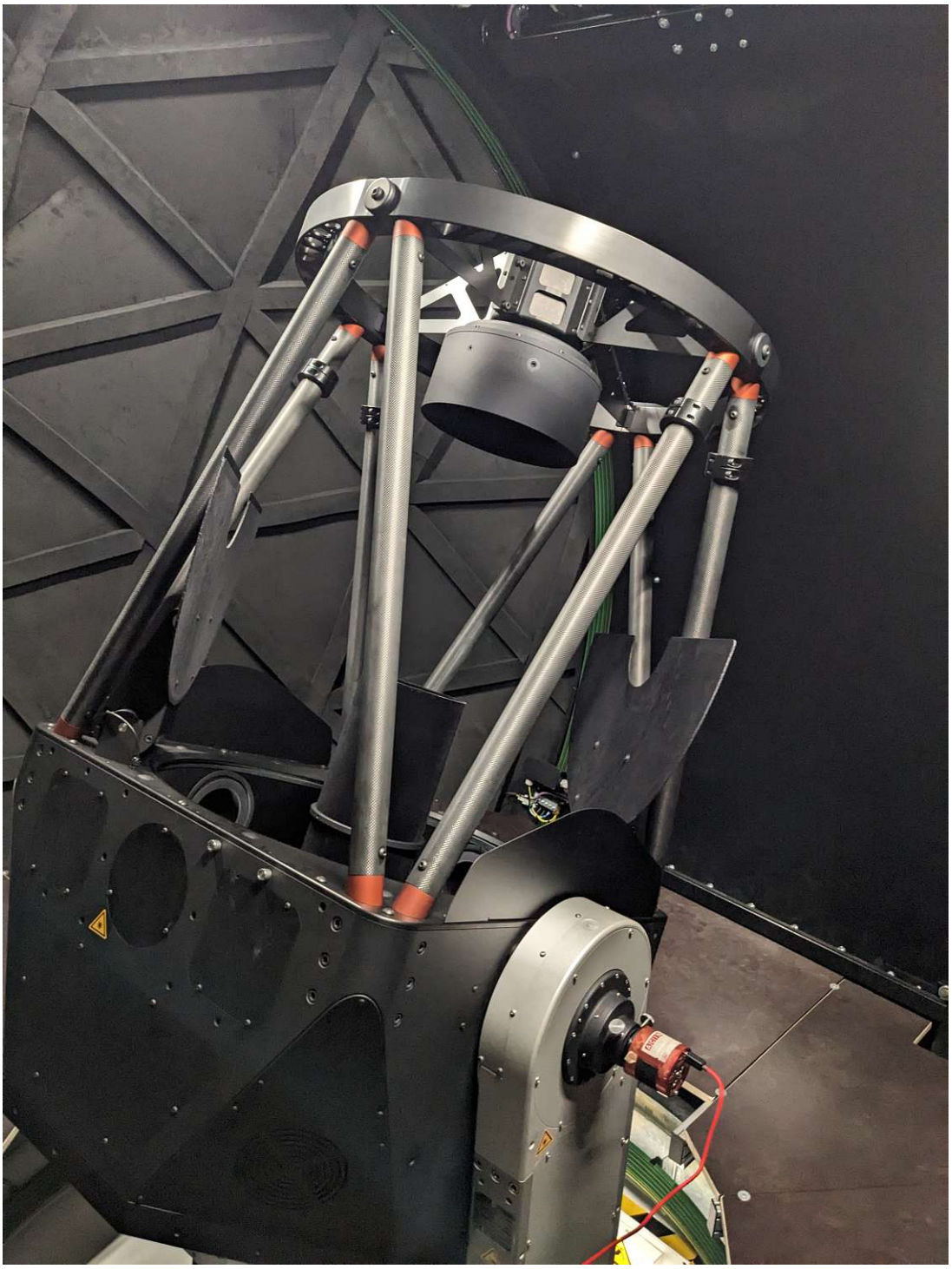

Figure 5.21: ACINOGS of TU Wien located in Science Center Arsenal.

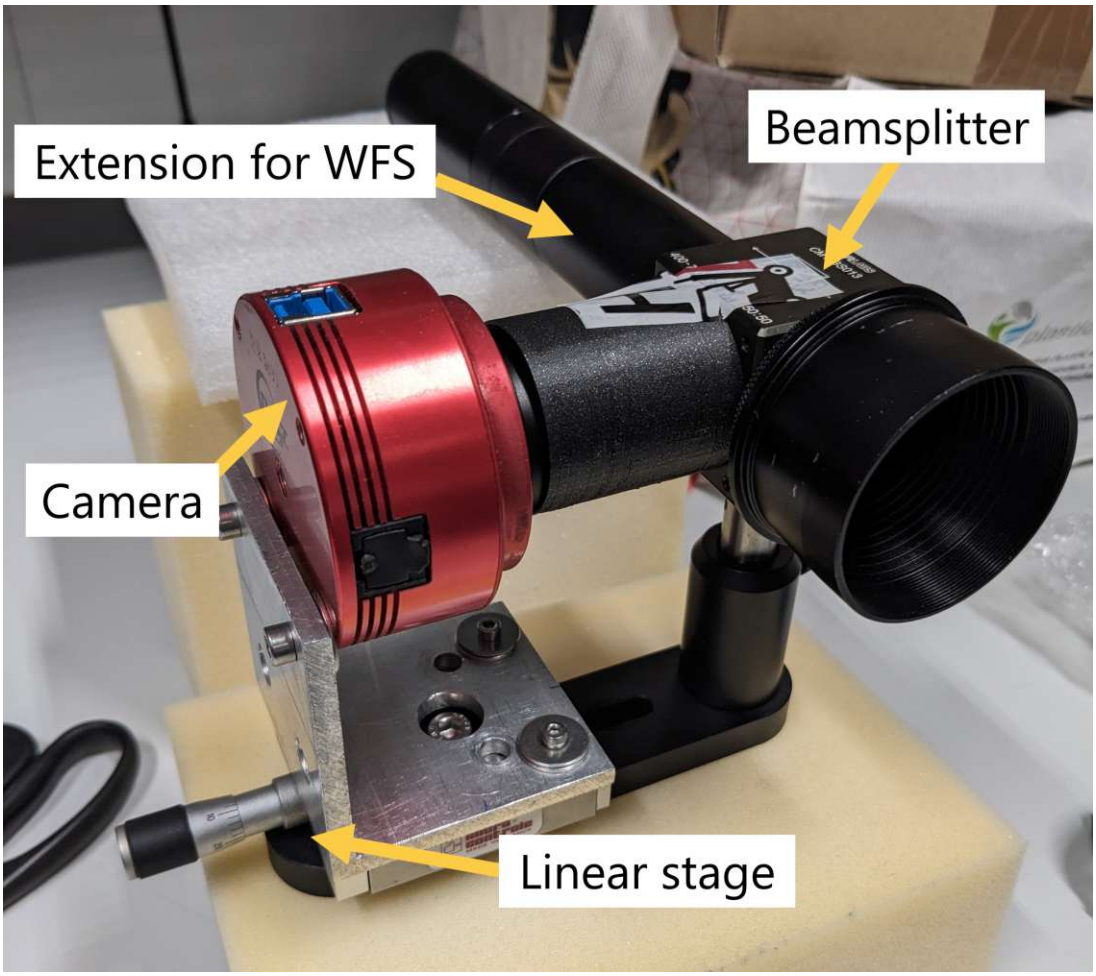

Figure 5.22: Adapter for simultaneous mounting of camera and WFS.

5.6 WFS proof of concept at ACINOGS

After the initial setup the tracking worked flawlessly judging by eye with no noticeable drift in the camera or WFS. Due to very strong winds the dome closed during some measurements but one 15 min measurement and one 5 min measurement were uninterrupted. Since the used star was a lot dimmer than the artificial star in the previous experiment data acquisition could only be performed at 1 Hz and a moving mean over 65 and 25 data points was used. The left part of Figures 5.23 and Figure 5.24 show the absolute errors and the right part shows the error propagation with a calculated RMS WFE. Tip and tilt have been purposefully left out, because that error can not only be contributed to the telescope but also to the pointing accuracy.

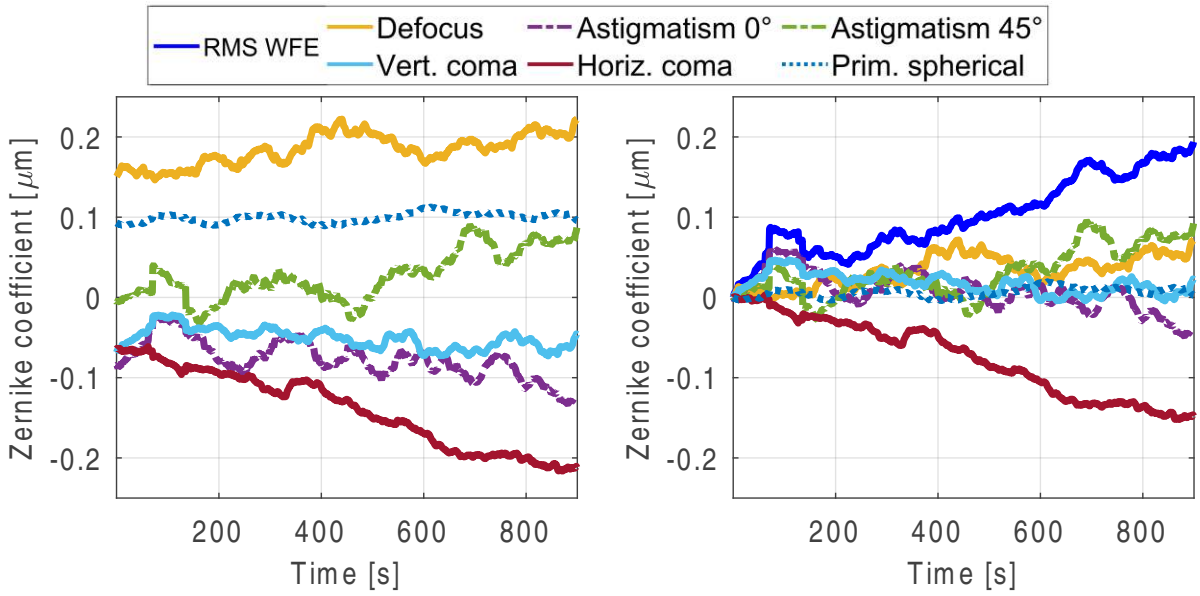

Figure 5.23: Groundstation WFS measurement over 15 min. The left part shows the absolute errors and the right part the error propagation and RMS WFE.

The average RMS WFE of Figure 5.23 is 102 nm and the maximum is 194 nm. For a reference wavelength of 500 nm this corresponds to a Strehl ratio of 19.3% and 0.3%. It is visible that most errors fluctuate both in the positive and negative direction, only horizontal coma shows a clear trend. The average RMS WFE of the five minute measurement in Figure 5.24 is 90 nm and the maximum is 149 nm. This corresponds to a Strehl ratio of 27.8% and 3.0%. The clear trend of horizontal coma was not observed again in this measurement.

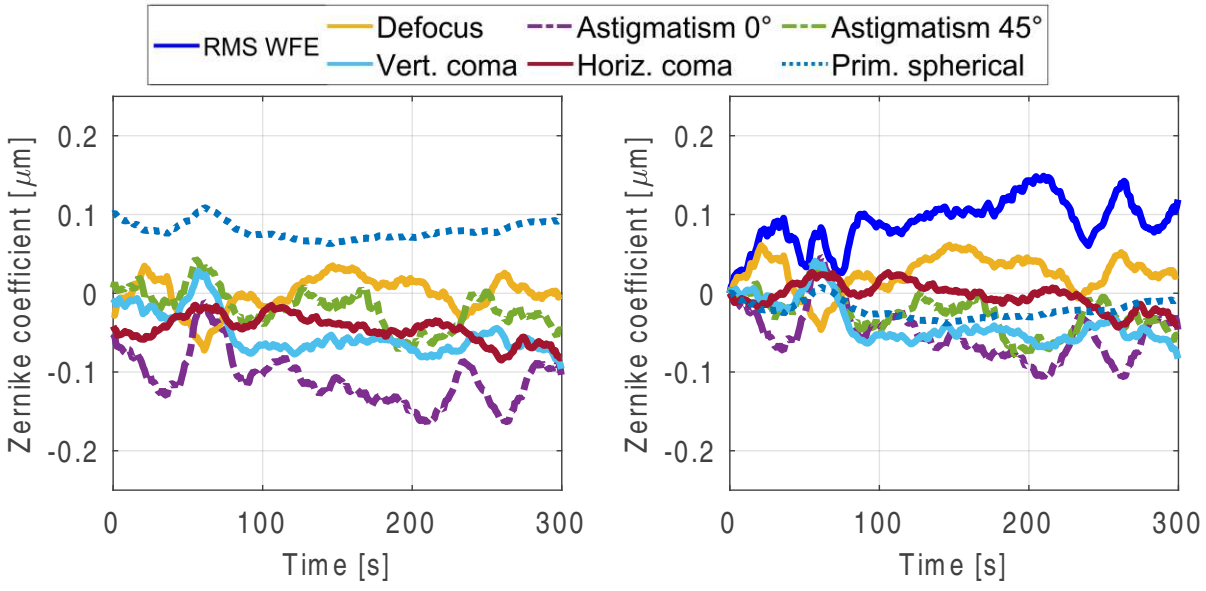

Figure 5.24: Groundstation WFS measurement over 5 min. The left part shows the absolute errors and the right part the error propagation and RMS WFE.

The measurement worked as intended, a continuos data acquisition was possible even when interrupted by the dome closing. As for the results a significant degradation can be

observed, which is not unreasonable given the wind conditions at the time. Wind speeds averaged at around 60 km h^{-1} (16.7 m s^{-1}) and peaked at over 100 km h^{-1} (27.8 m s^{-1}). This most likely influenced the wavefront error significantly, potentially introducing structural vibrations causing misalignments. Coma's dominance in the first measurement could be an indicator of asymmetric distortions in the optical system, likely resulting from shifts in the optical axis due to wind exposure. The automatic closure of the dome during wind peaks highlights the severity of the conditions, as they are designed to protect the telescope among other things from too much mechanical stress caused by extreme winds.

As a next step if further analysing of this telescope is desired a repeated measurement under better conditions could verify these explanations.

5.7 Discussion

The dimensional metrology and WFS systems were successfully installed at the LFO, which features an aperture of 1.52 m and a distance of roughly 3.46 m between primary and secondary mirror. Out of the 20 individual measurements conducted, 18 showed a very similar behaviour, averaging around 4.54 µm of axial displacement per individual measurement and a combined tip/tilt error of 0.87 µrad, both representing the difference between the starting and end points. Based on the sensitivity analysis, these errors are estimated to result in a Strehl ratio of 92.36% and of over 99% respectively. When looking only at the standard deviations, which can be seen in Table 5.2, the Strehl ratio stays at over 97% for the axial error and at over 99.9% for the tip and tilt error.

The first anomalous measurement, shown in Figure 5.13a, could be explained by a component still settling or a cable being inadvertently pulled, since it was the very first measurement. The second measurement (Figure 5.15d) however, does not have an immediate explanation. Using the values from Figure 5.18-5.20, a mean absolute distance and standard deviation can be calculated. A quick summary is shown in Table 5.3. It can be seen that the axial distance change between positions is much larger than during individual measurements. Even when looking at the two days separately a standard deviation of 29.60 µm and 45.08 µm is recorded, which lowers the Strehl ratio way below 80% to 17.20% and 4.15% respectively.

This significant change in distance between positions could largely be compensated for by checking the alignment before each observation. In addition, the existing secondary mirror focuser could be used to actively track and correct any axial changes that occurred. This would not require any additional hardware modifications to the telescope. Implementing this approach could provide an effective compensation method with minimal changes. Furthermore, to improve overall stability, it may be beneficial to remove the rotating secondary mirror mount. Originally designed to support different observing modes, this setup adds unnecessary weight and mechanical uncertainty. Reducing the mass of the secondary mirror assembly could help minimise mechanical flexure and improve alignment stability. It is also important to note that lateral displacement measurements were not considered in this thesis, but may contribute significantly to the overall wavefront error. This may require a more complex compensation approach.

The WFS setup was also successfully installed and tested on another 80 cm RC-telescope. However, the telescope's performance or the magnitude of the errors observed during these tests may not be considered conclusive due to the extreme wind conditions at the time. The setup was designed in such a way that with the right adapter it can be used at any telescope in combination with a camera, making it much easier to get

a proper alignment and a good initial focus. Simultaneously the point spread function could also be measured if desired.

The implemented dimensional metrology system was successfully adapted and used for characterization for the LFO. The measurements indicate a significant change of the imaging quality due to axial displacement, which however could be compensated by the integrated secondary mirror focusing unit.

6 Conclusion and outlook

In the course of this thesis an active compensation system of the secondary mirror for a small RC-telescope was tested and its performance was verified by introducing disturbances and performing a simultaneous measurement with a WFS. Furthermore the existing dimensional metrology and WFS system was adapted and implemented at the Leopold Figl-Observatory (LFO). The metrology system was used extensively at the LFO and the WFS setup was tested at a different telescope with a real star, due to weather conditions and unavailable remote control. The results are summarised below with answers to the research questions. Finally, possible suggestions for improvement and possible approaches for future work are presented.

6.1 Conclusion

The goal of this diploma thesis was to first investigate the suitability of an active optics system that requires no light from the telescope and verify its performance with a simultaneous use of a WFS and secondly to install the tested dimensional metrology system at Austria's largest telescope, the Leopld Figl-Observatory, and analyse its behaviour and any possible changes in multiple measurements.

The results of this work will be discussed in the next section in relation to the research questions formulated in Section 2.5.

Research question 1. *What are the factors limiting imaging quality at the Leopold Figl-Observatory?*

Originally designed to support multiple observing modes, the secondary mirror mounting at the LFO is now exclusively used in its RC-mode. However, its additional weight and complexity may introduce mechanical instabilities and misalignment issues. Also with the observatory being over 50 years old, its design standards and materials may no longer align with those of modern more modern observatories, potentially affecting overall performance.

Misalignment of optical elements, particularly collimation issues in the secondary mirror, could also be a limiting factor. Common aberrations such as coma, astigmatism, and spherical aberration degrade image quality but could be mitigated through improved optical alignment or higher mirror quality.

Measurement results show a significant change in axial direction (up to 78.04 µm max.) when moving the telescope to different poses. Tip and tilt changes are small (2.76 µrad max.). This indicates a significant axial mechanical movement of the secondary mirror with respect to the primary mirror and results in a degradation of the imaging quality.

Research question 2. *Can the expected distance changes at the Leopold Figl-Observatory be effectively measured with dimensional metrology?*

A sensitivity analysis was carried out to determine the relationship between axial distance change and tip/tilt with Strehl ratio. To maintain a Strehl ratio above 0.8, a maximum axial change of 9.5 µm and a maximum tilt of 215 µrad were determined as thresholds for seeing limited performance. These distances could be easily and accurately tracked in a similar but much smaller setup.

Building on this, the dimensional metrology system and WFS were successfully implemented at the LFO. The chosen interferometer demonstrated its capability to monitor position changes over about 4 m with sub-micrometer precision. Of the 20 individual measurements conducted in various poses of the telescope, 18 provided consistent results and 2 showed some irregular behaviour. Although alignment complexity increases with telescope size, once properly set up, this did not hinder reliable data acquisition.

The 18 measurements with consistent results indicate a max axial distance change of 78 µm, which has a significant influence on the imaging quality. Even with excellent initial alignment the observation is affected by this behavior.

Overall, the dimensional metrology system proved to be effective for the mechanical analysis of the LFO and it was possible to identify potential areas for improvement with suggestions for possible solutions. Given its ability to provide consistent and reliable data across different telescope positions and operating modes, this research question can be answered with yes.

Research question 3. *Is a wavefront sensor suited to monitor image quality despite atmospheric turbulences?*

This has been tested with a small RC-telescope and an artificial star in the city center and an 80 cm RC-telescope on a real star and both times data acquisition was possible. For the small RC-telescope the data of the WFS could be compared to the one of a dimensional metrology system. The dimensional metrology system showed that thermal gradients of over 20 °C leading to an axial displacement of over 25 µm could be easily compensated for reducing it by a factor of 82.0 and reducing the combined tip/tilt error by 11.3 during the heating phase. The simultaneous WFS measurement confirmed this by measuring similar but smaller errors and observed a reduced axial displacement by a factor of 12.7 and by a factor of 9.6 for the combined tip/tilt error in the case of active compensation. With the active optics system turned on all measurements managed to maintain a SR of over 80%, reducing the RMS WFE from 185 nm to 46 nm while heating the system. Considering only the aberrations that are actively targeted by the compensation system the RMS WFE could be reduced from 167 nm to 13 nm keeping the SR at 98.3%. The external metrology system's independence from the telescope's light path ensures versatile and continuous performance monitoring without sacrificing observational efficiency. The thermal experiments also showed that while not all aberrations could be entirely mitigated, the system stabilized the telescope effectively within its three degrees of freedom. In all those measurements the WFS delivered reliable data even at locations with high turbulences, which lets the research question be answered with yes.

6.2 Outlook

To get a complete understanding of the compensation system of the small RC-telescope, the combined measurement can be performed without interruption to see if the aberrations go back to their original values especially defocus, tip and tilt or if the discussed discrepancy remains.

As a next step, once the remote control of the LFO is working again, an optical analysis using the WFS module as described in this thesis should be performed. This should give a deeper understanding of the performance of the telescope and can be compared to the data of the dimensional metrology system. If the results match, the existing secondary mirror

focuser could be repurposed to actively compensate for the observed axial displacements. Since the focuser already provides control over axial positioning, integrating it into the compensation system would offer a straightforward and effective method to correct drifts and maintain optical alignment. In the case of a different WFS result, a deeper look into possible compensation systems should be taken. This should involve the secondary mirror structure and possible actuation based on some combination of the metrology and WFS data. Furthermore, more measurements with the metrology system can be performed to get a better understanding of the very few irregular behaviors and their possible cause.

For large telescopes like the LFO, direct actuation of the secondary mirror (similar to the small RC-telescope) could be explored as a cost-effective and less complex alternative to the hexapod system, especially since it already proved to be very successful for the small RC-telescope. This approach would require detailed modelling and validation to ensure it meets the necessary requirements.

By addressing these points, future research will bridge the remaining gaps in system integration and evaluation, and be able to make more detailed suggestions to further improve image quality for the LFO.

References

[1] R. N. Wilson, *Reflecting Telescope Optics II*, 2nd ed. Berlin-Heidelberg: Springer Verlag, 2001.

[2] S. L. Grimm, B.-O. Demory, M. Gillon, *et al.*, "The nature of the TRAPPIST-1 exoplanets," *Astronomy & Astrophysics*, vol. 613, A68, 2018. DOI: 10.1051/0004-6361/201732233.

[3] T. R. Slatyer and C.-L. Wu, "General constraints on dark matter decay from the cosmic microwave background," *Physical Review D*, vol. 95, no. 2, p. 023 010, 2017. DOI: 10.1103/PhysRevD.95.023010.

[4] R. Schwenn, "Space weather: The solar perspective," *Living Reviews in Solar Physics*, vol. 3, 2006. DOI: 10.12942/lrsp-2006-2.

[5] R. N. Wilson, *Reflecting Telescope Optics I*, 2nd ed. Berlin-Heidelberg: Springer Verlag, 2007.

[6] B. D. Tapley and J. C. Ries, "Precision orbit determination for earth observation systems," in *Encyclopedia of Space Science and Technology*. John Wiley & Sons, Ltd, 2003. DOI: https://doi.org/10.1002/0471263869.sst023.

[7] Inter-Agency Space Debris Coordination Committee, "IADC Space Debris Mitigation Guidelines," IADC, Tech. Rep. Rev. 3, 2021.

[8] A. Murtaza, S. J. H. Pirzada, T. Xu, *et al.*, "Orbital debris threat for space sustainability and way forward (review article)," *IEEE Access*, vol. 8, pp. 61 000–61 019, 2020. DOI: 10.1109/ACCESS.2020.2979505.

[9] M. W. Taylor, "Orbital debris: Technical and legal issues and solutions," Master's Thesis, McGill University, Montreal, 2006.

[10] H. Kaushal, V. Jain, and S. Kar, *Free Space Optical Communication* (Optical Networks), 1st ed. New Delhi: Springer India, 2017. DOI: 10.1007/978-81-322-3691-7.

[11] R. Wilson, F. Franza, and L. Noethe, "Active Optics: I. A System for Optimizing the Optical Quality and Reducing the Costs of Large Telescopes," *Journal of Modern Optics*, vol. 34, no. 4, pp. 485–509, 1987. DOI: 10.1080/09500348714550501.

[12] C. Schwaer, A. Sinn, and G. Schitter, "Development of active optics for thin meniscus mirrors in 1-meter-class telescopes," in *Advances in Optical and Mechanical Technologies for Telescopes and Instrumentation V*, R. Navarro and R. Geyl, Eds., vol. 12188, p. 121883C, International Society for Optics and Photonics, SPIE, 2022. DOI: 10.1117/12.2625986.

[13] J. W. Hardy, *Adaptive optics for astronomical telescopes*. New York: Oxford University Press, 1998.

[14] C. E. Max, "Adaptive optics: An introduction," 2012.

[15] P. Prager, "Das ideale Teleskop: Kompensation von Aberrationen durch Präzisionspositionierung," Master's Thesis, TU Wien, Vienna, 2021.

[16] E. Hecht, *Optics*, 5th ed. Boston: Pearson Education, Inc, 2017.

[17] J. Cotton. "Telescopes," Physics 1311. (Dec. 26, 2019), [Online]. Available: https://www.physics.smu.edu/jcotton/ph1311/ch03a.htm (visited on 01/12/2025).

[18] NASA. "Telescopes 101 - NASA science," NASA, [Online]. Available: https://science.nasa.gov/universe/telescopes-101/ (visited on 01/12/2025).

[19] S. Littlefair. "L03: Reflector design & practical use," PHY241 Observational Astronomy, [Online]. Available: https://slittlefair.staff.shef.ac.uk/teaching/phy241/lectures/l03/ (visited on 01/13/2025).

[20] R. Patel, S. Achamfuo-Yeboah, R. Light, *et al.*, "Widefield two laser interferometry," *Optics Express*, vol. 22, no. 22, pp. 27 094–27 101, 2014. DOI: 10.1364/OE.22.027094.

[21] M. Hrynevych, K. Tsubota, R. Smythe, *et al.*, "Keck interferometer autoaligner: Algorithms and techniques," *Proceedings of SPIE - The International Society for Optical Engineering*, vol. 5491, 2004. DOI: 10.1117/12.552417.

[22] A. P. Rakich, H. Choi, C. Veillet, *et al.*, "A laser-truss based optical alignment system on LBT," in *Ground-based and Airborne Telescopes VIII*, H. K. Marshall, J. Spyromilio, and T. Usuda, Eds., p. 21, USA: SPIE, 2020. DOI: 10.1117/12.2558013.

[23] L. Noethe, *Active optics in modern, large optical telescopes*, 2001. arXiv: astro-ph/0111136.

[24] A. Adamson. "The telescopes," Gemini Observatory, [Online]. Available: https://www.gemini.eduhttps://www.gemini.edu/observing/telescopes-and-sites/telescopes (visited on 11/26/2024).

[25] J. Lozi, K. Ahn, C. Clergeon, *et al.*, "AO3000 at Subaru: combining for the first time a NIR WFS using First Light's C-RED ONE and ALPAO's 64x64 DM," in *Adaptive Optics Systems VIII*, D. Schmidt, L. Schreiber, and E. Vernet, Eds., SPIE, 2022. DOI: 10.1117/12.2630634.

[26] European Southern Observatory. "Astronomical site monitor (ASM) instruments," ESO, [Online]. Available: https://www.eso.org/sci/facilities/paranal/astroclimate/asm-instruments.html (visited on 01/10/2025).

[27] M. Belío-Asin, J. Sánchez-Capuchino, Á. Mato Martínez, *et al.*, "Active optics strategy for the alignment and operation of the European Solar Telescope," in *Advances in Optical and Mechanical Technologies for Telescopes and Instrumentation V*, R. Geyl and R. Navarro, Eds., Montréal, Canada: SPIE, 2022. DOI: 10.1117/12.2628791.

[28] European Southern Observatory. "Active optics," ESO, [Online]. Available: https://www.eso.org/public/teles-instr/technology/active_optics/ (visited on 10/14/2024).

[29] P. Schipani, S. D'Orsi, L. Ferragina, *et al.*, "Active optics primary mirror support system for the 26m VST telescope," *Applied Optics*, vol. 49, no. 8, p. 1234, 2010. DOI: 10.1364/AO.49.001234.

[30] P. Schipani, S. D'Orsi, D. Fierro, *et al.*, "Active optics control of VST telescope secondary mirror," *Applied Optics*, vol. 49, no. 16, p. 3199, 2010. DOI: 10.1364/AO.49.003199.

[31] F. Bortoletto, C. Bonoli, D. Fantinel, *et al.*, "An active telescope secondary mirror control system," *Review of Scientific Instruments*, vol. 70, no. 6, pp. 2856–2860, 1999. DOI: 10.1063/1.1149807.

[32] "Compact drives for hexapod micropositioning systems," Dr. Fritz Faulhaber GmbH & Co. KG, [Online]. Available: https://www.faulhaber.com/en/motion/hexapod-micropositioning-technology/ (visited on 12/29/2024).

[33] L. Zago and S. Droz, "Small parallel manipulator for the active alignment and focusing of the secondary mirror of the VLTI ATS," in *Optical Design, Materials, Fabrication, and Maintenance*, vol. 4003, pp. 450 – 455, International Society for Optics and Photonics, SPIE, 2000. DOI: 10.1117/12.391536.

[34] B. Smith, T. Chylek, B. Cuerden, *et al.*, "The active optics system for the Discovery Channel Telescope," in *Modern Technologies in Space- and Ground-based Telescopes and Instrumentation*, vol. 7739, p. 77391T, International Society for Optics and Photonics, SPIE, 2010. DOI: 10.1117/12.858047.

[35] N. A. Roddier, D. R. Blanco, L. W. Goble, *et al.*, "WIYN telescope active optics system," in *Telescope Control Systems*, P. T. Wallace, Ed., vol. 2479, pp. 364–376, 1995. DOI: 10.1117/12.211446.

[36] A. T. Tokunaga, "Chapter 51 - new generation ground-based optical/infrared telescopes," in *Encyclopedia of the Solar System (Third Edition)*, T. Spohn, D. Breuer, and T. V. Johnson, Eds., 3rd ed., pp. 1089-1105, Boston: Elsevier, 2014. DOI: https://doi.org/10.1016/B978-0-12-415845-0.00051-7.

[37] J. Palca. "For sharpest views, scope the sky with quick-change mirrors," KCUR. (Jun. 24, 2013), [Online]. Available: https://www.kcur.org/2013-06-24/for-sharpest-views-scope-the-sky-with-quick-change-mirrors (visited on 12/28/2024).

[38] S. Ye, C. Yuan, L. Zhou, *et al.*, "Analysis and compensation of temperature effects on the 1.2m laser ranging telescope," *Measurement*, vol. 247, p. 116 778, 2025. DOI: https://doi.org/10.1016/j.measurement.2025.116778.

[39] W. Zeilinger. "Leopold Figl-Observatorium für Astrophysik," Universität Wien, [Online]. Available: https://foa.univie.ac.at/ (visited on 01/16/2025).

[40] P. Maeda, "Zernike polynomials and their use in describing the wavefront aberrations of the human eye," 2003.

[41] V. N. Mahajan, *Optical imaging and aberrations*. Bellingham, WA, USA: SPIE Optical Engineering Press, 1998.

[42] Wikimedia Commons. "The zernike polynomials values." (May 7, 2008), [Online]. Available: https://commons.wikimedia.org/wiki/File:Zernike_polynomials2.png (visited on 01/08/2025).

[43] K. Niu and C. Tian, "Zernike polynomials and their applications," *Journal of Optics*, vol. 24, no. 12, 2022. DOI: 10.1088/2040-8986/ac9e08.

[44] V. N. Mahajan, "Strehl ratio for primary aberrations in terms of their aberration variance," *Journal of the Optical Society of America*, vol. 73, no. 6, p. 860, 1983. DOI: 10.1364/JOSA.73.000860.

[45] R. R. Shannon and J. C. Wyant, *Applied optics and optical engineering, volume 11*. New York: Academic press, 1992.

[46] I. Norman. "A practical guide to lens aberrations and the lonely speck aberration test," Lonely Speck. (Jul. 15, 2015), [Online]. Available: https://www.lonelyspeck.com/a-practical-guide-to-lens-aberrations-and-the-lonely-speck-aberration-test/ (visited on 01/08/2025).

[47] A. Sinn, P. Prager, C. Schwaer, *et al.*, "Design and evaluation of an active secondary mirror positioning system for a small telescope," *Journal of Astronomical Telescopes, Instruments, and Systems*, vol. 8, no. 2, 2022. DOI: 10.1117/1.JATIS.8.2.029007.

[48] T. Nawratil. "10" RC GSO," Interferometrie und optische Tests. (Jan. 4, 2013), [Online]. Available: http://interferometrie.blogspot.com/2013/01/10-rc-gso.html (visited on 08/25/2024).

[49] "Deep space place," [Online]. Available: https://deepspaceplace.com/gso8rccollimate.php (visited on 08/25/2024).

[50] B. A. McLeod, "Collimation of fast wide-field telescopes," *Publications of the Astronomical Society of the Pacific*, vol. 108, p. 217, 1996. DOI: 10.1086/133712.

[51] C. Schmitz. "How to check and fix telescope collimation in the field," Photographing Space. (Apr. 5, 2018), [Online]. Available: https://www.photographingspace.com/check-fix-telescope-collimation/ (visited on 10/23/2024).

[52] A. Sinn, F. Kreuzmair, C. Schwaer, *et al.*, "Characterization of an active secondary mirror positioning system for a small telescope," in *Advances in Optical and Mechanical Technologies for Telescopes and Instrumentation VI*, R. Navarro and R. Jedamzik, Eds., p. 175, Yokohama, Japan: SPIE, 2024. DOI: 10.1117/12.3021247.

[53] L. Sereinig, "Methods of measuring telescope mirror misalignment," Bachelor's Thesis, TU Wien, Vienna, 2022.